



ANALYSIS OF HYPERSONIC BOUNDARY LAYER
SECOND MODE INSTABILITY OVER A 7° CONE

THESIS

RICHARD A. DENNERY, CAPTAIN, USAF

AFIT/GAE/ENY/94D-20

DEPARTMENT OF THE AIR FORCE
AIR UNIVERSITY

AIR FORCE INSTITUTE OF TECHNOLOGY

Wright-Patterson Air Force Base, Ohio

DISTRIEUTION STATEMENT A

Approved for public release

19950103 064

AFIT/GAE/ENY/94D-20

Accession For	
NTIS CRA&I	<input checked="checked" type="checkbox"/>
DTIC TAB	<input type="checkbox"/>
Unannounced	<input type="checkbox"/>
Justification _____	
By _____	
Distribution /	
Availability Codes	
Dist	Avail and/or Special
A-1	

ANALYSIS OF HYPERSONIC BOUNDARY LAYER
SECOND MODE INSTABILITY OVER A 7° CONE

THESIS

RICHARD A. DENNERY, CAPTAIN, USAF

AFIT/GAE/ENY/94D-20

THIS QUANTITY NOT FOR SALE

Approved for public release; distribution unlimited

ANALYSIS OF HYPERSONIC BOUNDARY LAYER SECOND MODE
INSTABILITY OVER A 7° CONE

THESIS

Presented to the Faculty of the School of Engineering
of the Air Force Institute of Technology
Air University
In Partial Fulfillment of the
Requirements for the Degree of
Master of Science in Aeronautical Engineering

Richard A. Dennery, B.S.

Captain, USAF

December 1994

Approved for public release; distribution unlimited

Preface

In analyzing the data and writing this thesis I have received substantial help from others. I am indebted to my thesis adviser Dr. R Bowersox for his patience and the assistance he rendered. I wish to thank Dr. R. Kimmel of Wright Laboratories, the sponsor of this project, for his experience and patience in explaining concepts in which I had no background. I would also like to thank C. McNeely for his efforts in obtaining and setting up the equipment which permitted my work to begin.

Richard A. Dennery

Abstract

This paper presents the results of the analysis of Mach 8.0 flow over a seven degree half-angle cone. The purpose of this analysis was to develop techniques to examine boundary layer transition at hypersonic velocities. The specific objectives were to look for second mode instability waves characteristic of the transition process and to quantify the percentage of turbulent flow. Two sets of data were used in this analysis. The first set of data was taken at several axial positions at a freestream Reynolds number 4.265 million per meter. This data was used to develop the analysis techniques. The second set of data was taken at station 35 for Reynolds numbers of 3.28, 3.94, 4.92, and 6.56 million per meter.

Spectral analysis was used to identify 2nd mode disturbances, if they existed. The energy associated with the disturbances was then removed from the data signal to produce a new signal. The new signal was then evaluated using conditional sampling techniques. Additional methods used to assess turbulent intermittency were histogram analysis and examination of the power spectrum of the data signal.

It was determined that removal of the disturbances from the raw data signal produced a cleaner signal. However, the new signals were not amenable to conditional sampling techniques. The histogram analysis proved to be inconclusive. Examination of the power spectrum showed that a laminar flow could be identified by the presence of a strong peak corresponding to the 2nd mode disturbances, but could not be used to identify a flow as being turbulent by the absence of this peak.

Table of Contents

PREFACE.....	ii
ABSTRACT.....	iii
LIST OF FIGURES	iv
CHAPTER 1 : INTRODUCTION	1
1.1 BACKGROUND.....	1
1.2 OBJECTIVE.....	5
1.3 SCOPE.....	6
1.4 CONTRIBUTION	6
CHAPTER 2 : THEORY.....	7
CHAPTER 3: DATA COLLECTION AND REDUCTION	16
3.1 INTRODUCTION	16
3.2 TEST FACILITY	16
3.3 TEST ARTICLE.....	16
3.4 TEST INSTRUMENTATION	17
3.5 HOT WIRE ANEMOMETER INSTRUMENTATION.....	18
3.6 TEST CONDITIONS.....	18
3.7 MEAN FLOW DATA ACQUISITION	19
3.8 PROBE CALIBRATION	19
3.9 ANEMOMETER DATA ACQUISITION.....	20
3.10 DIGITIZATION.....	22
3.11 DATA ANALYSIS TECHNIQUES	23
3.12 ANALYSIS PROCEDURE	27
CHAPTER 4 : RESULTS.....	29
4.1 INITIAL DATA SET	29
4.2 PRIMARY DATA SET.....	32
4.2.1 Velocity Profiles	32
4.2.2 Schlieren Photographs.....	33
4.2.3 Spectral Analysis.....	36
4.2.4 Histogram Analysis	41
4.2.5 Conditional Sampling.....	45
4.2.6 Turbulent Bursting	49
CHAPTER 5 : CONCLUSIONS.....	50
CHAPTER 6 : RECOMMENDATIONS.....	51
REFERENCES.....	52
APPENDIX A : INITIAL DATA SET.....	55
VITA.....	84

List Of Figures

FIGURE 1: $Re_L=100,000$; DYE STREAKS IN A BOUNDARY LAYER ON A FLAT PLATE. (WERLE, 1982)	7
FIGURE 2 : $Re_L=100,000$; DYE STREAKS IN A BOUNDARY LAYER ON A FLAT PLATE AT 1° AOA. (WERLE, 1982) [FROM REFERENCE 22].....	8
FIGURE 3 : NEUTRAL CURVES OF THE ORR-SOMMERFELD EQUATION [FROM REFERENCE 23]	9
FIGURE 4: COMPARISON OF THE PREDICTIONS OF THE HYDRODYNAMIC STABILITY THEORY BY LIN(1945) AND WAZZAN ET AL. (1968) FOR THE WAVELENGTH OF NEUTRAL DISTURBANCES FOR FLOW OVER A FLAT PLATE WITH THE MEASUREMENTS OF SCHUBAUER AND SKRAMSTAD (1947) [FROM REFERENCE 22] ..	11
FIGURE 5 : NEUTRAL CURVES FOR SUPERSONIC, ADIABATIC FLAT-PLATE FLOW ILLUSTRATING THE APPEARANCE OF HIGHER ORDER MODES. [AFTER MACK (1969)] [FROM REFERENCE 23]	13
FIGURE 6 : TEMPORAL AMPLIFICATION RATES AND MOST UNSTABLE WAVE DIRECTION ϕ FOR ADIABATIC FLOW PAST A FLAT PLATE [AFTER MACK (1969)] [FROM REFERENCE 23].....	14
FIGURE 7 : TRANSITION MEASUREMENTS AS A FUNCTION OF REYNOLDS NUMBER IN WIND TUNNELS, BALLISTIC RANGES, AND FLIGHT. (FROM OWEN, 1990) [FROM REFERENCE 22]	15
FIGURE 8 : HOT-WIRE ANEMOMETER PROFILE, CONSTANT HEATING CURRENT ¹³	21
FIGURE 9 : CONDITIONAL SAMPLING FOR TURBULENT INTERMITTENCY FACTOR OF 0.4	26
FIGURE 10 : FFT FOR ODD NUMBERED STATIONS; $Re_\infty=4,625,000/M$	30
FIGURE 11: BOUNDARY LAYER VELOCITY PROFILES FOR VARYING REYNOLDS NUMBER.....	32
FIGURE 12: FLOWFIELD FOR $Re_\infty= 3,560,000/M$, FRONT VIEW	33
FIGURE 13: FLOWFIELD FOR $Re_\infty= 3,560,000/M$, AFT VIEW	34
FIGURE 14: FLOWFIELD FOR $Re_\infty= 4,92E6/M$, FRONT VIEW	34
FIGURE 15: FLOWFIELD FOR $Re_\infty= 4,920,000/M$, AFT VIEW	35
FIGURE 16: FLOWFIELD FOR $Re_\infty= 6,560,000/M$, FRONT VIEW	35
FIGURE 17: FLOWFIELD FOR $Re_\infty= 6,560,000/M$, AFT VIEW	36
FIGURE 18: FFT FOR $Re_\infty= 3,280,000/M$	37
FIGURE 19: FFT FOR $Re_\infty= 3,940,000/M$	38
FIGURE 20: FFT FOR $Re_\infty= 4,920,000/M$	38
FIGURE 21: FFT FOR $Re_\infty= 6,560,000/M$	39
FIGURE 22: POWER SPECTRA FOR $Re_\infty= 3,280,000/M$	39
FIGURE 23: POWER SPECTRA FOR $Re_\infty= 3,940,000/M$	40
FIGURE 24: POWER SPECTRA FOR $Re_\infty= 4,920,000/M$	40
FIGURE 25: POWER SPECTRA FOR $Re_\infty= 6,560,000/M$	41
FIGURE 26: HISTOGRAM FOR $Re_\infty= 3,280,000/M$	42
FIGURE 27: HISTOGRAM FOR $Re_\infty= 3,940,000/M$	43
FIGURE 28: HISTOGRAM FOR $Re_\infty= 4,920,000/M$	43
FIGURE 29: HISTOGRAM FOR $Re_\infty= 6,560,000/M$	44
FIGURE 30: SKEWNESS FACTOR FOR STATION 35.....	44
FIGURE 31: FLATNESS FACTOR FOR STATION 35.....	45
FIGURE 32: DATA SIGNALS FOR $Re_\infty= 3,280,000/M$	47
FIGURE 33: DATA SIGNALS FOR $Re_\infty= 3,940,000/M$	47
FIGURE 34: DATA SIGNALS FOR $Re_\infty= 4,920,000/M$	48
FIGURE 35: DATA SIGNALS FOR $Re_\infty= 6,560,000/M$	48
FIGURE A.1: FFT FOR STATION 27; $Re_\infty=4,265,000/M$	55
FIGURE A.2 : FFT FOR STATION 28; $Re_\infty=4,265,000/M$	55
FIGURE A.3 : FFT FOR STATION 29; $Re_\infty=4,265,000/M$	56
FIGURE A.4 : FFT FOR STATION 30; $Re_\infty=4,265,000/M$	56
FIGURE A.5 : FFT FOR STATION 31; $Re_\infty=4,265,000/M$	57
FIGURE A.6 : FFT FOR STATION 32; $Re_\infty=4,265,000/M$	57
FIGURE A.7 : FFT FOR STATION 33; $Re_\infty=4,265,000/M$	58

FIGURE A.8 : FFT FOR STATION 34; $Re_{\infty}=4,265,000/M$	58
FIGURE A.9 : FFT FOR STATION 35; $Re_{\infty}=4,265,000/M$	59
FIGURE A.10 : FFT FOR STATION 36; $Re_{\infty}=4,265,000/M$	59
FIGURE A.11 : FFT FOR STATION 37; $Re_{\infty}=4,265,000/M$	60
FIGURE A.12 : POWER SPECTRUM FOR STATION 27; $Re_{\infty}=4,265,000/M$	60
FIGURE A.13 : POWER SPECTRUM FOR STATION 28; $Re_{\infty}=4,265,000/M$	61
FIGURE A.14 : POWER SPECTRUM FOR STATION 29; $Re_{\infty}=4,265,000/M$	61
FIGURE A.15 : POWER SPECTRUM FOR STATION 30; $Re_{\infty}=4,265,000/M$	62
FIGURE A.16 : POWER SPECTRUM FOR STATION 31; $Re_{\infty}=4,265,000/M$	62
FIGURE A.17 : POWER SPECTRUM FOR STATION 32; $Re_{\infty}=4,265,000/M$	63
FIGURE A.18 : POWER SPECTRUM FOR STATION 33; $Re_{\infty}=4,265,000/M$	63
FIGURE A.19 : POWER SPECTRUM FOR STATION 34; $Re_{\infty}=4,265,000/M$	64
FIGURE A.20 : POWER SPECTRUM FOR STATION 35; $Re_{\infty}=4,265,000/M$	64
FIGURE A.21 : POWER SPECTRUM FOR STATION 36; $Re_{\infty}=4,265,000/M$	65
FIGURE A.22 : POWER SPECTRUM FOR STATION 37; $Re_{\infty}=4,265,000/M$	65
FIGURE A.23 : DATA SIGNALS FOR STATION 27; $Re_{\infty}=4,265,000/M$	66
FIGURE A.24 : DATA SIGNALS FOR STATION 28; $Re_{\infty}=4,265,000/M$	66
FIGURE A.25 : DATA SIGNALS FOR STATION 29; $Re_{\infty}=4,265,000/M$	67
FIGURE A.26 : DATA SIGNALS FOR STATION 30; $Re_{\infty}=4,265,000/M$	67
FIGURE A.27 : DATA SIGNALS FOR STATION 31; $Re_{\infty}=4,265,000/M$	68
FIGURE A.28 : DATA SIGNALS FOR STATION 32; $Re_{\infty}=4,265,000/M$	68
FIGURE A.29 : DATA SIGNALS FOR STATION 33; $Re_{\infty}=4,265,000/M$	69
FIGURE A.30 : DATA SIGNALS FOR STATION 34; $Re_{\infty}=4,265,000/M$	69
FIGURE A.31 : DATA SIGNALS FOR STATION 35; $Re_{\infty}=4,265,000/M$	70
FIGURE A.32 : DATA SIGNALS FOR STATION 36; $Re_{\infty}=4,265,000/M$	70
FIGURE A.33 : DATA SIGNALS FOR STATION 37; $Re_{\infty}=4,265,000/M$	71
FIGURE A.34 : HISTOGRAM FOR STATION 27; $Re_{\infty}=4,265,000/M$	71
FIGURE A.35 : HISTOGRAM FOR STATION 28; $Re_{\infty}=4,265,000/M$	72
FIGURE A.36 : HISTOGRAM FOR STATION 29; $Re_{\infty}=4,265,000/M$	72
FIGURE A.37 : HISTOGRAM FOR STATION 30; $Re_{\infty}=4,265,000/M$	73
FIGURE A.38 : HISTOGRAM FOR STATION 31; $Re_{\infty}=4,265,000/M$	73
FIGURE A.39 : HISTOGRAM FOR STATION 32; $Re_{\infty}=4,265,000/M$	74
FIGURE A.40 : HISTOGRAM FOR STATION 33; $Re_{\infty}=4,265,000/M$	74
FIGURE A.41 : HISTOGRAM FOR STATION 34; $Re_{\infty}=4,265,000/M$	75
FIGURE A.42 : HISTOGRAM FOR STATION 35; $Re_{\infty}=4,265,000/M$	75
FIGURE A.43 : HISTOGRAM FOR STATION 36; $Re_{\infty}=4,265,000/M$	76
FIGURE A.44 : HISTOGRAM FOR STATION 37; $Re_{\infty}=4,265,000/M$	76
FIGURE A.45 : SKEWNESS FACTOR FOR $Re_{\infty}=4,265,000/M$	77
FIGURE A.46 : FLATNESS FACTOR FOR $Re_{\infty}=4,265,000/M$	77
FIGURE A.47 : FFT (ALT. SOURCE) FOR STATION 27; $Re_{\infty}=4,265,000/M$	78
FIGURE A.48 : FFT (ALT. SOURCE) FOR STATION 28; $Re_{\infty}=4,265,000/M$	78
FIGURE A.49 : FFT (ALT. SOURCE) FOR STATION 29; $Re_{\infty}=4,265,000/M$	79
FIGURE A.50 : FFT (ALT. SOURCE) FOR STATION 30; $Re_{\infty}=4,265,000/M$	79
FIGURE A.51 : FFT (ALT. SOURCE) FOR STATION 31; $Re_{\infty}=4,265,000/M$	80
FIGURE A.52 : FFT (ALT. SOURCE) FOR STATION 32; $Re_{\infty}=4,265,000/M$	80
FIGURE A.53 : FFT (ALT. SOURCE) FOR STATION 33; $Re_{\infty}=4,265,000/M$	81
FIGURE A.54 : FFT (ALT. SOURCE) FOR STATION 34; $Re_{\infty}=4,265,000/M$	81
FIGURE A.55 : FFT (ALT. SOURCE) FOR STATION 35; $Re_{\infty}=4,265,000/M$	82
FIGURE A.56 : FFT (ALT. SOURCE) FOR STATION 36; $Re_{\infty}=4,265,000/M$	82
FIGURE A.57 : FFT (ALT. SOURCE) FOR STATION 37; $Re_{\infty}=4,265,000/M$;	83

Chapter 1 : Introduction

1.1 Background

The nature of the boundary layer in hypersonic flow is of critical importance in determining the drag and heating characteristics of the object in question. A laminar boundary layer results in decreased drag and a lower heat transfer rate compared to that of a turbulent boundary layer. However, for most applications of interest, a laminar boundary layer is inherently unstable under most conditions and will transition to turbulence. The factors influencing boundary layer transition include nose radius, pressure gradient, surface curvature, surface roughness, surface mass transfer (blowing or suction), surface and freestream temperatures and freestream disturbances.

It is a relatively simple matter to estimate the drag and heating coefficients for laminar and turbulent boundary layers. The situation is much more complicated in solving for these coefficients in the transition region. This would merely be a curiosity if this region was small relative to the total flow area, but the transition region can be many times the size of either the laminar or turbulent areas. In an effort to develop coefficients for this region, the transition region is often defined to be turbulent a certain percentage of the time and laminar all other times. These percentages are then used to perform an averaging of the known laminar and turbulent coefficients to provide estimates for the transition region.

Many investigations concerning the transition from laminar flow to turbulent flow have been performed over the last 100 years. It was proposed as early as the 19th century,

although unsupported at the time, that the instability of laminar flow causes turbulence¹. Prandtl², using a linear model, advanced this notion one step further showing that viscosity destabilized the boundary layer. While this work was applied only to an incompressible boundary layer on a flat plate, henceforth referred to as the Blasius boundary layer, it was an important first step. Tollmein and Schlichting furthered this area of study with a well-developed theory for the Blasius boundary layer stability¹. Subsequently, numerous stability calculations were done for a large number of boundary layers with favorable and adverse pressure gradients. The primary result of this theory was that disturbance frequency is the most significant characteristic in the occurrence of transition. This theory remained unsupported experimentally until Schubauer and Skranstad³ demonstrated the existence of instability waves in a boundary layer with small external disturbances that behaved according to the theory. They also showed that the location of transition could be changed by adjusting the amplitude and/or frequency of the artificially induced sinusoidal boundary layer disturbance. In another experiment that included freestream disturbances of similar amplitude, Spangler and Wells⁴ found a much higher transition Reynolds number than the experiment of Schubauer and Skranstad. Even though the two experiments had similar freestream disturbance amplitudes, the spectra of the disturbances were significantly different. This demonstrated the importance of the external disturbance spectra in the transition from laminar to turbulent flow. In contrast to the low disturbance levels in the previously mentioned experiments, Bennett⁵, using a tunnel with large external disturbances (0.42%), also demonstrated that instability waves precede transition. Jackson and Heckle⁶ showed that disturbance

amplitude was extremely sensitive to disturbance frequency for a freestream turbulence level of 0.2-0.4% while maintaining the location of transition at a fixed point.

The results of these and numerous other studies were used to estimate boundary layer transition location in situations of similar geometry, similar environmental conditions and similar flow conditions. In many of these experiments the objective was determining where transition occurred rather than on the disturbance mechanism that caused transition. This lack of knowledge on the transition process made predictions of transition in new situations based upon extrapolation of old data somewhat uncertain. This becomes especially true as the flow changes from subsonic to supersonic, or from supersonic to hypersonic flow.

This was demonstrated in the early supersonic transition experiments when it was noticed that cooling the surface of the model increased the critical Reynolds number and had a stabilizing effect on the boundary layer. This held true up to a point, after which, increasing the Mach number decreased the critical Reynolds number. The authors Reference 29 performed experiments investigating this behavior and reported data consistent with this trend.

“Since the authors of Reference 29 had no knowledge of second mode disturbances at the time of the study, their data were compared with supersonic data which reported a similar trend for surface temperature effects on transition, the so called “transition reversal” data³⁰⁻³². In retrospect, it appears likely that these Mach 5.5 shock tunnel transition data were the result of second mode dominated transition. Since second mode disturbances become more unstable as T_w/T_{AD} decreases, it would be expected that the transition Reynolds number would decrease as T_w/T_{AD} decreased. Thus, such results should then not be considered a transition reversal in the sense of a reversal from the expected theoretical trend.”²¹

The discovery of this second mode instability, which will be discussed in greater detail in Chapter 2, at high Mach numbers and its unique characteristics required hypersonic transition problems to be treated independently from those of low speed or supersonic transition problems. It became necessary to understand the higher instability modes, and stability experimentation at high Mach numbers was a prerequisite. To date there have only been a handful of hypersonic boundary layer stability experiments. They include Kendall^{7,8} in the Jet Propulsion Laboratory (JPL) supersonic wind tunnel ($M = 4.5$ and 5.6) and the hypersonic wind tunnel ($M = 8.5$), Demetriades⁹⁻¹² in the GALCIT Leg 1 hypersonic tunnel ($M = 5.8$) and the AEDC Tunnel B ($M = 8.0$), and those of Stetson, et al.¹³⁻¹⁹ in the AEDC Tunnel B ($M = 6.0$ and 8.0).

Demetriades performed the first hypersonic stability in 1958. This was prior to the knowledge of the higher order instability modes and his investigation did not identify any of these modes. The first confirmation of the second mode disturbances and their dominance in the hypersonic boundary layer came from Kendall's experiment in 1967. This experiment was conducted while maintaining laminar flow on the tunnel walls and avoiding the "noisy" freestream conditions that normally resulted from this type of testing. Artificial disturbances were then introduced into the boundary layer at frequencies corresponding to the first mode and second mode instabilities. The streamwise growth of these disturbances was measured using hot wire anemometry. Comparison of these experimental results with Mack's numerical calculations provided the first confirmation of the second mode instability. Kendall's Mach 8.5 tests⁷ in 1975 generated the frequencies and growth rates associated with the second mode and confirmed that the

second mode was the dominant instability. Demetriades obtained additional instability characteristics and confirmed that wall cooling destabilizes the second mode disturbances with his Mach 8.0 experiments¹² in 1978.

The experiments of Stetson, et al. are part of a continuing program begun in 1979. The results of this program are documented in References 13-21 with Reference 21 being a summary of the overall program. The program itself has shown that the concepts of subsonic and supersonic flow stability cannot simply be extended to hypersonic flows. A principal difference between the subsonic, supersonic, and hypersonic speed regimes is the disturbances that precede transition. Subsonic and supersonic flow disturbances contain velocity fluctuations with amplitudes of approximately 1% that of the freestream velocity. The flow disturbances in hypersonic boundary layers are predominately the result of variations in density that cause mass flux fluctuations up to 8% that of the local mean mass flow. This result has required a reexamination of the small disturbance assumption used in deriving the linear stability theory.

1.2 Objective

The purpose of this analysis was to develop techniques to examine boundary layer transition at hypersonic velocities. The specific objectives were to look for second mode instability waves characteristic of the transition process and to quantify the percentage of turbulent flow. Two sets of data were used in this analysis. The first set of data was taken at several axial positions at a freestream Reynolds number 4.265 million per meter.

This data was used to develop the analysis techniques. The second set of data was taken at station 35 for Reynolds numbers of 3.28, 3.94, 4.92, and 6.56 million per meter.

1.3 *Scope*

The data analyzed includes Mach 8.0 flow over a cone at a freestream Reynolds number 4.265 million per meter at multiple downstream stations and flow over the same cone at a single station for Reynolds numbers of 3.28, 3.94, 4.92, and 6.56 million per meter.

1.4 *Contribution*

The results from this analysis expand the data base for hypersonic boundary layer transition at higher Reynolds number conditions. It also provides information with regard to the assumptions made about the transition process in hypersonic boundary layers.

Chapter 2 : Theory

It is generally accepted that a turbulent boundary layer results when disturbances within the flow grow to sufficient amplitude to break down the laminar boundary layer. The transition from a laminar to a turbulent boundary layer does not occur instantaneously, but rather is the result of a process by which these disturbances grow in a finite region. The first requirement to begin this process is the existence of some disturbance within the flow. Sources of possible disturbances include vorticity, variations in entropy, and sound fluctuations within the freestream, and roughness or vibration on the surface. The disturbance will then begin to grow as it travels downstream forming two-dimensional waves. This growth assumes the boundary layer is unstable with respect to the particular disturbance. This will be discussed in more detail later. These waves are commonly referred to as Tollmein-Schlichting waves and can be clearly seen in Figure 1.

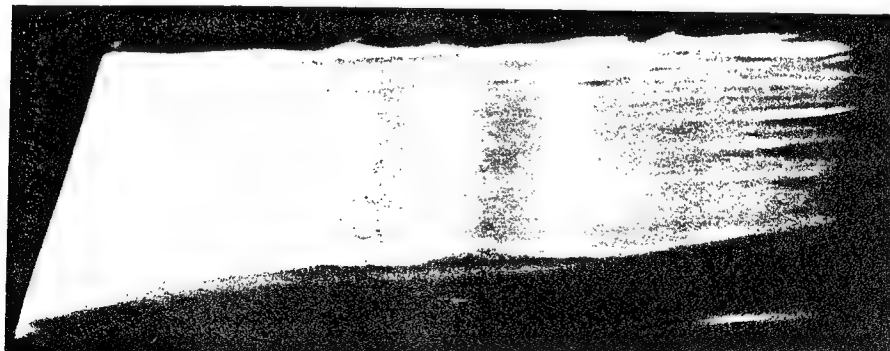


Figure 1: $Re_L=100,000$; Dye Streaks in a boundary layer on a flat plate. (Werle, 1982) [from Reference 22]

The two-dimensional waves will continue to grow forming three-dimensional structures that eventually break down into localized spots of turbulence. Fully turbulent flow results

when the turbulent spots merge together. This process can be seen in the following picture of flow over a flat plate from Werle (1982)²².

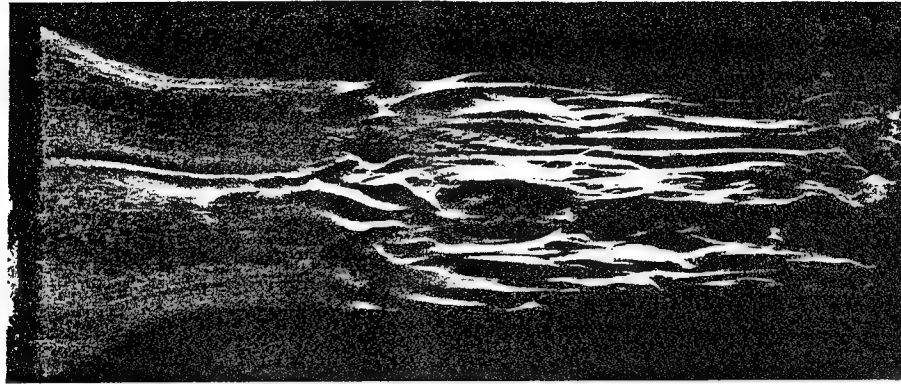


Figure 2 : $Re_L=100,000$; Dye Streaks in a boundary layer on a flat plate at 1° AOA.
(Werle, 1982) [from Reference 22]

It has been suggested that all disturbances may not grow within the boundary layer. A boundary layer can do three things to a particular disturbance; amplify it, damp it, or let it pass unchanged. These three possibilities are respectively referred to as unstable, stable, or neutrally stable conditions. Hydrodynamic stability theory was developed to predict when flow instability would occur.

The difficulty in analyzing small, unsteady, three dimensional disturbances in the background of laminar flow is apparent. Squire's theorem that two dimensional disturbances are always less stable than three dimensional disturbances for low speed flow simplified the problem²². This theorem implied that the two-dimensional analysis is sufficient to find the minimum instability conditions. The primary simplifying assumptions used to perform this analysis are (1) disturbance quantities are small

compared to the baseline flow; (2) the baseline flow is only a function of the transverse coordinate; (3) and the disturbance can be written as

$$\Psi(x, y, t) = \phi(y) \exp[i\alpha(x - ct)] \quad (1)$$

where $\phi(y)$ is a complex amplitude function, $\alpha = \alpha_r + i\alpha_i$ is the wave number of the disturbance and c is the complex phase velocity. Examination of this equation reveals that stability with respect to time is dependent upon the value of αc_i where $c_i = c_i$. Positive values of this quantity result in amplification of the instability while negative values result in disturbance damping. A zero value is the condition of neutral stability.

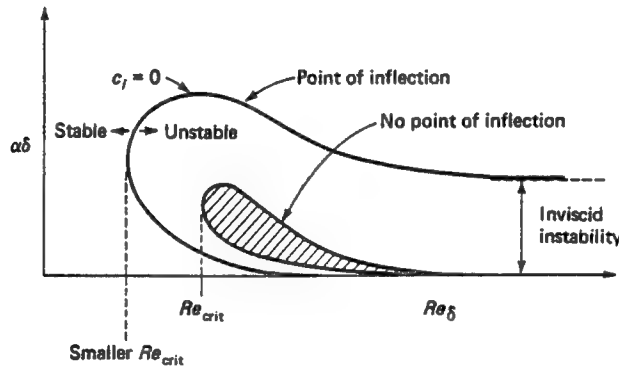


Figure 3 : Neutral Curves of the Orr-Sommerfeld Equation [from Reference 23]

The unsteady Navier-Stokes equations for incompressible, constant property, laminar flow reduces to

$$(u_o - c)(\phi'' - \alpha^2 \phi) - u_o'' \phi = \frac{-i}{\alpha Re} (\phi^{(iv)} - 2\alpha^2 \phi'' + \alpha^4 \phi) \quad (2)$$

which is well known as the Orr-Sommerfeld equation. The locus of $c_i=0$ is referred to as the neutral curve. A plot of this can be seen in Figure 3 where the vertical axis, α_i ,

represents the temporal instability. The outer curve, which results in a smaller Re_{crit} , represents a velocity profile that contains a point of inflection. The inner curve has no point of inflection and closes at large Reynolds number. Disturbances falling within the curves are amplified while those outside the curve are damped.

It is important to realize that Re_{crit} represents the lowest Reynolds number where disturbances may be amplified. It does not correlate to the position where flow will transition. This positive amplification simply satisfies the criteria permitting the initially small disturbances to begin their growth that ultimately leads to turbulence. The values of αc_i within the curve are probably more important than Re_{crit} because it is this value that determines the disturbance growth rate, with higher values resulting in earlier transition.²³

While this stability theory cannot predict flow transition, it can be used to find what parameters enhance or restrict transition. For example, velocity profiles containing an inflection point are very unstable. An adverse pressure gradient will tend toward profiles with an inflection point. Therefore, flow with an adverse pressure gradient will become unstable and transition earlier than an equal flow with zero pressure gradient. The effects of favorable pressure gradients, boundary layer injection, suction, and surface heating or cooling (it changes the fluid viscosity) can also be explored.

This theory works quite well for low speed flow as demonstrated by Figure 4. However, the statements that (1) a flat plate boundary layer has no inflection point and is therefore stable from an inviscid stand point; (2) the most unstable disturbance is two

dimensional and (3) there exists a maximum of one unstable frequency at each Reynolds number and wave angle, are all incorrect for a compressible boundary layer. In the case of Squire's theorem, the most unstable waves no longer need to be parallel to the freestream.

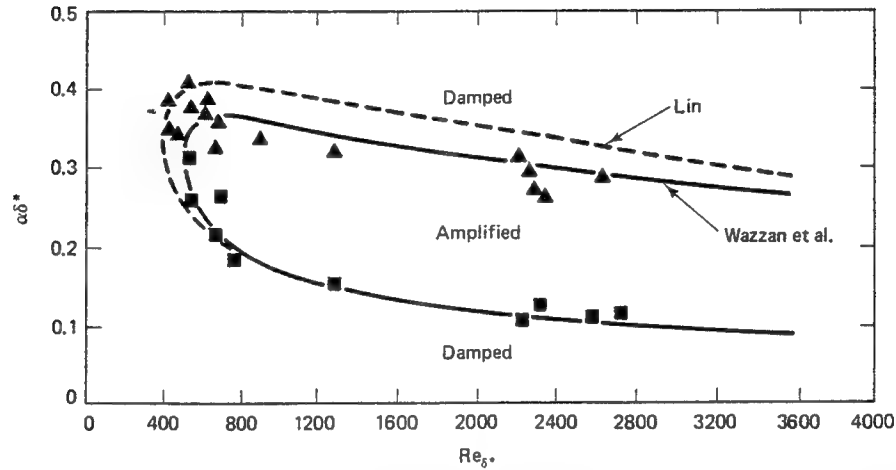


Figure 4: Comparison of the predictions of the hydrodynamic stability theory by Lin(1945) and Wazzan et al. (1968) for the wavelength of neutral disturbances for flow over a flat plate with the measurements of Schubauer and Skramstad (1947) [from Reference 22]

Lee and Lins²⁴ showed that the inflection point criteria for inviscid stability is

replaced by $\frac{d}{dy} \left(\frac{dU/dy}{T} \right) \Big|_s = 0$ for compressible flow where U is the mean flow and T is

the temperature evaluated at the generalized inflection point (y_s). This point moves away from the surface with increasing Mach number. Corresponding to this movement away from the surface is an increase in the inviscid instability. Simultaneously, the viscous instability mechanism weakens, so that when the freestream Mach number reaches about 3, the maximum amplification rate occurs as the Reynolds number approaches infinity and viscosity has only a stabilizing influence¹. Furthermore, multiple instability modes

come into existence when there is a region of supersonic mean flow relative to the disturbance phase velocity. The reason for the additional modes can be seen in the inviscid stability equation for the pressure-fluctuation amplitude function $\pi(y)$ of a disturbance of neutral stability $\pi(y)\exp[i(\alpha x - \omega t)]$

$$\pi'' - (\log M^2)' \pi' - \alpha^2 (1 - M^2) \pi = 0 \quad (3)$$

where M is the local Mach number of the mean flow relative to the disturbance phase velocity c_r .¹ This equation is a wave equation in the region from the wall to a point y_a where supersonic relative flow exists. Each standing wave length in the y direction is the disturbance wavelength $(2\pi/\alpha)$ times a factor involving the mean relative flow. This requires the existence of multiple values of α where the additional α_n are referred to as the higher modes. All of these modes are unstable with the first mode (due to viscosity), having the greatest spatial amplification rate and the first additional mode, referred to as the second mode, being the most unstable of the higher modes. The first mode has its greatest amplification at low speeds and decreases with Mach number. The second mode appears only at a very high frequency and is extremely weak below Mach 3.7. This mode grows in strength as Mach number increases eventually merging with the first mode and becoming indistinguishable by Mach 7. Figure 5 demonstrates the merging of the first and second mode neutral stability curves.

As the regime of interest moves from supersonic flow to that of hypersonic flow, Squire's theorem becomes valid again. In supersonic flow, the most unstable disturbance is always oblique and peaks at a wave angle of 65° around Mach 3.¹ In contrast, the

higher modes' most unstable disturbances are always two dimensional. Examination of Figure 6 shows that the most unstable first mode disturbances satisfies Squire's theorem ($\phi=0$) up until $M=0.7$ while the second mode disturbances always meet this criterion. Additionally, above $M=4$ the second mode becomes the dominate instability

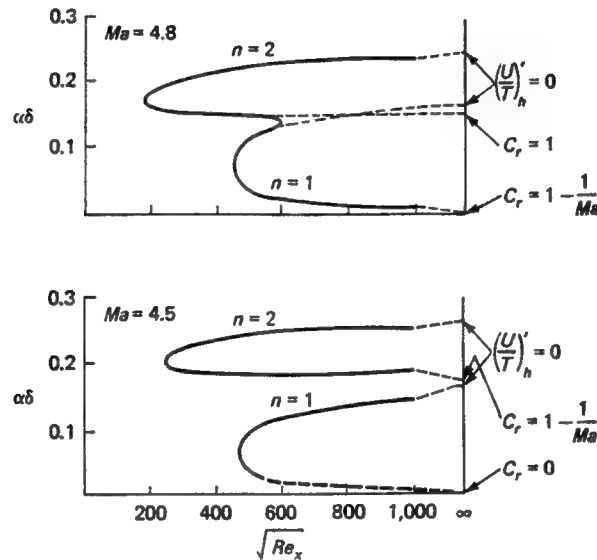


Figure 5 : Neutral curves for supersonic, adiabatic flat-plate flow illustrating the appearance of higher order modes. [After Mack (1969)] [from Reference 23]

It has already been mentioned that the presence of flow instability does not necessarily result in transition. The theory presented thus far only concerns itself with the characteristics of flow stability. No theory exists that can predict the onset of transition. All current methods for predicting transition are based on empirical relations derived from the results of years of experimentation. There are numerous relations in existence that attempt to predict the onset of transition with some modest success. However, Figure 7 demonstrates the problem with attempting to predict transition when seemingly similar tests are run with very dissimilar results. It is now known that the similar

experiments contained small differences that result in large effects. One of the best examples of this is Reynolds' pipe flow experiment which had a transition Reynolds number of 2300 while subsequent studies that carefully tailored the inlet flow achieved transition Reynolds number up to 20,000. This sensitivity to experimental conditions underlies all work in this area.

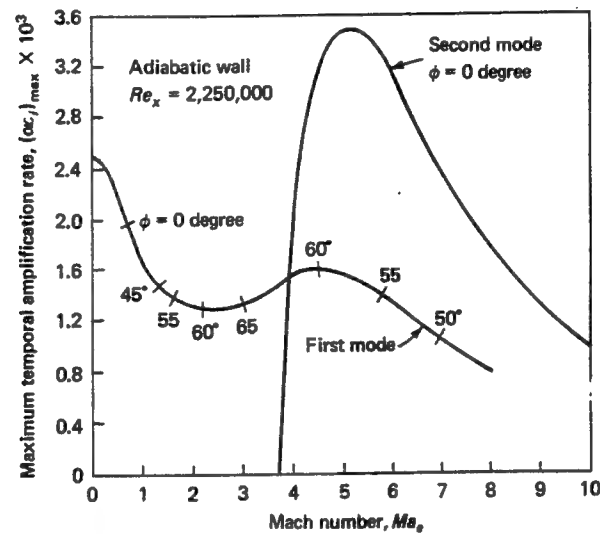


Figure 6 : Temporal amplification rates and most unstable wave direction ϕ for adiabatic flow past a flat plate [After Mack (1969)] [from Reference 23]

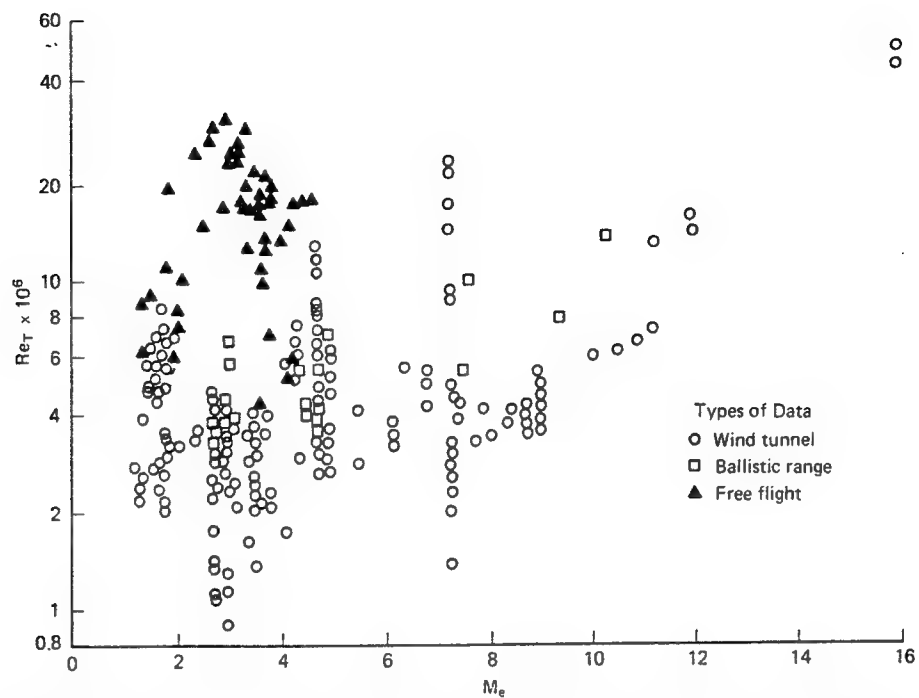


Figure 7 : Transition measurements as a function of Reynolds number in wind tunnels, ballistic ranges, and flight. (From Owen, 1990) [from Reference 22]

Chapter 3: Data Collection and Reduction

3.1 Introduction

This chapter outlines the test methods and data collection techniques used to acquire the boundary layer data analyzed in this paper. The process by which the data was digitized and the analysis procedure is also reviewed. Finally, a brief discussion of the signal processing techniques used is also included.

3.2 Test Facility

Arnold Engineering Development Center (AEDC) conducted testing in Tunnel B. This tunnel contains a 1.27 meter diameter test section. Air is provided to the tunnel by the von Karman Facility main compressor plant at pressures of 137.9 to 2068.5 Pa at Mach 6 and 344.75 to 6205.5 Pa at Mach 8. A natural gas fired heater is used to raise stagnation temperatures up to 750 K to avoid air liquefaction in the test section. Integral, external water jackets are used to cool the entire tunnel. A model injection system permits test article changes while the tunnel remains in operation.

3.3 Test Article

The test article used was a seven degree half angle cone, 1.016 m long with a 0.2495 m base diameter. The basic model allowed for interchangeable nose sections. The tip radius of the nose section used for this test was 38.1 μm . Instrumentation consisted of 24 pressure ports and 32 coaxial surface thermocouples. The instrumentation was arranged along four rays, with the top centerline (zero degree ray)

being the primary ray of pressure instrumentation. Additional pressure orifices were installed on the 180° and 270° rays at three axial stations. All of the thermocouples were installed on the 180° ray.

3.4 Test Instrumentation

The Pitot pressure probe was made by flattening a 0.635 mm O.D. (0.508 mm I.D.) tube which produced a probe tip thickness of 0.2794 mm with an orifice height of 0.1524 mm. The tube section adjacent to the orifice was bent to align the probe parallel to the model surface for the surveys.

The unshielded total temperature probe was fabricated from a length of sheathed thermocouple wire (0.508 mm O.D.) with two 0.1016 mm diameter wires. The wires were bared for a length of about 0.381 mm and a thermocouple junction of approximately 0.127 mm diameter was made.

Hot wire anemometer probes of platinum-10% rhodium wires, drawn by the Wollaston process, of 0.508 μm or 1.27 μm nominal diameter and approximately 150 diameters length, were attached to sharpened 2.0 -mil nickel wire supports using a bonding technique developed by Philco-Ford Corporation²⁵. The wire supports were inserted in an alumina cylinder of 0.7874 mm diameter and 6.33 mm length, which was, in turn, cemented to an alumina cylinder of 2.3876 mm diameter and 7.62 cm length that carried the hot wire leads through the probe holder of the survey mechanism.

3.5 Hot Wire Anemometer Instrumentation

Flow fluctuation measurements were made using constant current hot wire anemometry techniques. The anemometer current control (Philco-Ford Model ADP-13) which supplies the heating current to the sensor is capable of maintaining the current at any one of 15 preset levels. The anemometer amplifier (Philco-Ford Model ADP-12) which amplifies the wire-response signal contains the circuits required to electronically compensate the signal for thermal lag which is a characteristic of the finite heat capacity of the wire. A square-wave generator was used in determining the time constant of the sensor whenever required. The sensor heating current and mean voltage were monitored by autoranging digital voltmeters for a visual display and a Bell and Howell model VR3700B magnetic tape machine for recording. The sensor response a-c coupled signal was monitored by an oscilloscope for visual display of the raw signal and a wave analyzer (Hewlett Packard Model 8553B/8552B) for visual display of the spectra of the fluctuating signal. The a-c signals were recorded on magnetic tape for subsequent analysis. A detailed description of the hot-wire anemometer instrumentation is given in Reference 26.

3.6 Test Conditions

Data was acquired for the sharp cone model at the following test condition.

M_∞	P_o (kPa)	T_o (K)	P_∞ (kPa)	$Re_\infty/m \times 10^{-6}$
7.96	2068.5	750	0.2206	4.265

3.7 Mean Flow Data Acquisition

Mean flow data was acquired using hot wire anemometry techniques. Boundary layer profile data (Pitot pressure and total temperature) were collected to define the region around the hot wire. The profiles ranged from 0.635 mm above the surface to two to three times the boundary layer thickness. The probe travel was normal to the surface. The flow field surveys were obtained only after the model had reached equilibrium temperature. The model was rolled about the centerline axis to provide a smooth surface, free of surface instrumentation, upstream of the flow field being surveyed.

3.8 Probe Calibration

The evaluation of flow fluctuation quantitative measurements with hot wire anemometry techniques requires a knowledge of certain thermal and physical characteristics of the wire sensor employed. In application of the hot wire to wind tunnel tests at AEDC, two complementary calibrations are used to evaluate the wire characteristics needed. The first calibration of each hot wire probe was performed in a laboratory oven prior to the testing; the wire reference resistance at 273 K and the thermal coefficient of resistance, also at 273 K, are obtained from the results.

The second calibration of each hot wire probe was done in the wind tunnel free stream flow to obtain the heat loss coefficient (Nusselt number) and the temperature recovery factor characteristics of the wire sensor as a function of local Reynolds number.

The resulting relationships were used to determine the values of the various wire sensitivity parameters required in the reduction of the quantitative measurements.

Since the total temperature probe was unshielded, a recovery factor calibration had to be performed. The calibration of the recovery factor as a function of local Reynolds number was made in the free stream flow of the tunnel test section.

3.9 Anemometer Data Acquisition

The hot wire anemometer data were of three general categories: 1) continuous-traverse surveys of the boundary layer to map the response of the hot wire anemometer as a function of distance normal to the surface, 2) discrete point boundary layer profile surveys using the hot wire operated at a single heating current to determine the variation of the spectrum of the wire a-c voltage component across the boundary layer at selected model station, 3) quantitative hot wire measurements using the wire operated at each of a series of wire heating currents at one selected location on a given profile, to determine the magnitude of the mass flux (ρu)' and total temperature (T_t)' fluctuations.

Continuous traverse data were acquired with the hot wire operated using a single heating current, in the present case the maximum practical current. The maximum overheat was chosen to minimize the hot-wire sensitivity to total temperature fluctuations. The probe was translated in a continuous manner in the direction normal to the model surface from near the surface outward to a distance of approximately twice the boundary layer thickness and the hot wire response (rms of the a-c voltage component) was obtained as a function of probe height.

Discrete point hot wire profile data, were obtained simultaneously with the mean flow boundary layer survey data. The signal was recorded as a function of time at discrete points across the boundary layer. The wire response (a-c voltage component) was recorded on magnetic tape at each discrete point in the profile.

Quantitative hot wire data (third category) were acquired at selected locations of significant disturbance energy as determined from the continuous traverse surveys (first category data). The point of maximum rms voltage output of the hot wire, the “maximum energy point”, of the profile was selected for quantitative measurements at each model station. The quantitative data were acquired at 12 wire heating currents; one current was nominally zero to obtain a measurement of the electronic noise of the anemometer instrumentation.

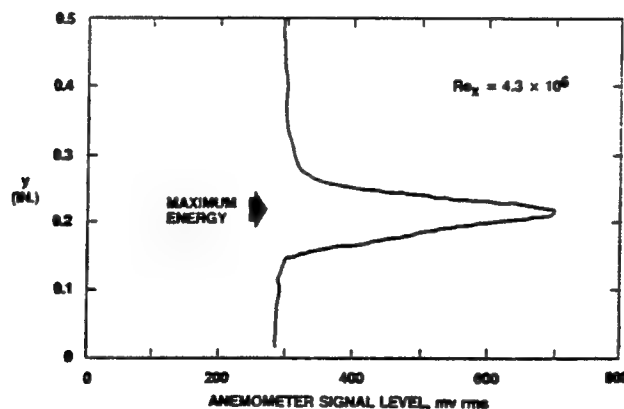


Figure 8 : Hot-wire anemometer profile, constant heating current¹³

The data analyzed in this paper were taken as part of the program documented in References 13-21. The preceding description of the test setup has been extracted from Reference 13.

3.10 Digitization

The anemometer response (a-c voltage) signals recorded on magnetic tape were digitized by a Nicolet 500 data acquisition system (DAS) at the Air Force Institute of Technology (AFIT). The data tape contained a data track and a "valid data" identification signal. The data tape was played with both signals routed through an oscilloscope and the data signal routed to the DAS. Each run contained five seconds of valid data. Two consecutive, non-overlapping quarter-second samples of the five seconds of data available were digitized for each run. Each sample was manually triggered when the "valid data" signal appeared on the oscilloscope.

Initial analog analyses by AEDC showed that frequencies of interest could be as high as 300 kHz. A minimum sampling rate of 600 kHz was required based on the Nyquist criteria. The DAS was configured to digitize the contents of the tape at 76.9 kHz. Tape speed was slowed to 15 ips from a nominal 120 ips resulting in an effective sampling rate of 615 kHz. This procedure was used because the DAS could sample at 500 kHz or 1 GHZ, and the large volume of data being acquired (210 seconds), necessitated conserving as much storage space as possible. 615 kHz was chosen as the minimum sampling rate possible within the DAS capabilities that still exceeded the 600 kHz requirement.

3.11 Data Analysis Techniques

The analysis described within the Results section used four primary procedures; Fourier transforms, filtering, inverse Fourier transforms, and conditional sampling.

3.11.1 Fourier Transforms

“Fourier analysis is a method of decomposing a signal into a sum of individual components which can easily be produced and observed.”²⁷ Processing the hot wire signal with this method permits determination of the spectra of the disturbances within the boundary layer. This information can then be used to evaluate disturbance growth and amplification rates. The program MatLab by Math Works was utilized on a Sun workstation. The algorithm used to compute the FFT of the data signal (x) is given by

$$X(k+1) = \sum_{n=0}^{N-1} x(n+1)W_n^{kn} \quad (4)$$

where $W_n = e^{-2\pi j/N}$ and N is the length of x . X represents the data signal in the frequency domain while x represents the signal in the time domain. Note the series is written with subscripts of $(n+1)$ and $(k+1)$ instead of the usual n and k . This is because vectors in MatLab run from 1 to N versus 0 to $(N-1)$. The algorithm used to perform the FFT was adjusted for the present study such that an FFT of a sine wave of a fixed amplitude and frequency produced a spike at the correct frequency with a magnitude equal to that of square of the input signal magnitude. This was accomplished by multiplying the resultant FFT by a factor of $2/N$.

3.11.2 Power Spectrum

The power spectrum is a representation of the energy contained within the frequencies of the signal. It is obtained by dividing the signal into sections of 1024 points. Successive sections are Hanning windowed, transformed via the FFT, and accumulated. The 95% confidence interval is estimated by calculating the variance of the unaveraged spectral estimates under the assumption of a normal distribution. The formula used for each power spectra is given by

$$P_{yy} = \frac{X.*conj(X)}{N} \quad (5)$$

3.11.3 Filtering

High pass and low pass filters were employed for the data analysis. A high pass filter processed a signal in the frequency domain and removed all information corresponding to frequencies below the cut off frequency (ω_c) by zeroing out those frequencies. A low pass filter works similarly, except it zeroes out the information in the frequencies above ω_c . Band pass filtering was used to retain only the second mode disturbance information by low passing the signal using the upper frequency of the second mode for ω_c and high passing the new signal using lower frequency of the second mode for ω_c . Notch filtering was used to remove the second mode disturbance information by low passing the signal using the lower frequency of the second mode for ω_c and high passing the new signal using upper frequency of the second mode for ω_c .

3.11.4 Inverse Fourier Transforms

Inverse Fourier transforms (IFT) were also accomplished using MatLab. The formula used to perform this procedure was

$$x(n+1) = \frac{1}{N} \sum_{k=0}^{k-1} X(k+1)W_n^{-kn} \quad (6)$$

The conversion of the signals from the frequency domain to the time domain resulted in the presence of complex components that were 15 orders of magnitude less than their real counterparts. Thus, they were neglected.

3.11.5 Conditional Sampling

The initial step in evaluating the intermittency factor was to determine what constitutes a period of laminar flow and what is a period of turbulent flow. A common procedure for making this evaluation is conditional sampling. This procedure examines the energy signature of flow with respect to time. The energy level of the flow for a window of time (RMS_{local}) is compared to that of the average energy level of the entire data signal (RMS_{mean}). If RMS_{local} exceeds RMS_{mean} by some predetermined threshold (k), a turbulent burst can be identified. The intermittency factor is defined as the percentage of time RMS_{local} exceeds the threshold. Figure 9 demonstrates this concept.

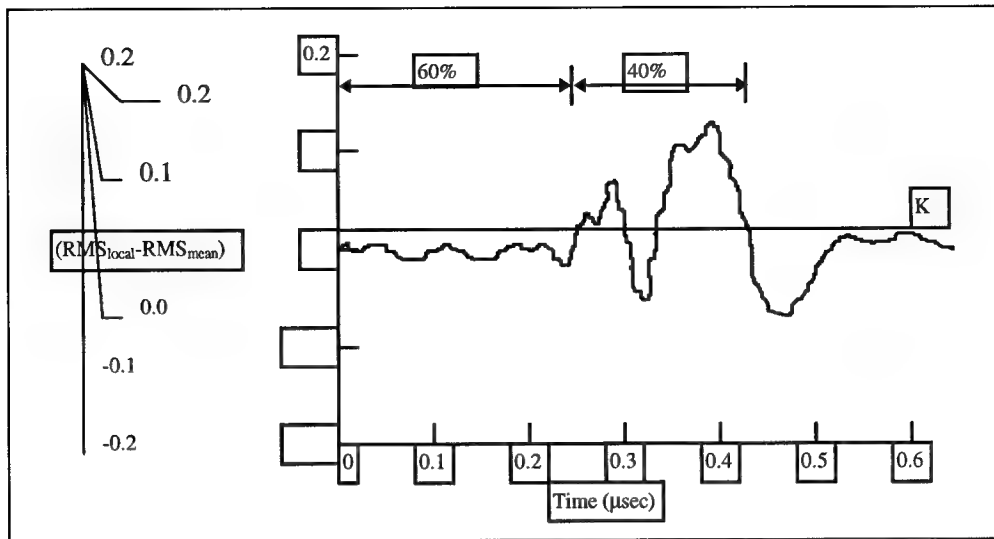


Figure 9 : Conditional sampling for turbulent intermittency factor of 0.4

A major drawback to this method is the determination of the threshold value. As the flow condition transitions from purely laminar flow to fully turbulent flow, RMS_{mean} will rise. That is RMS_{mean} rises with increasing intermittency. The result of this is that if a fixed threshold is used over the entire flow, the calculated intermittency factor will decrease even though the flow is becoming more turbulent. In an ideal situation, the energy level of a purely laminar boundary layer would be available as a reference condition providing some basis for setting the threshold. Even without a laminar reference frame, the determination of the threshold requires some knowledge of the boundary layer being studied. A related concern is the sensitivity of the result to the threshold used. The extent of the error due to the above concerns is difficult to quantify. No attempt at estimating this error was made due to the inability to apply this technique to the data as will be discussed in the next chapter.

The hypersonic transitional flow regime adds an additional complication to this method in the form of the higher mode disturbances. As previously mentioned, second mode disturbances can obtain amplitudes up to eight percent of the mean flow value. The presence of second mode disturbances indicates that the flow has not transitioned to turbulence, yet their energy content can falsely lead to an increase in intermittency factor. This possible source of error was avoided by removing the second mode disturbances from the data signal through digital filtering.

3.11.6 Histogram Analysis

Fully turbulent flow is accepted to be random in nature, and the fluctuations should have a normal distribution. Any deviation from a normal distribution may be indicative that the flow is not fully turbulent. The primary measures for determining how normal a distribution are the skewness and flatness factors. The dimensionless third moment, or skewness factor has a nominal value of zero for a normal distribution, where the dimensionless fourth moment, or flatness factor, has a nominal value of three for a normal distribution. A value less than three for the flatness factor indicates the data in question has an amplitude less than the normal distribution while a value greater than three indicates the data peaks at values higher than the normal distribution.

3.12 Analysis Procedure

The digitized data signal was transformed into the frequency domain via the FFT in order to evaluate the frequency content of the signal. If the disturbances were present, this allowed the determination of their frequencies. The information on disturbance

frequency range was then used to compute two new data signals; one of just the second mode disturbances and the other without the disturbances. This step required respectively band pass filtering and notch filtering the original signal in the Fourier domain. The signal used in the Fourier domain was the FFT of the entire data set, thus no time information would be lost. The filtered signals were then converted back into the time domain. The new data signal, the original with the second mode disturbances removed, was then ready for conditional sampling.

Chapter 4 : Results

This chapter discusses the results of the analysis for the two data sets. The initial data set was used to verify the analysis procedure described in the previous chapter. No conclusions are made with respect to the flowfield due to inconsistencies with this data. The results of the analysis of the primary data set are also presented.

4.1 *Initial Data Set*

The initial data set used to develop the analysis procedure was that of Mach 8.0 flow past a seven degree half-angle cone at a freestream Reynolds number of 4.6 million per meter. Data was available for stations 27 through 37. Each data file contains 160,700 points, so 156 consecutive blocks of 1024 points were transformed and results were averaged. Figure 10 shows the averaged Fourier transforms for stations 15 - 25. This data set was moved to Appendix A due to the inconsistencies mentioned in Chapter 1. The individual stations can be seen in Figures A.1 through Figure A.10 in Appendix A. The normalized error associated with the frequency magnitude is given by $\epsilon_A = 1/\sqrt{N}$ where N is the number of blocks.²⁸ For the present data, ϵ_A is 7.9%.

The results and conclusions presented here are based on the present data analysis. Thus, due to the possible difficulties with the data, no flowfield conclusions will be made. Figures A.12 through Figure A.22 presents the power spectrum of the flow. The power spectrum shows that the energy containing the expected disturbance band, based on the initial analysis of AEDC, has been fully absorbed into the overall profile by station 30.

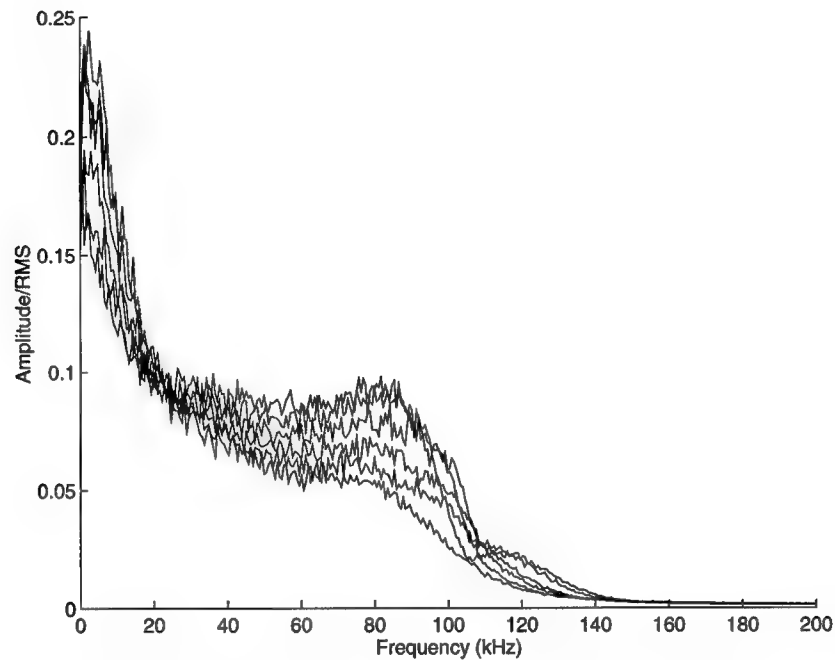


Figure 10 : FFT for odd numbered stations; $Re_{\infty}=4,625,000/m$

Figure A.1 shows a clearly defined peak. The frequency band of this peak was used for all cases. The upper limit of the disturbance was determined to be 110 kHz while the lower limit was set a 65 kHz. This lower limit was set below the lower frequency of the initial station disturbance to account for the shifting of the 2nd mode disturbance to the lower frequencies. Experience has shown the 2nd mode disturbance amplification is dependent upon boundary layer thickness with the frequency of maximum amplification being inversely related to the boundary layer thickness.²¹ This results in a shifting of the 2nd mode peak to the lower frequencies as one progresses downstream.

The filtered data signals can be seen in Figure A.23 through Figure A.33.

Examination of the second mode disturbance frequency band signal shows the results of the “disturbances” passing the station. Referring to Figures A.23 through Figure A.33, it

is seen that amplitudes of the disturbances are growing with station position.

Examination of the data signal with the second mode disturbances removed shows minimal differences compared to the raw data signal. Figures A.34 through Figures A.44 contain the results of this analysis. The skewness factors are shown in Figure A.45 and the flatness factors are shown in Figure A.46 for each station.

The filtered data signal is ready for conditional sampling and a determination of the intermittency factor. However, the lack of clearly defined turbulent bursts makes determination of a reasonable threshold impossible. Whether this is true for highly transitional flows in general, or is a result of possible data contamination, is uncertain.

The above analysis would indicate fully turbulent flow, however, the flow conditions for which the data was collected were thought to be laminar. This has resulted in some discussion as to the differences. Initial analog examination of the data by the collection agency, AEDC, showed distinct second mode disturbances at all stations. Figures A.47 through Figures A.57 contain this information. However, the results of the present analysis, which have been verified by the project sponsor and thesis advisor, do not show the 2nd mode peaks. The collection agency has rechecked their analyses and confirmed their original results. This matter is further clouded by examination of an additional set of data, to be discussed next, whose FFT results were matched by all parties involved. No explanation for this difference is offered here.

4.2 Primary Data Set

The second set of data analyzed in an effort to confirm the analysis procedure and examine the flow field phenomena was that of station 35, where the Reynolds number was varied. The test setup used was the same as for the previous data set. The different Reynolds numbers used were 3.28, 3.94, 4.92 and 6.56 million per meter.

4.2.1 Velocity Profiles

Figure 11 shows the mean velocity profiles for each of the data sets. The profiles show that the mean flow is laminar (or very early in transition) for $Re/m = 3.28$ and 3.94 million. The $Re/m = 6.56$ million profile indicates a fully turbulent (or nearly fully turbulent) flow. The $Re/m = 4.92$ million profile falls in between the laminar and turbulent cases, indicating that the flow is transitional.

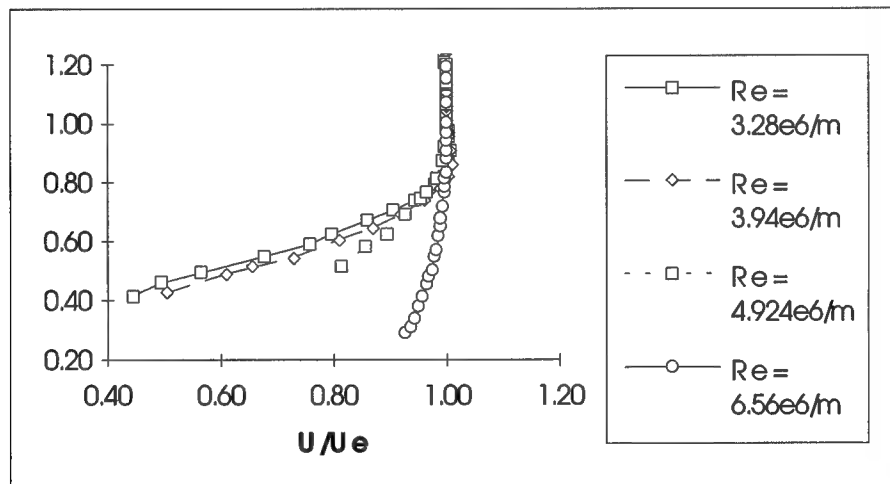


Figure 11: Boundary Layer Velocity Profiles for Varying Reynolds Number

4.2.2 Schlieren Photographs

Figure 12 and Figure 13 shows the flowfield for 3.28 million per meter and Figure 14 and Figure 15 shows the flowfields for 4.92 million per meter. No photographs are available for the 3.94 million per meter case.

The boundary layer remains thin along the length of the model and shows signs of “rope like” waves indicative of second mode disturbances near the aft end of the model for Reynolds numbers of 3.28 and 4.92 million per meter in both the forward and aft views. Figure 16 and Figure 17 shows the flowfield for 6.56 million per meter. The aft view shows an initially thin boundary layer with clearly defined disturbances that gradually dissipate into a thick boundary layer lacking discernible features. The forward view also shows the transition from a laminar boundary layer to a turbulent boundary layer, but no disturbance waves can be identified.

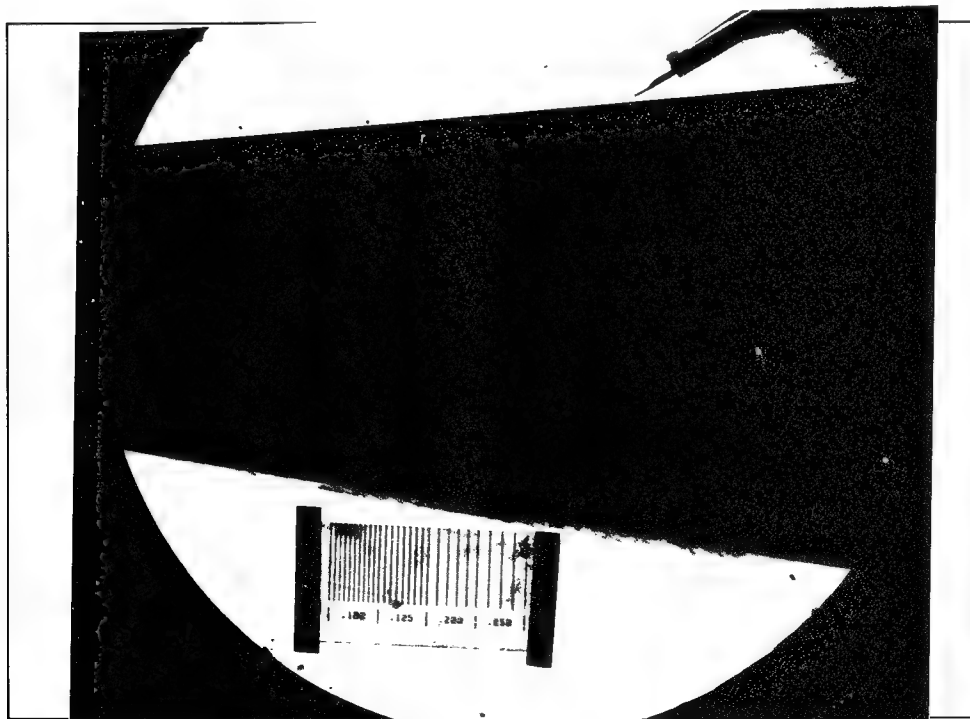


Figure 12: Flowfield for $Re_{\infty} = 3,280,000/m$, Front View

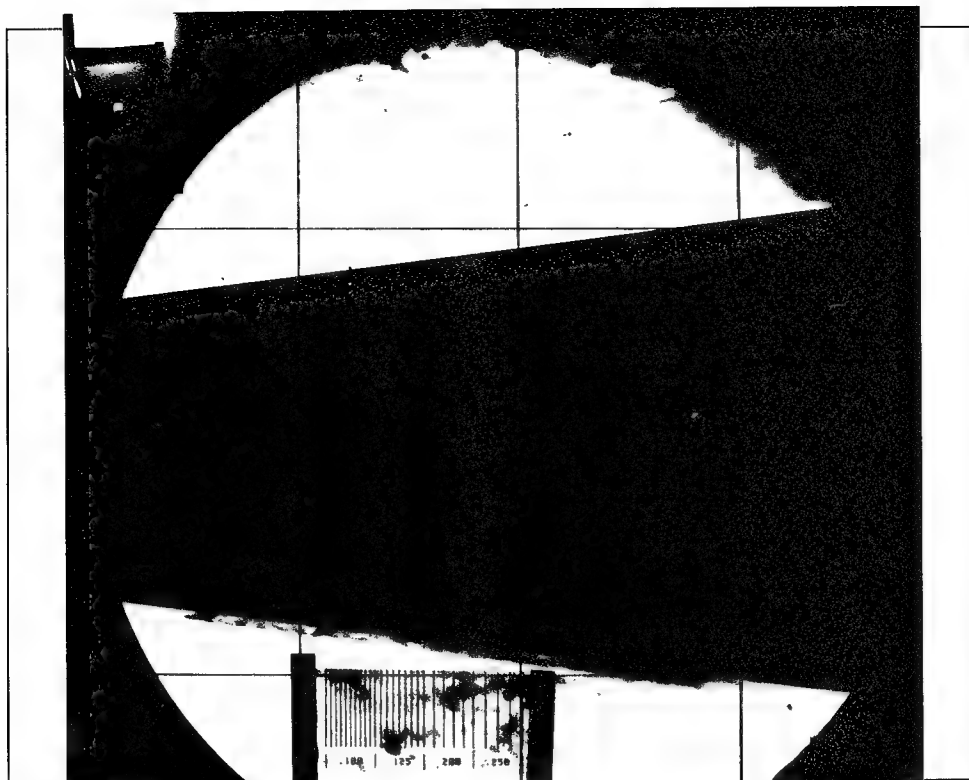


Figure 13: Flowfield for $Re_{\infty} = 3,280,000/m$, Aft View

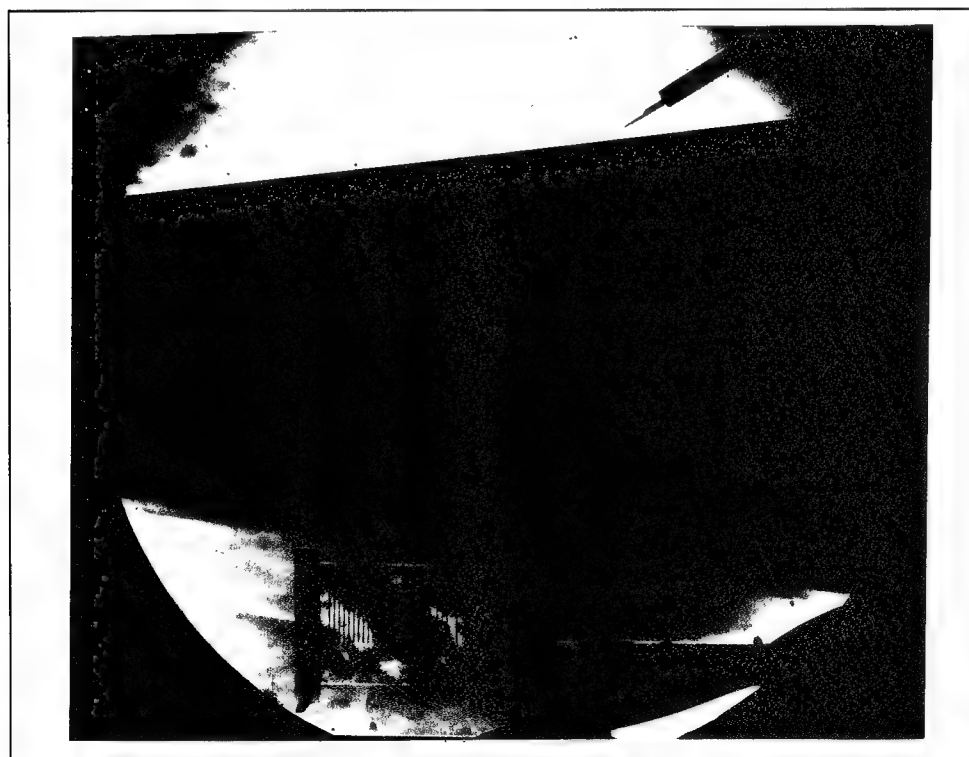


Figure 14: Flowfield for $Re_{\infty} = 4,92e6/m$, Front View

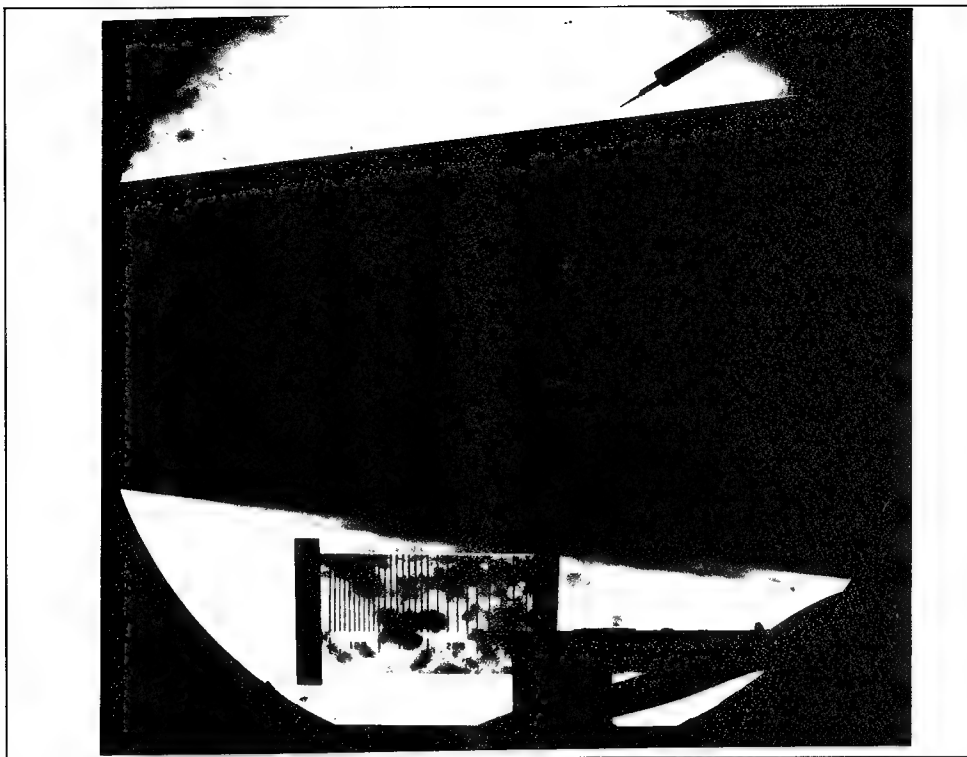


Figure 15: Flowfield for $Re_{\infty} = 4,920,000/m$, Aft View

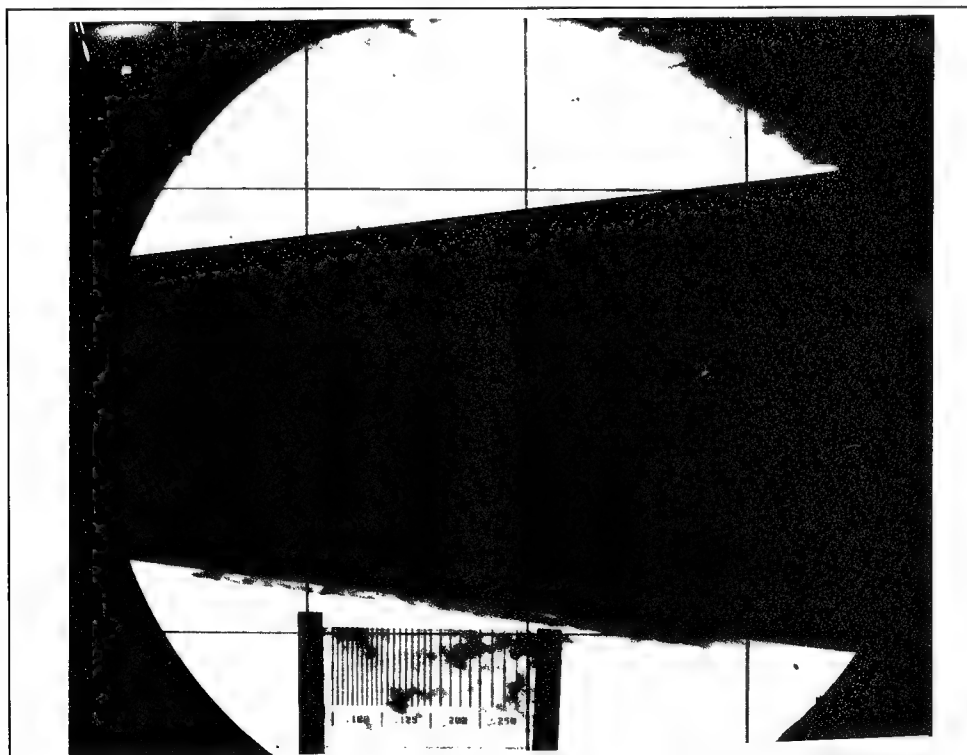


Figure 16: Flowfield for $Re_{\infty} = 6,560,000/m$, Front View

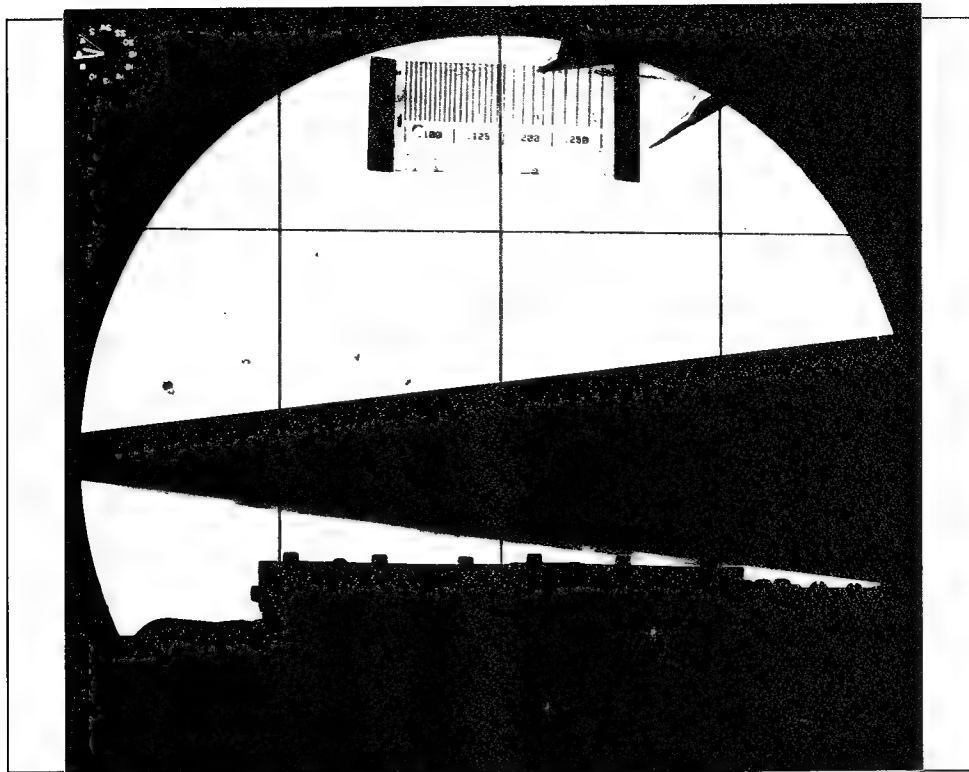


Figure 17: Flowfield for $Re_\infty = 6,560,000/m$, Aft View

4.2.3 Spectral Analysis

Figures 18 through Figure 21 contain the results of the Fourier analysis and Figures 22 through Figure 25 contain the results of the power spectrum. A distinct second mode disturbance energy containing band exists for the Reynolds numbers of 3.28 million per meter case only. The higher Reynolds number data shows no distinct peaks to identify the second mode frequency range. This can be taken to indicate that the flow is predominately turbulent. The power spectrum of a fully turbulent flow is uniform over the range of energy containing frequencies with no one frequency containing significantly more energy than any other frequency. This is because turbulent flow is accepted as being random in nature and the energy contained in the flow will be spread

uniformly among all the frequencies. The general shape of the power spectrum curves of Figures 23 through Figure 26 suggests that the flow is generally turbulent because these curves show the energy content of the flows to be distributed uniformly. This is in direct contrast to the velocity profiles for the Reynolds numbers of 3.94 and 4.92 million per meter that show the mean flow to be laminar or transitional. This indicates a limitation to using the power spectrum as a means to identify a turbulent flow regime.

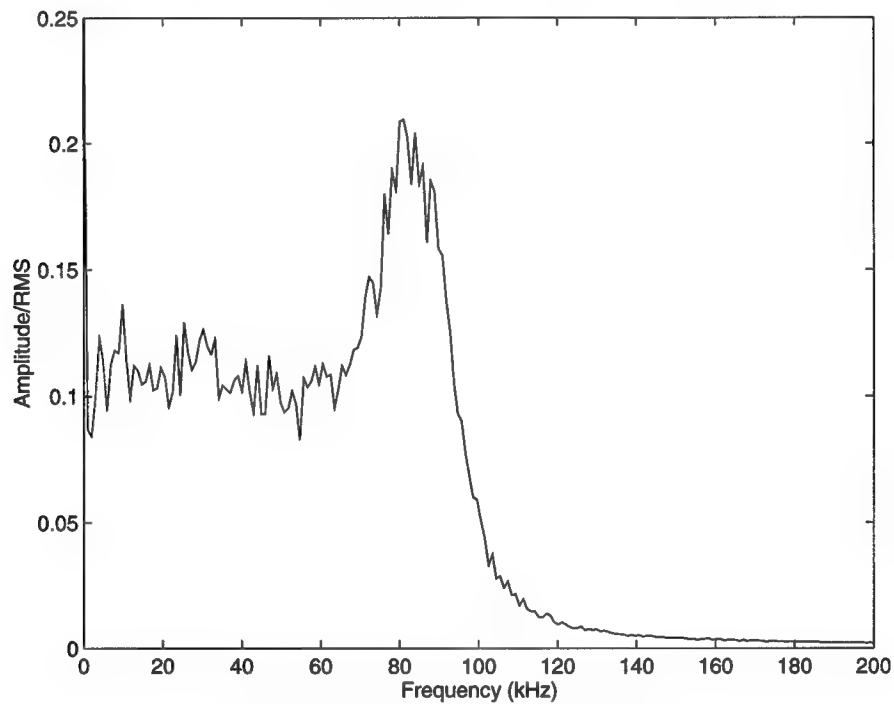


Figure 18: FFT for $Re_\infty = 3,280,000/m$

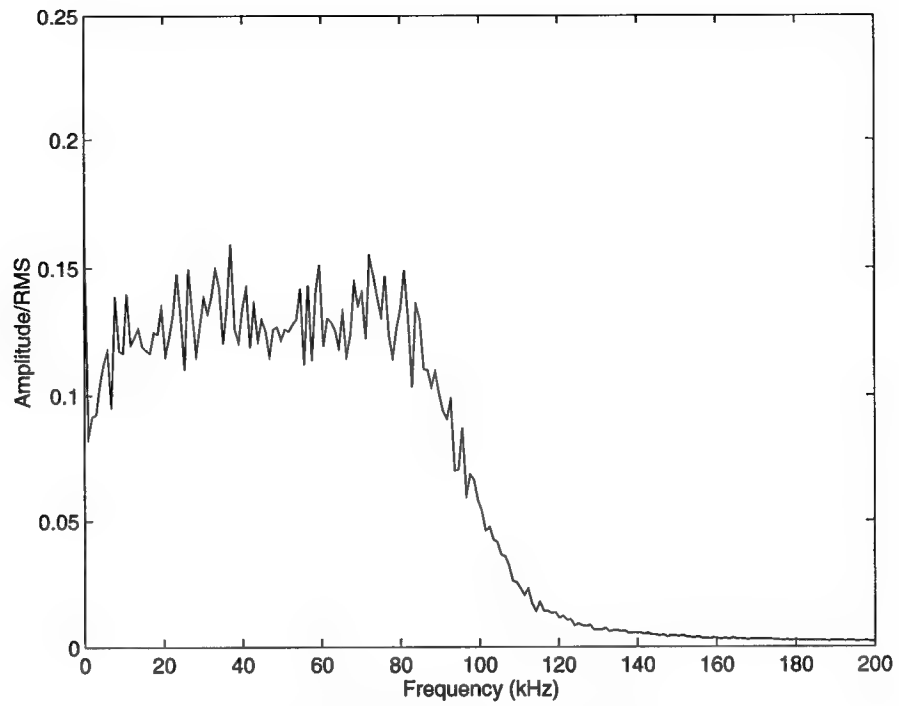


Figure 19: FFT for $Re_\infty = 3,940,000/m$

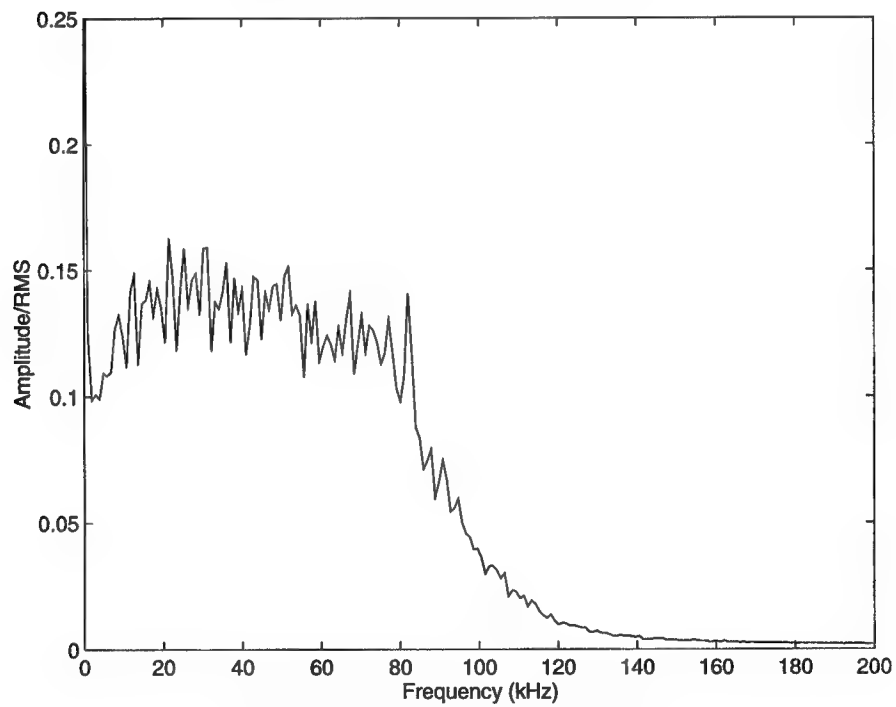


Figure 20: FFT for $Re_\infty = 4,920,000/m$

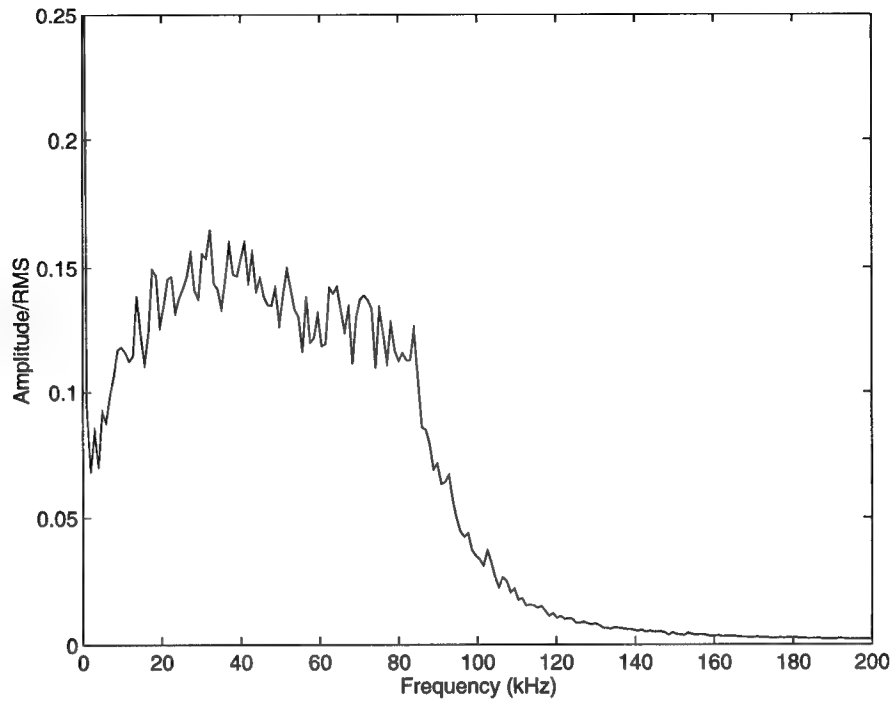


Figure 21: FFT for $Re_\infty = 6,560,000/m$

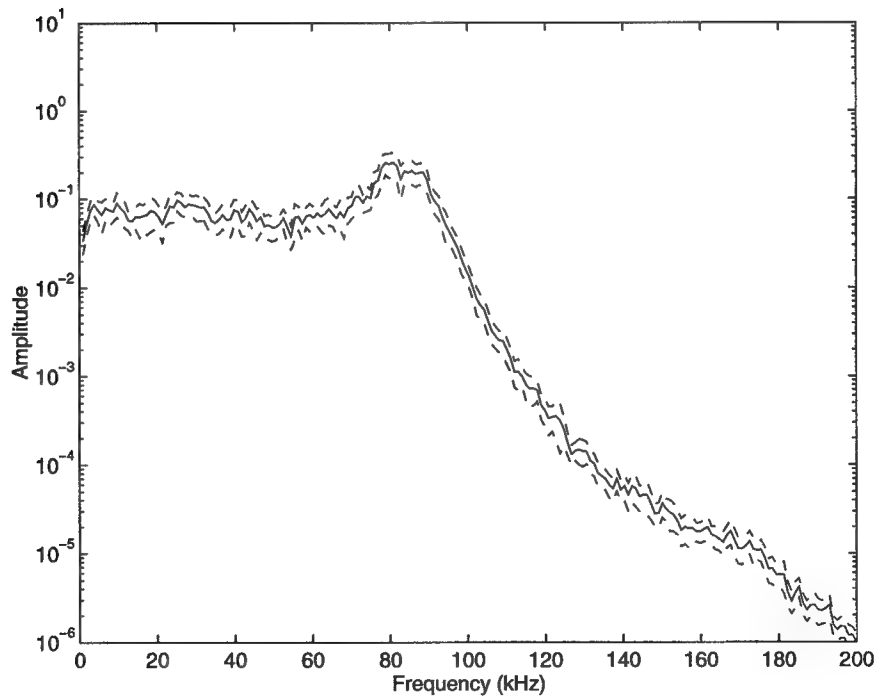


Figure 22: Power Spectra for $Re_\infty = 3,280,000/m$

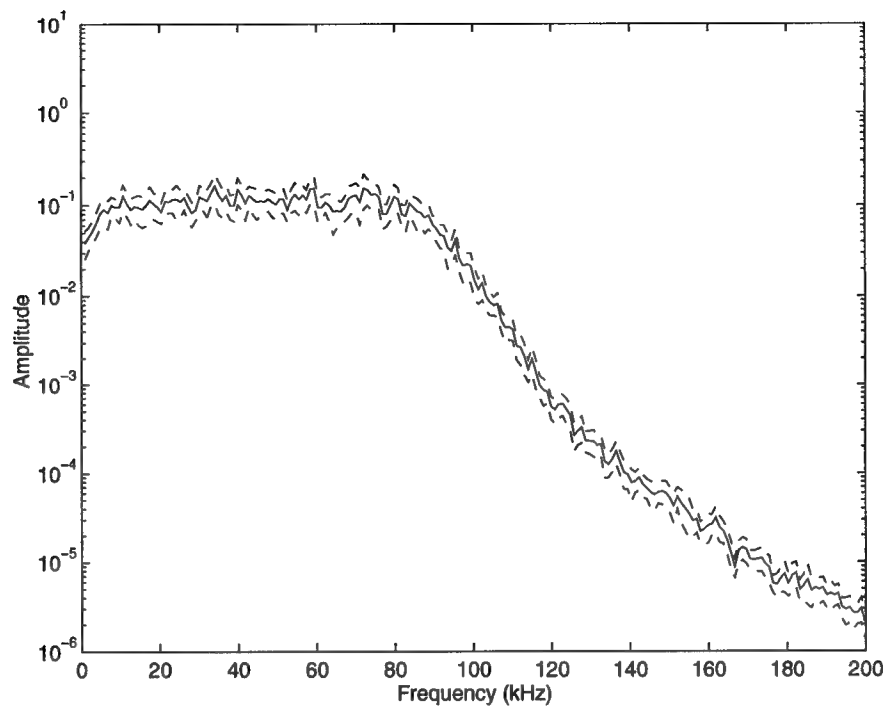


Figure 23: Power Spectra for $Re_\infty = 3,940,000/m$

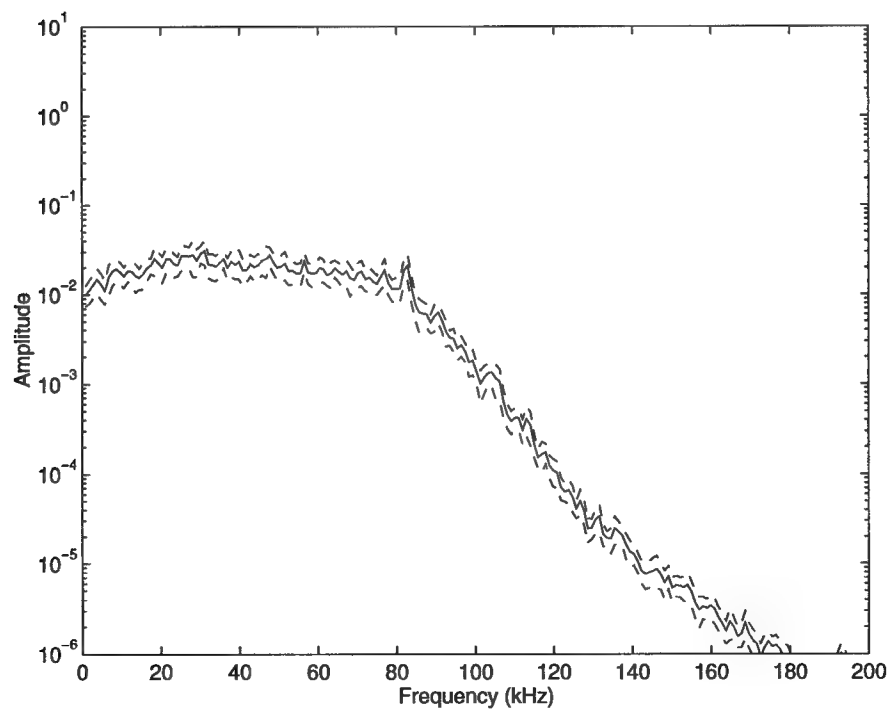


Figure 24: Power Spectra for $Re_\infty = 4,920,000/m$

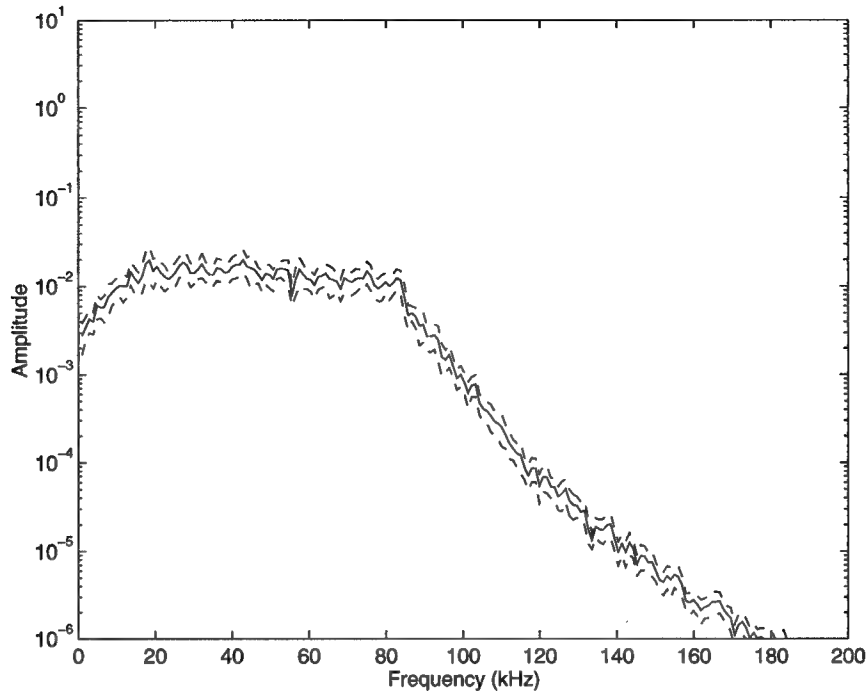


Figure 25: Power Spectra for $Re_{\infty} = 6,560,000/m$

4.2.4 Histogram Analysis

Another method for determining the turbulence of the flow is to compare the distribution of the deviations in mass flux to a random (Gaussian) distribution. Figures 26 through Figure 29 contain the histogram analysis for the primary data set. Qualitative examination of these figures shows the deviations in mass flux to have a nominally Gaussian distribution. The data departs from a normal distribution as measured by the skewness and the flatness which are shown in Figure 30 and Figure 31 respectively. As the flow regime transitions from laminar to turbulent, the distributions begin to more closely approximate a Gaussian distribution. The flatness factor shows a continuous increase with increasing Reynolds number. This can be seen in the

histograms, that as the Reynolds number increases, the histogram peak approaches, and eventually exceeds the Gaussian curve. The skewness factors show an overall trend of increasing with increasing Reynolds number. The Reynolds number of 6.56 million per meter case should have skewness and flatness factors of zero and three respectively due to its turbulent nature, as evidenced by the mean velocity profile shown in Figure 11. This departure from nominal values suggests that the flow may not be fully turbulent.

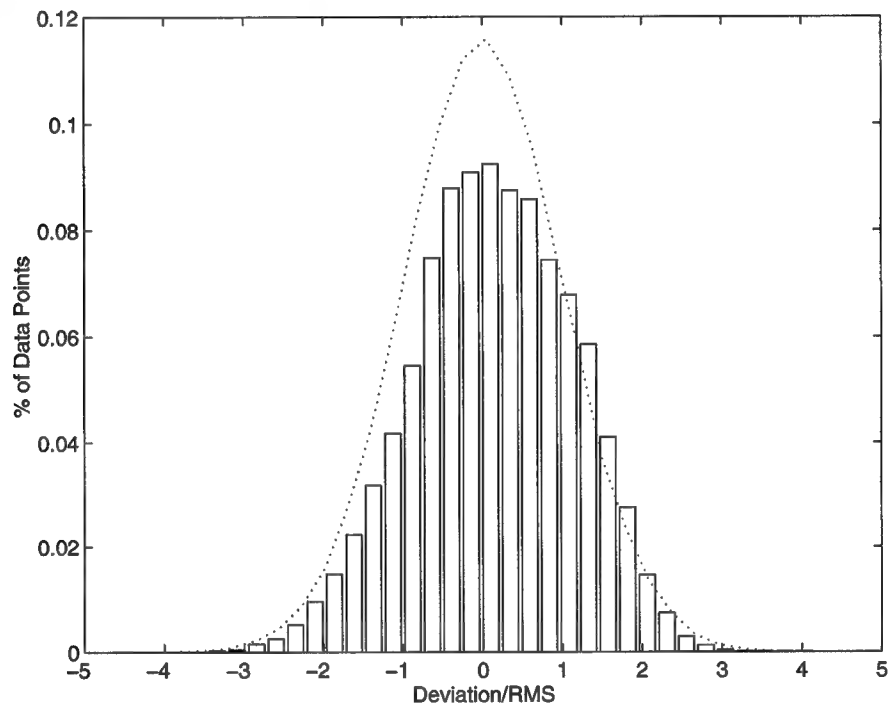


Figure 26: Histogram for $Re_\infty = 3,280,000/m$

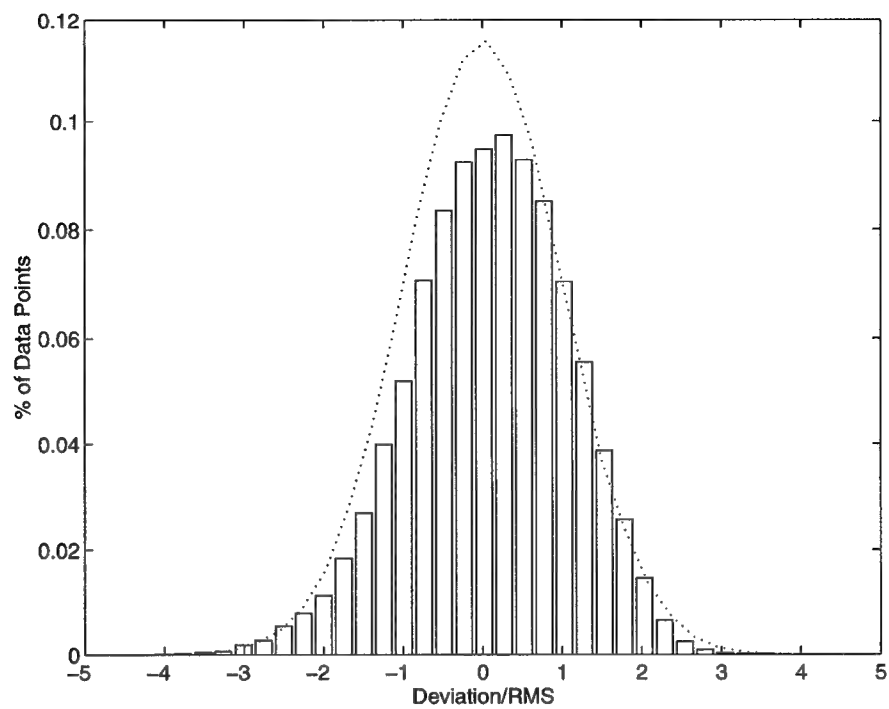


Figure 27: Histogram for $Re_\infty = 3,940,000/m$

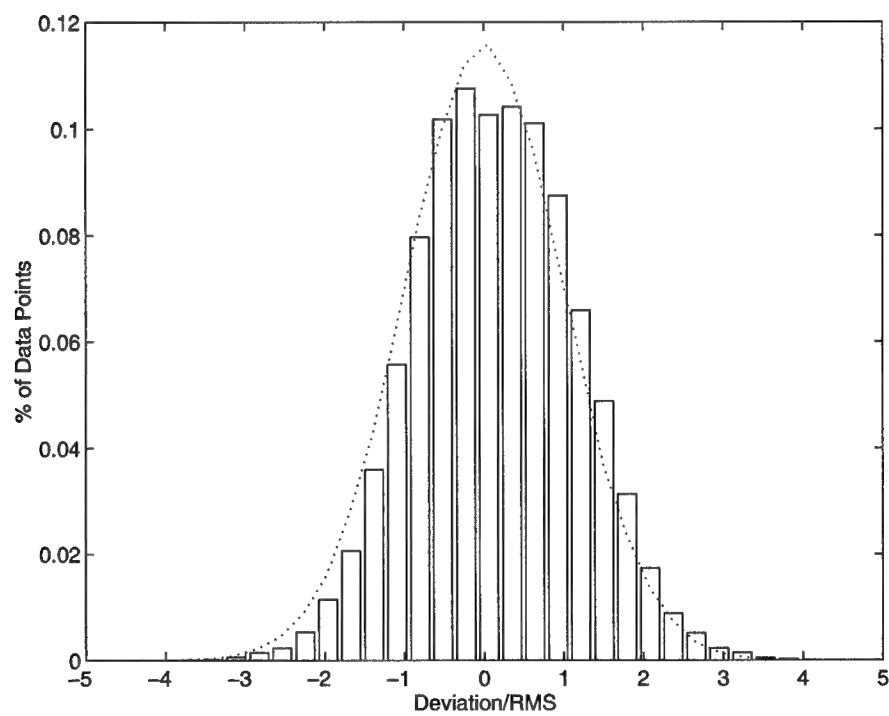


Figure 28: Histogram for $Re_\infty = 4,920,000/m$

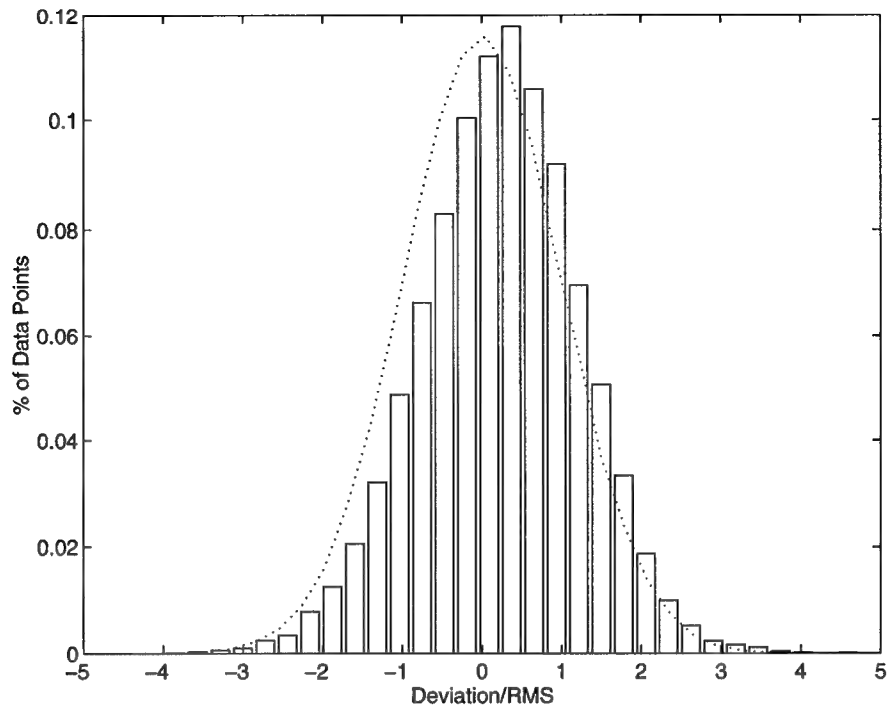


Figure 29: Histogram for $Re_\infty = 6,560,000/m$

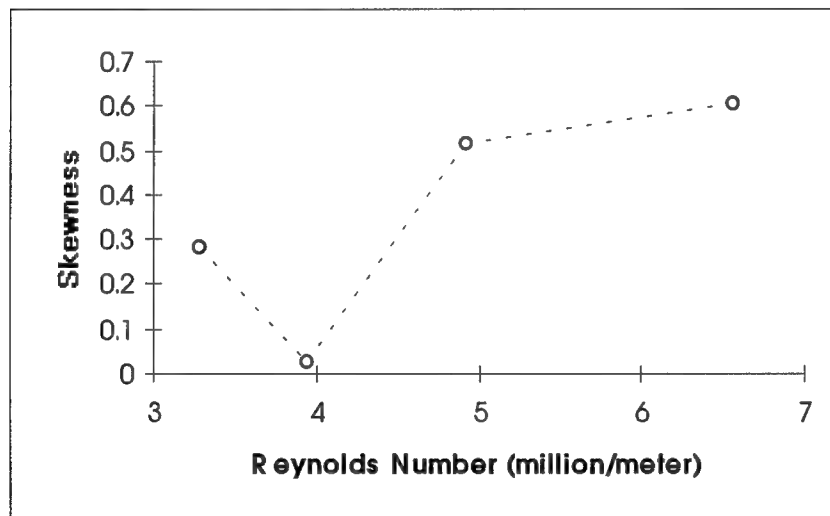


Figure 30: Skewness Factor for Station 35

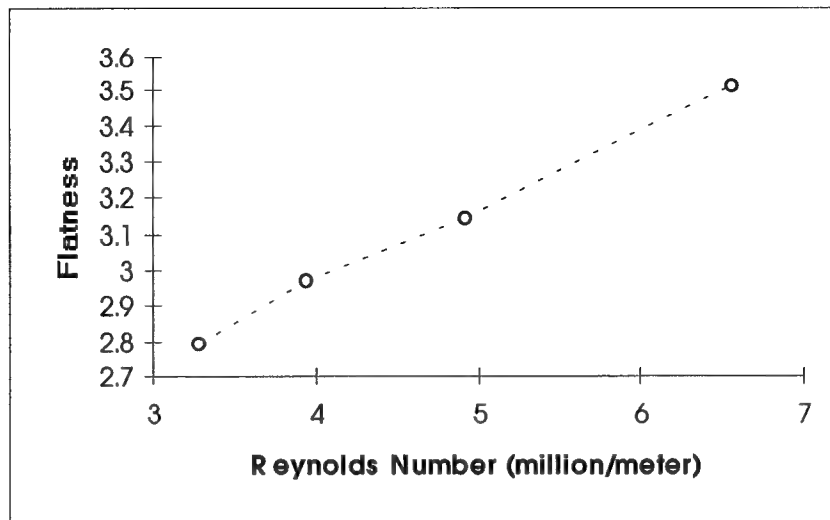


Figure 31: Flatness Factor for Station 35

4.2.5 Conditional Sampling

The data sets were run through the analysis procedure developed for the initial data set. Based upon the spectral analysis, it was assumed that the second mode disturbances were present, and that they would fall between 70 kHz and 105 kHz for all four cases. The frequency range was chosen based upon the power spectra for the Reynolds number of 3.56 million per meter case. Figures 32 through Figure 35 contain the results. Examination of the data signals again shows the removal of the second mode disturbances only to have a marginal impact on the general trends of the raw data signal. However, the removal of the disturbances results in a cleaner signal. The most dramatic result of the removal occurs for a Reynolds number of 3.28 million per meter. In this case the energy content of the second mode is on the same order as the remainder of the signal.

Figure 33 shows that the 2nd mode disturbances have decreased in amplitude compared to the previous figure. The same result holds true for Figure 34. The disturbances seen in the Reynolds numbers of 4.92 and 6.56 million per meter cases are essentially the same. All three cases show only a marginal benefit from the removal of the disturbances from the original signal. Not surprisingly, the benefit derived from the removal of the disturbances is directly related to magnitude of the disturbances. This benefit decreases with increasing Reynolds number for this data set

The time plots of the disturbances reveal a drop in the relative amplitude of the disturbances as the Reynolds number increased. This is due in part to the lack of energy within the chosen frequency band as evidenced by the power spectrums of Figures 22 through Figure 25. It is a due result of the shifting to the lower frequencies of the disturbance amplification. Finally, the disturbances may be smaller because as the flow transitions to turbulence, the coherent second mode disturbance structures break down and the energy dissipates to the lower frequencies.

Attempts at conditional sampling were unsuccessful for the same reasons as in the initial data set; no criteria could be established for a threshold. This suggests that the technique of conditional sampling may not be applicable to hypersonic transitional flow.

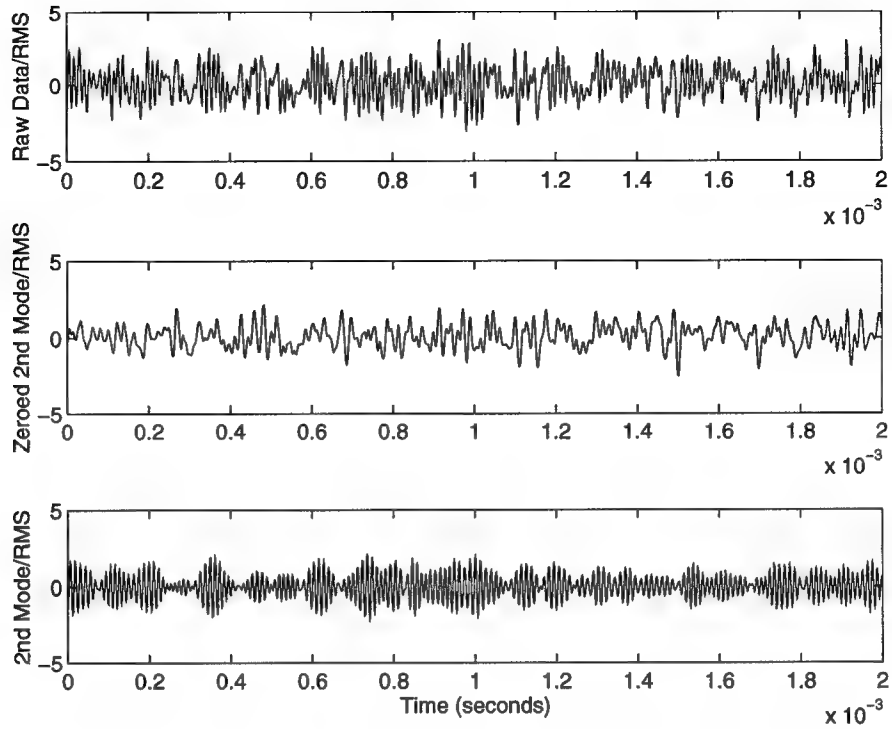


Figure 32: Data Signals for $Re_{\infty} = 3,280,000/m$

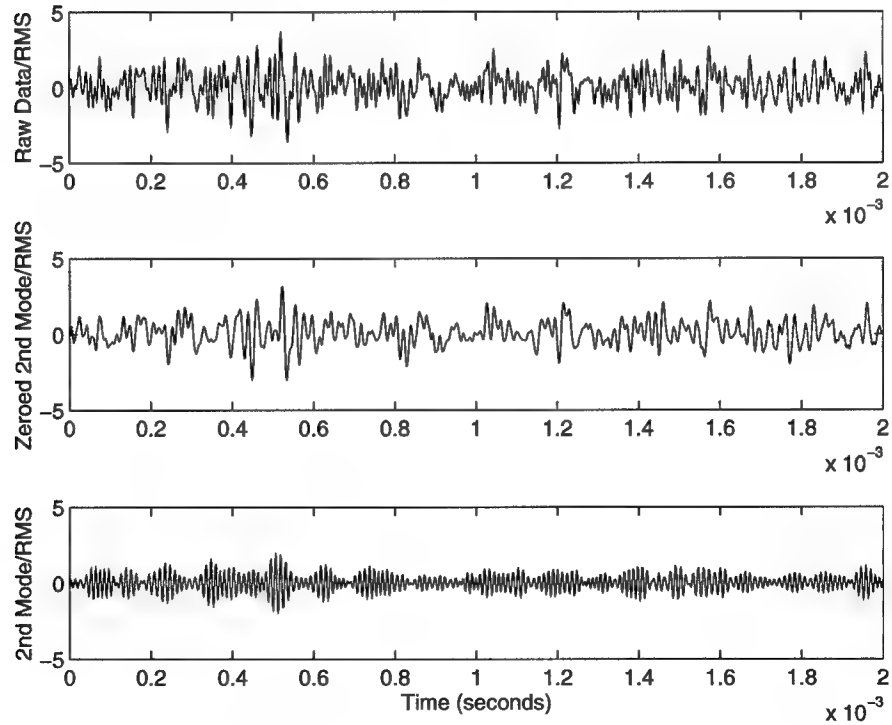


Figure 33: Data Signals for $Re_{\infty} = 3,940,000/m$

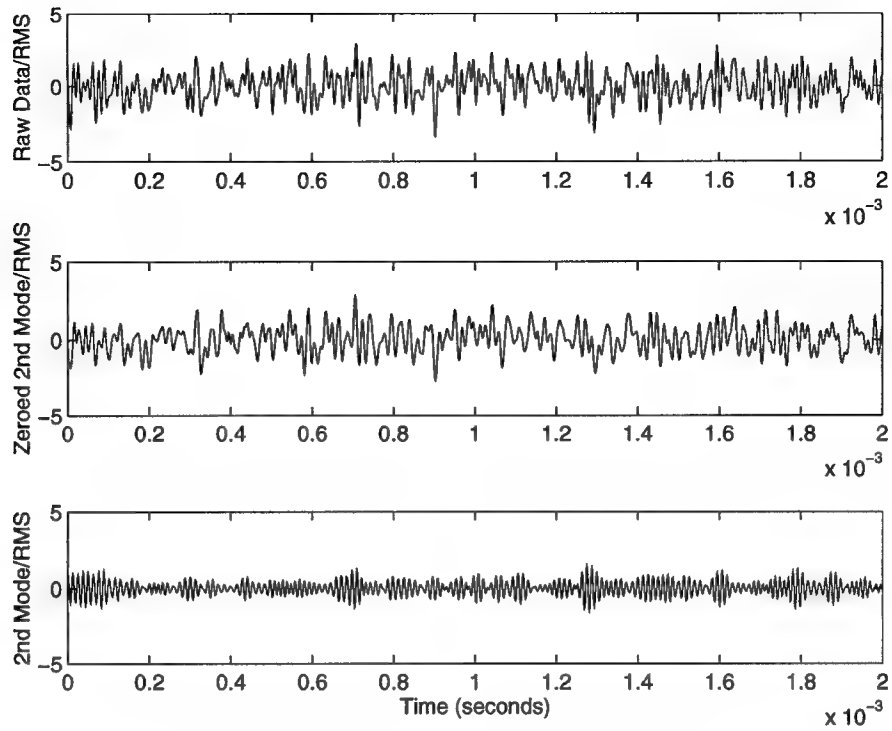


Figure 34: Data Signals for $Re_\infty = 4,920,000/m$

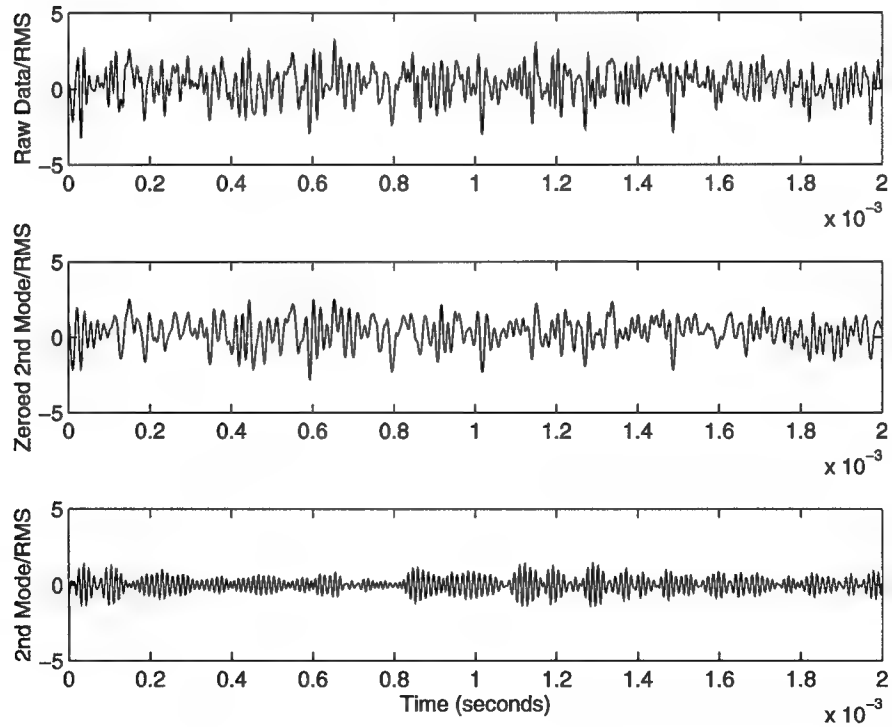


Figure 35: Data Signals for $Re_\infty = 6,560,000/m$

4.2.6 Turbulent Bursting

Examination of the second mode disturbance signals and the corresponding total flow signals show the influence of the second mode to be on the same order as the total signal. This supports the need to remove the second mode disturbances from the signal to accurately assess the turbulent bursting phenomena. However, the signal with the second mode disturbance removed did not show any evidence of turbulent bursting. As thus, conditional sampling techniques proved to be not applicable. This was due mainly to the fact that no threshold value could be determined showing the occurrence of a turbulent burst. Photographs of the flow fields for the secondary data set also show no evidence of turbulent bursting. This means that the convention of turbulent bursting, or using a flow intermittency factor to determine flow properties, were not confirmed by the data analysis.

Chapter 5 : Conclusions

A procedure was developed to determine the intermittency of a transitioning boundary layer in hypersonic flow. Flow in this regime contains higher order disturbances, with the second mode being the most unstable, that can obtain magnitudes up to eight percent of the mean value. These disturbances must be removed to obtain an accurate value of the intermittency.

The initial data set used to develop this procedure showed only a marginal benefit from this processing. Questions about the validity of the data make any other conclusions impossible. The second set of data showed similar results from the analysis. Filtering out the second mode disturbances removed some of the noise from the data signal, but the resulting signal did not show any evidence of intermittency.

Examination of the power spectrum or the Fourier analysis can be used to label a flow as containing significant second mode disturbance energy and corresponding to this, be laminar. However, it would be incorrect to label the flow turbulent simply because the profile contains no evidence of second mode disturbance energy.

Finally, it has been assumed that the transition process in hypersonic flow contains turbulent bursting. Analysis of this data and photographs of the flow are unable to support this assumption.

Chapter 6 : Recommendations

The uncertainty in expanding concepts from lower speed flows to the hypersonic regime has been proven repeatedly. Added to this is the limited data base available for study. Additional transition data is required in this area. Two areas that would have been beneficial in the analysis are data for laminar flow and data taken closer to the surface.

No information was available for a laminar flow field (i.e. an upstream station) or that of the freestream. Subtraction of the laminar signal from the station of interest in the Fourier domain returns a signal without the lower frequency information. This would be useful for determining the second mode disturbance frequency range even in a noisy signal. Information on the freestream would be useful for correlating disturbance growth with that of the initial disturbances.

Secondly, the data used in this study was obtained at the maximum energy point of the flow which is in close proximity to the boundary layer edge. The second mode disturbances reach maximum amplitude at the boundary layer edge. A more suitable location for taking transition data may be near the surface, where the influence of the second mode disturbances is minimal.

References

- ¹Mack, L.M., "Linear Stability Theory and the Problem of Supersonic Boundary Layer Transition," AIAA Journal, Vol. 13, No. 3, March 1975, pp 278-289.
- ²Prandtl, L., "Bemerkungen uber die Entstehung der Turbulenz," Zeitschrift fuer Angewandte Mathematik und Mechanik, Vol 1, 1921, pp 431-436.
- ³Schubauer, G.B. and Skramstad, H.K., "Laminar Boundary Layer Oscillations and Transition on a Flat Plate," Rept. 909, 1948, NACA.
- ⁴Spangler, J.G. and Wels, C.S., Jr., "Effect of Freestream Disturbances on Boundary Layer Transition," AIAA Journal, Vol. 6, No. 3, March 1968, pp 543-545.
- ⁵Bennett, H. W., "An Experimental Study of Boundary Layer Transition," Kimberley-Clark Corp. Rept. Neenah, Wis., 1953.
- ⁶Jackson, F.J. and Heckl, M.A., "Effect of Localized Acoustic Excitation on the Stability of a Laminar Boundary Layer," Rept. 62-362, June 1962, Aeronautical Research Lab., Wright-Patterson AFB, Ohio.
- ⁷Kendall, J.M., "Supersonic Boundary Layer Stability Experiments," Proceedings of Boundary Layer Transition Study Group Meeting, Vol II, Aerospace Corporation, August 1967.
- ⁸Kendall, J.M., "Wind Tunnel Experiments Relating to Supersonic and Hypersonic Boundary Layer Transition," AIAA Journal, Vol. 13, No.3, March 1975, pp 290-299.
- ⁹Demetriades, A., "An Experimental Investigation of the Stbility of the Laminar Hypersonic Boundary Layer," GALCIT Hypersonic Research Project, Memorandum No. 43, 1958.
- ¹⁰Demetriades, A., "An Experiment on the Stability of Hypersonic Laminar Boundary Layers," Journal of Fluid Mechanics, Vol. 7, Part 3, March 1960.
- ¹¹Demetriades, A., Boundary Layer Instability Observations at Mach Number 7," Journal of Fluid Mechanics, ASME, Vol. 99, No. 1, March 1977.
- ¹²Demetriades, A., "New Experiments on Hypersonic Boundary Layer Stability Including Wall Temperature Effects," Proceedings of the Heat Transfer and Fluid Mechandics Institute, pp 39-54, 1978.

¹³Stetson, K.F., Thompson, E.R., Donaldson, J.C., and Siler, L.G., "Laminar Boundary Layer Stability Experiments on a Cone at Mach 8, Part 1: Sharp Cone," AIAA Paper No. 83-1761, July 1983.

¹⁴Stetson, K.F., Thompson, E.R., Donaldson, J.C., and Siler, L.G., "Laminar Boundary Layer Stability Experiments on a Cone at Mach 8, Part 3: Sharp Cone at Angle of Attack," AIAA Paper No. 85-0492, January 1985.

¹⁵Stetson, K.F., Thompson, E.R., Donaldson, J.C., and Siler, L.G., "Laminar Boundary Layer Stability Experiments on a Cone at Mach 8, Part 4: On Unit Reynolds Number and Environmental Effects," AIAA Paper No. 86-1087, May 1986.

¹⁶Stetson, K.F., Thompson, E.R., Donaldson, J.C., and Siler, L.G., "On Hypersonic Transition Testing and Prediction," AIAA Paper No. 88-2007, May 1988.

¹⁷Stetson, K.F., "On Nonlinear Aspects of Hypersonic Boundary Layer Stability," AIAA Journal, Vol. 26, No. 7, pp 883-885, July 1988.

¹⁸Stetson, K.F., Thompson, E.R., Donaldson, J.C., and Siler, L.G., "Laminar Boundary Layer Stability Experiments on a Cone at Mach 8, Part 5: Tests with a Cooled Model," AIAA Paper No. 89-1985, June 1989.

¹⁹Stetson, K.F., Kimmel, R.L., Thompson, E.R., Donaldson, J.C., and Siler, L.G., "A Comparison of Planar and Conical Boundary Layer Stability and Transition at a Mach Number of 8," AIAA Paper No. 91-1639, June 1991.

²⁰Kimmel, R.L., and Kendall, J.M., "Nonlinear Disturbances in a Hypersonic Laminar Boundary Layer," AIAA Paper No. 91-0320, January 1991.

²¹Stetson, K.F., and Kimmel, R.L., "On Hypersonic Boundary Layer Stability," AIAA Paper No 92-0737, January 1992.

²²Schetz, Joseph A., Boundary Layer Analysis. Prentice-Hall, Inc., NJ. 1992.

²³White, Frank M., Viscous Fluid Flow. 2nd ed. McGraw-Hill, Inc. NY, NY. 1991.

²⁴Lees, L. and Lin, C.C., "Investigation of the Stability of the Laminar Boundary Layer in a Compressible Fluid," TN-1115, Sept. 1946, NACA.

²⁵Doughman, E.L., "Development of a Hot-Wire Anemometer for Hypersonic Turbulent Flows". The Review of Scientific Instruments, Vol. 43, No.8, August 1972, pp. 1200-1202.

²⁶Donaldson, J.C., Nelson, C.G., and O'Hare, J.E., "The Development of Hot-Wire Anemometer Test Capabilities for $M_\infty=6$ and $M_\infty=8$ Applications". AEDC-TR-76-88 (AD A029570), September 1976.

²⁷ Bellanger, M., Digital Processing of Signals Theory and Practice. 2ed John Wiley & Sons Ltd. New York, New York, 1989.

²⁸ Bendat, J.S. and Piersol, A.G., Random Data Analysis and Measurement Procedures. 2ed. John Wiley & Sons Ltd. New York, New York, 1986.

²⁹ Stetson, K.F., and Rushton, G.H., "A Shock Tunnel Investigation of the Effects of Nose Bluntness, Angle of Attack and Boundary Layer Cooling on Boundary Layer Transition at a Mach Number of 5.5," AIAA Paper 66-495, June 1966.

³⁰ Evvard, John C., "The Effects of Extreme Cooling on Boundary-Layer Transition at Supersonic Speeds," Paper presented at the American Physical Society Meeting, New York, January 31, 1957.

³¹ Dianconis, N.S., Jack, J.R., and Wisniewski, R.J., "Boundary-Layer Transition at Mach 3.12 as Affected by Cooling and Nose Blunting," NACA TN 3928, January 1957.

³² Jack, J.R., Wisniewski, R.j., and Dianconis, N.S., "Effects of Extreme Surface Cooling on Boundary-Layer Transition," NACA TN 4094, October 1957.

Appendix A : Initial Data Set

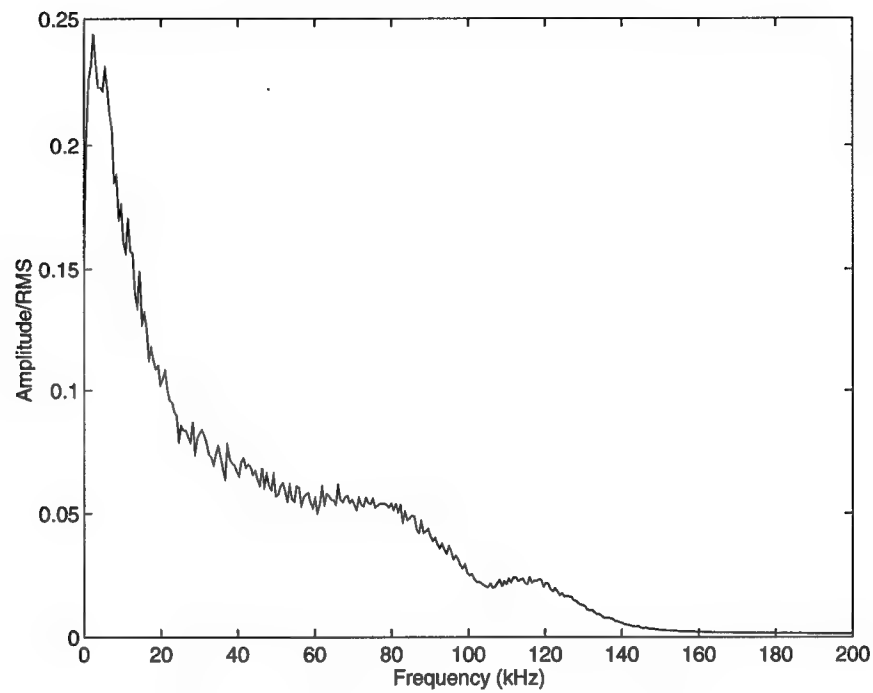


Figure A.1: FFT for Station 27; $Re_{\infty}=4,265,000/m$

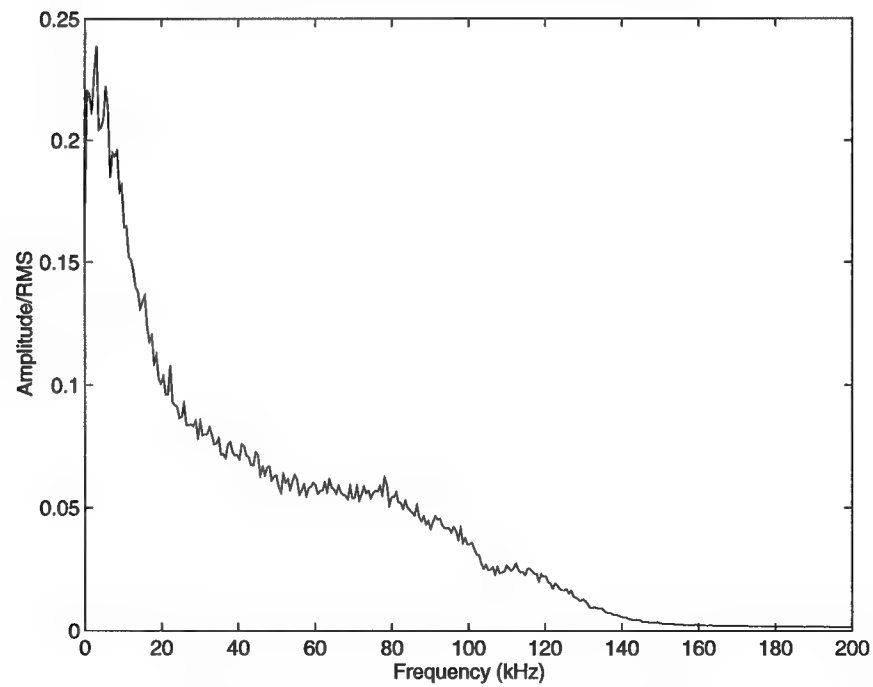


Figure A.2 : FFT for Station 28; $Re_{\infty}=4,265,000/m$

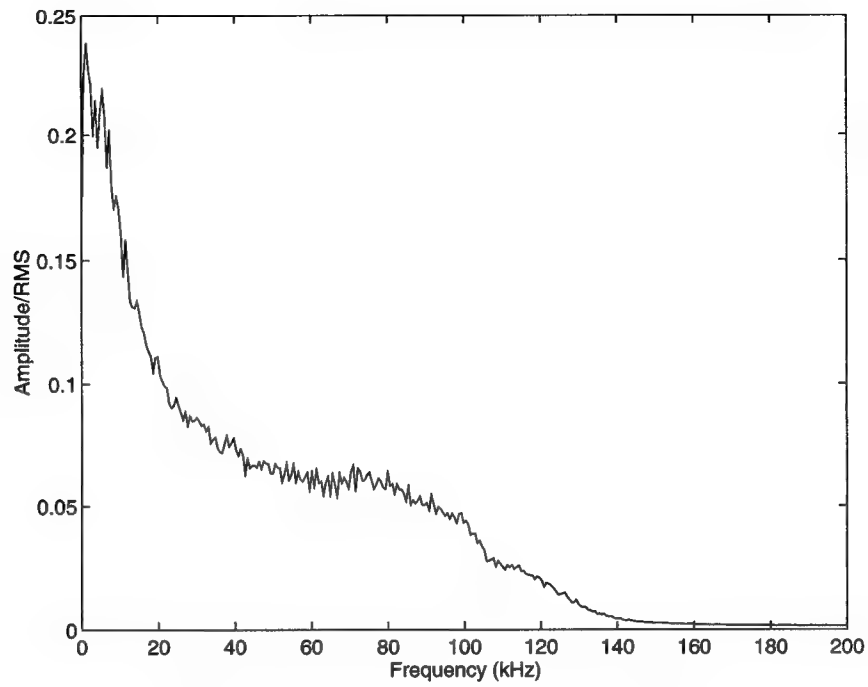


Figure A.3 : FFT for Station 29; $Re_\infty=4,265,000/m$

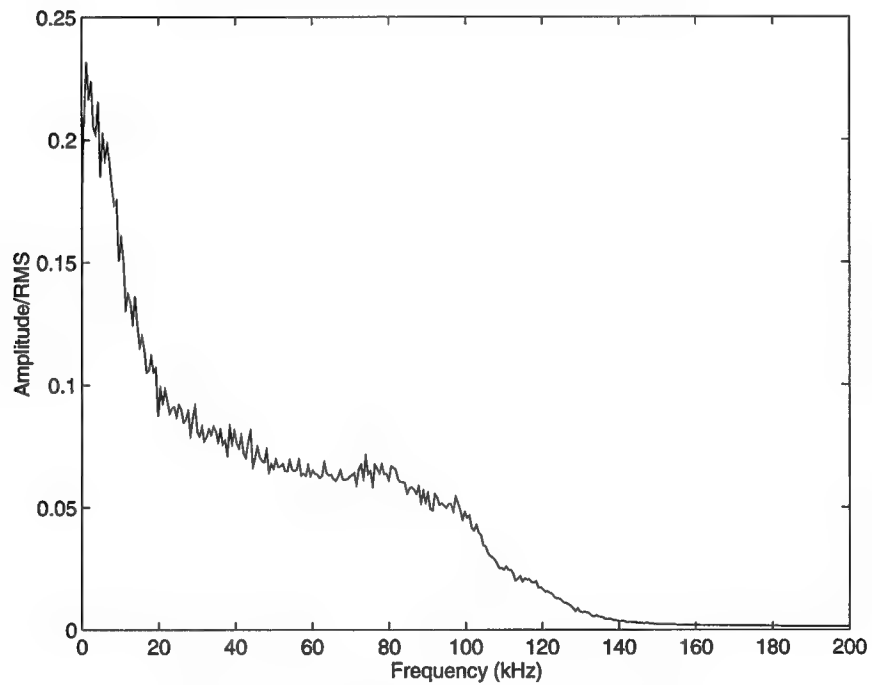


Figure A.4 : FFT for Station 30; $Re_\infty=4,265,000/m$

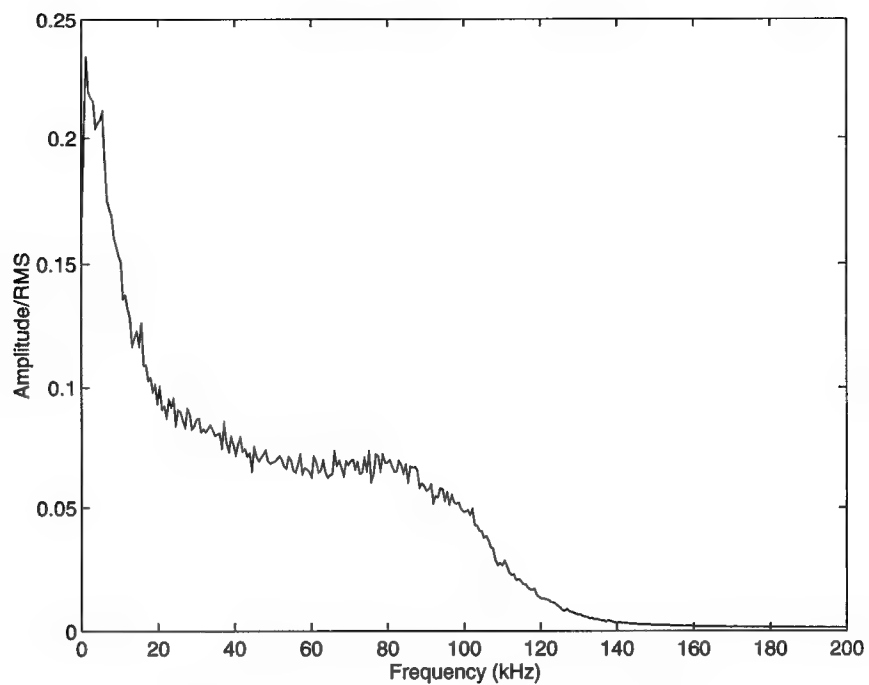


Figure A.5 : FFT for Station 31; $Re_\infty=4,265,000/m$

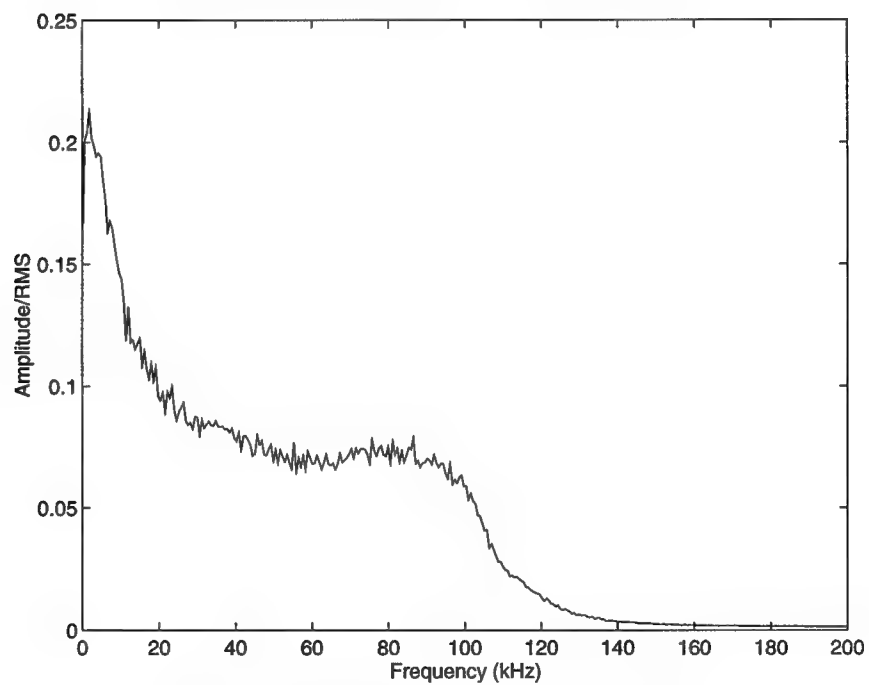


Figure A.6 : FFT for Station 32; $Re_\infty=4,265,000/m$

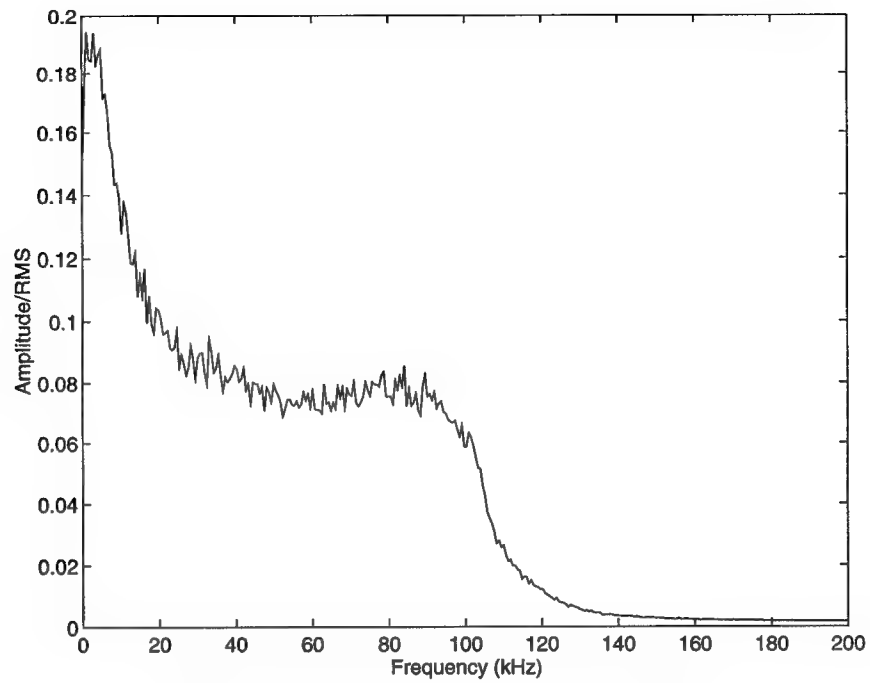


Figure A.7 : FFT for Station 33; $Re_\infty=4,265,000/m$

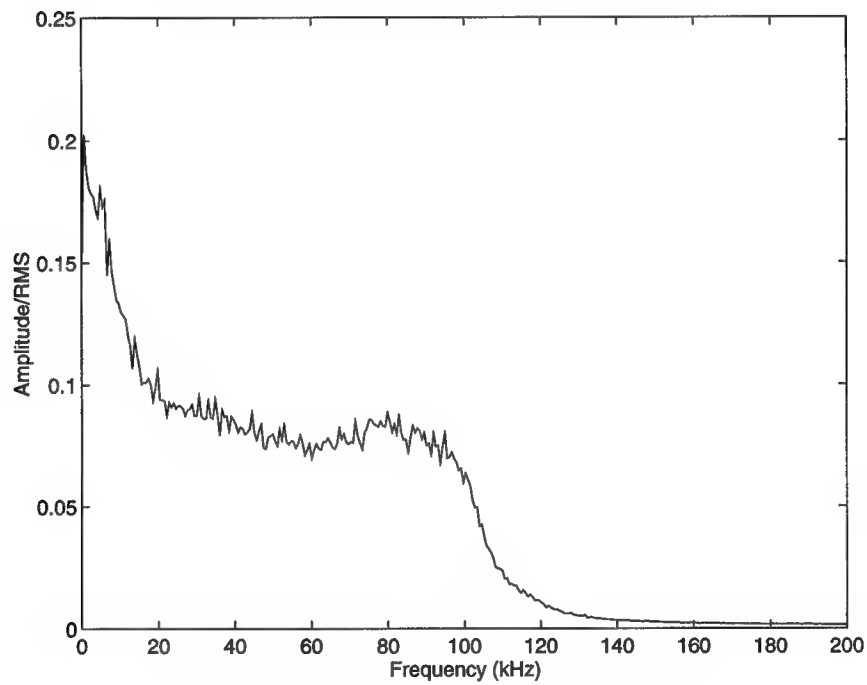


Figure A.8 : FFT for Station 34; $Re_\infty=4,265,000/m$

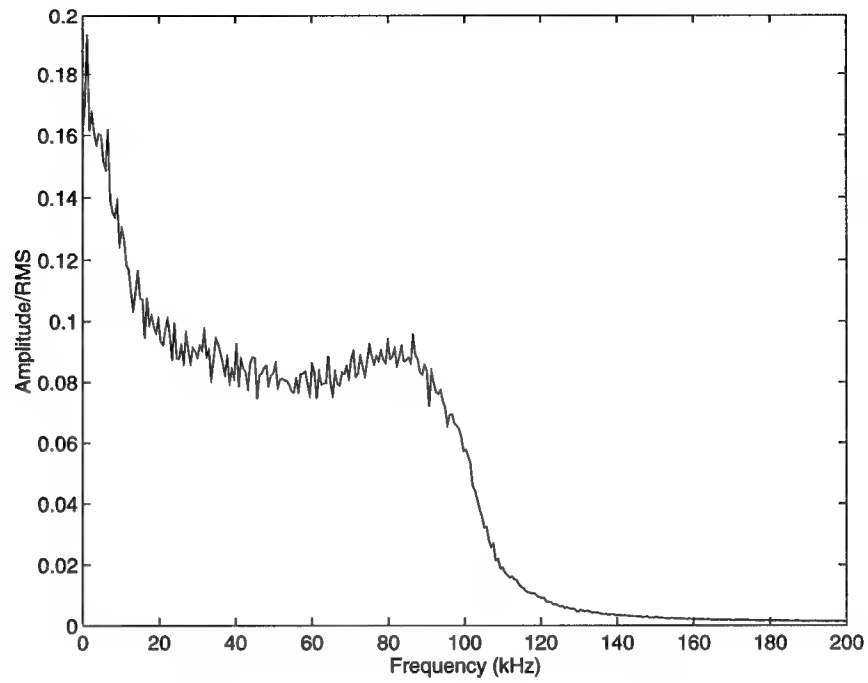


Figure A.9 : FFT for Station 35; $Re_\infty=4,265,000/m$

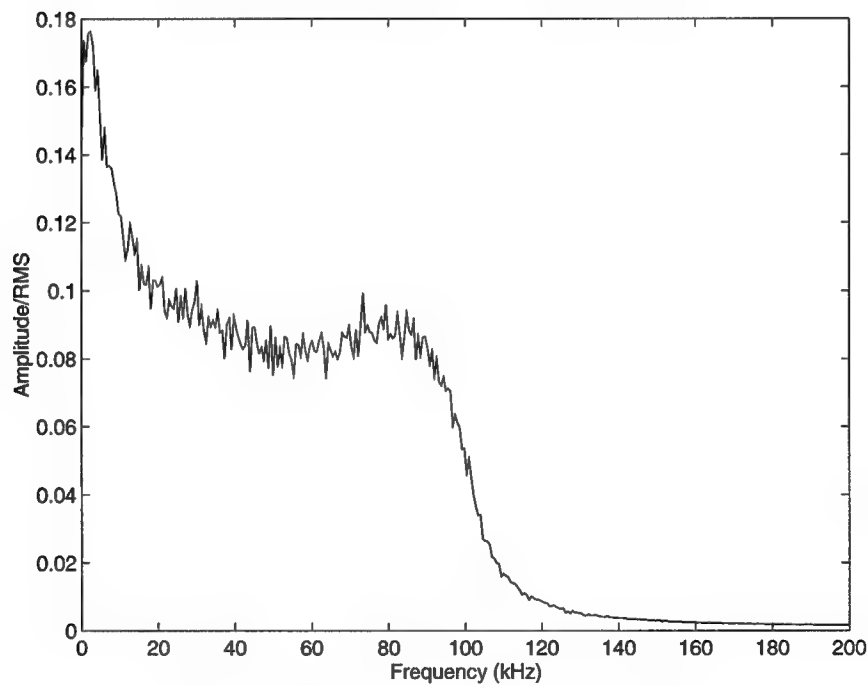


Figure A.10 : FFT for Station 36; $Re_\infty=4,265,000/m$

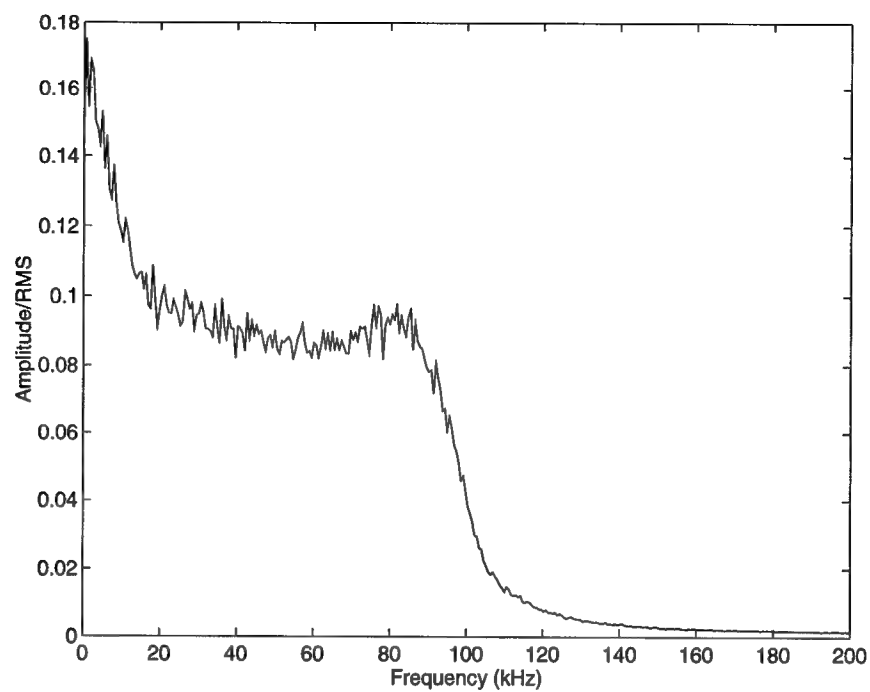


Figure A.11 : FFT for Station 37; $Re_\infty=4,265,000/m$

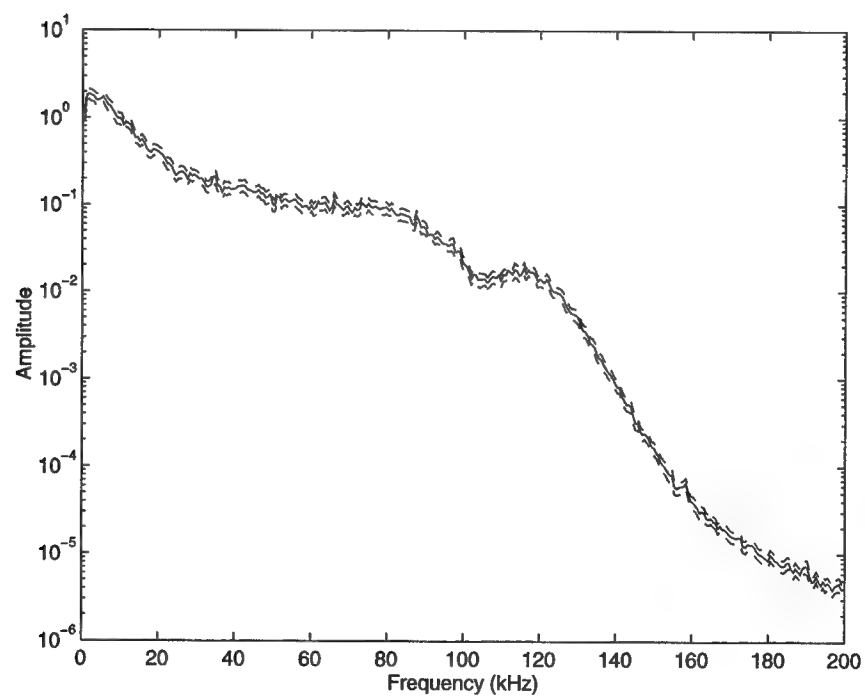


Figure A.12 : Power Spectrum for Station 27; $Re_\infty=4,265,000/m$

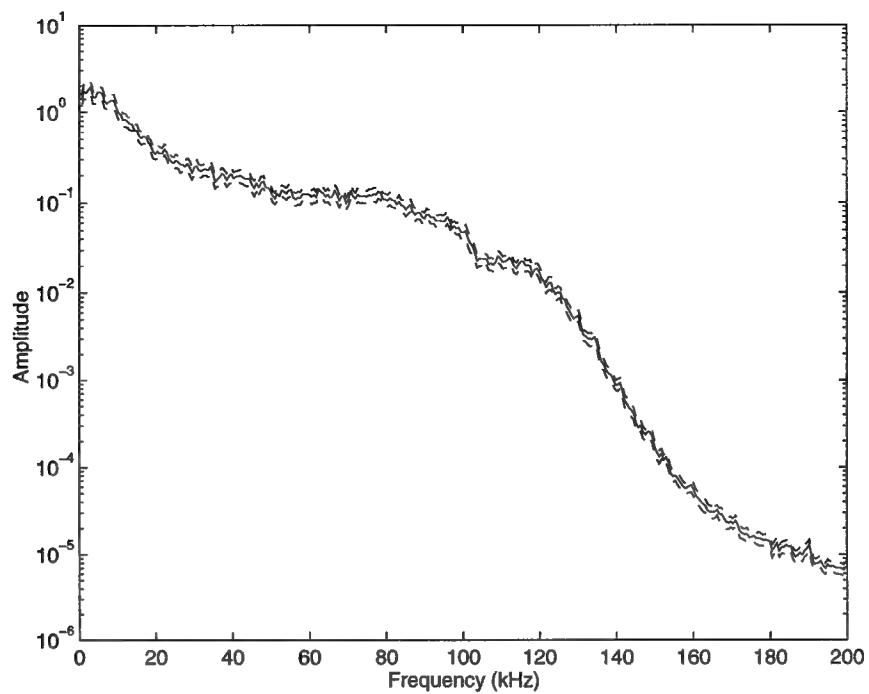


Figure A.13 : Power Spectrum for Station 28; $Re_\infty=4,265,000/m$

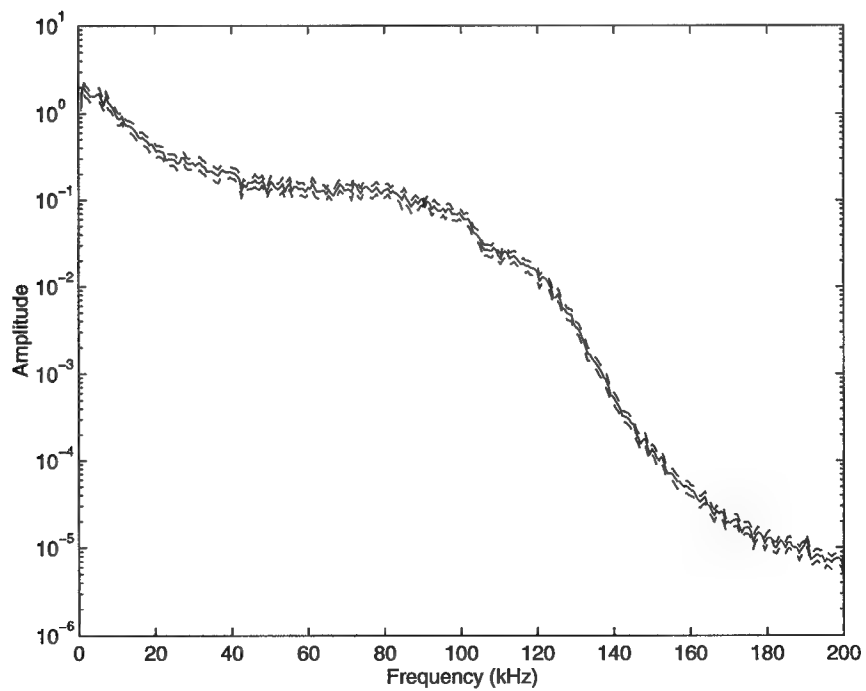


Figure A.14 : Power Spectrum for Station 29; $Re_\infty=4,265,000/m$

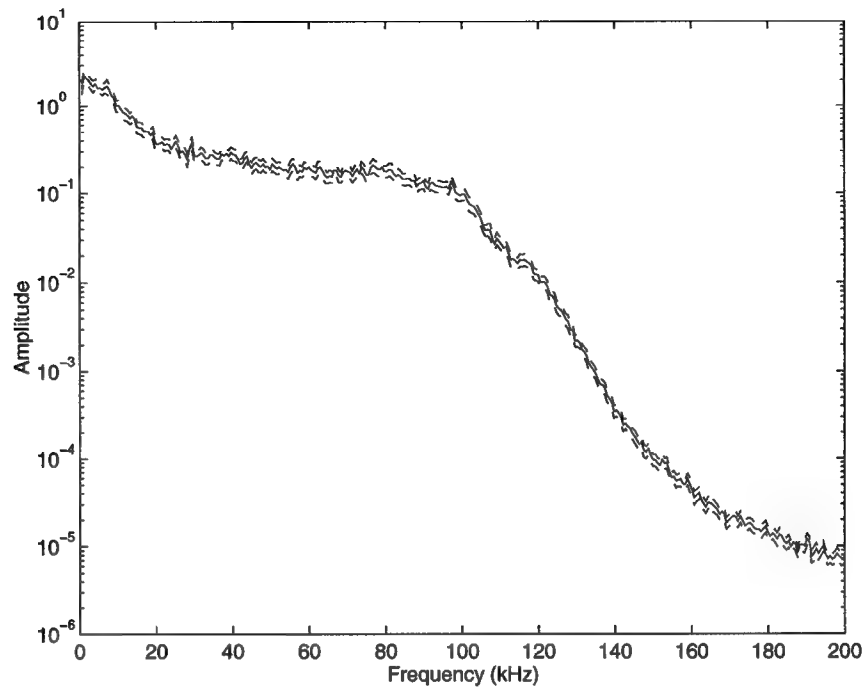


Figure A.15 : Power Spectrum for Station 30; $Re_\infty=4,265,000/m$

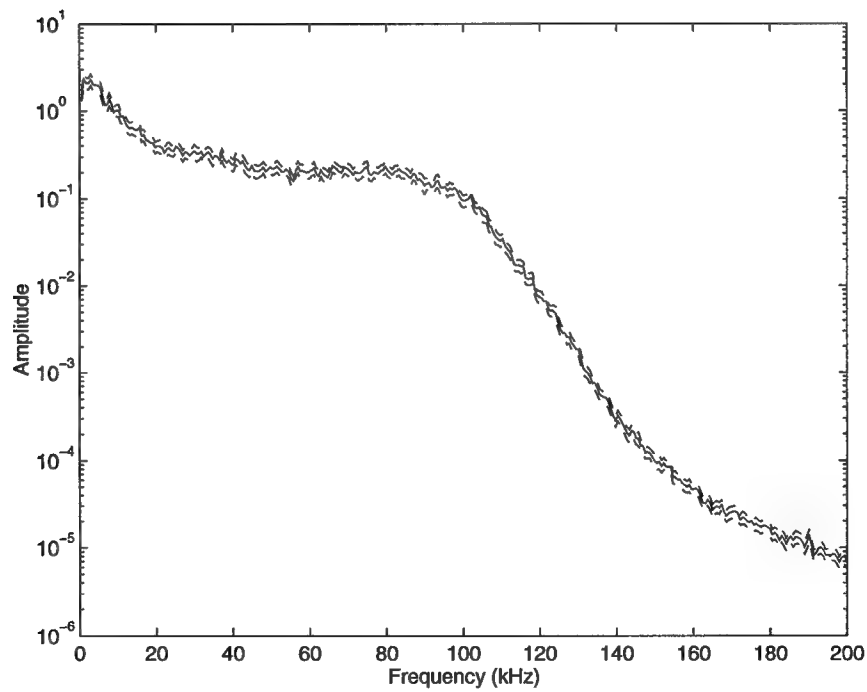


Figure A.16 : Power Spectrum for Station 31; $Re_\infty=4,265,000/m$

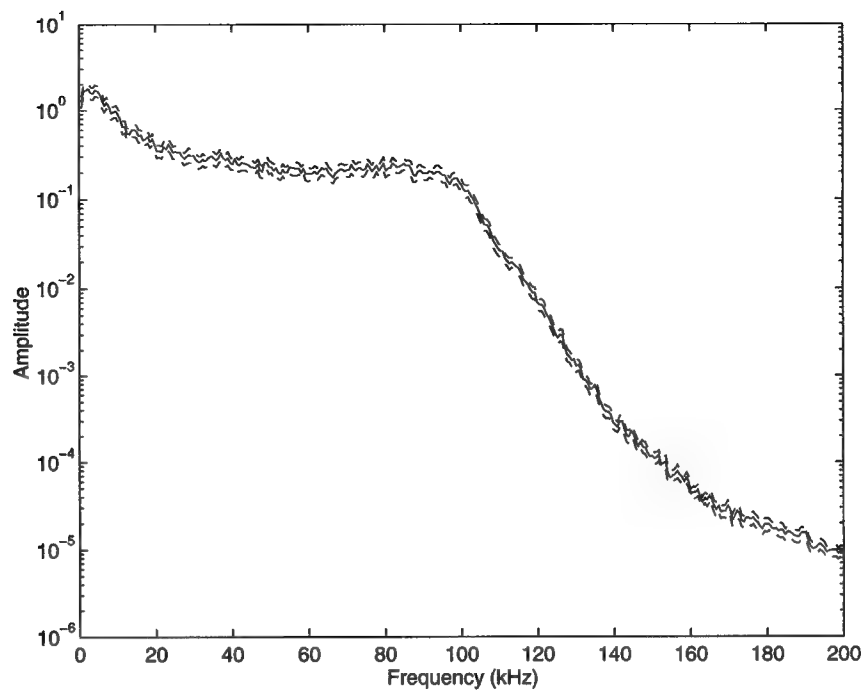


Figure A.17 : Power Spectrum for Station 32; $Re_\infty=4,265,000/m$

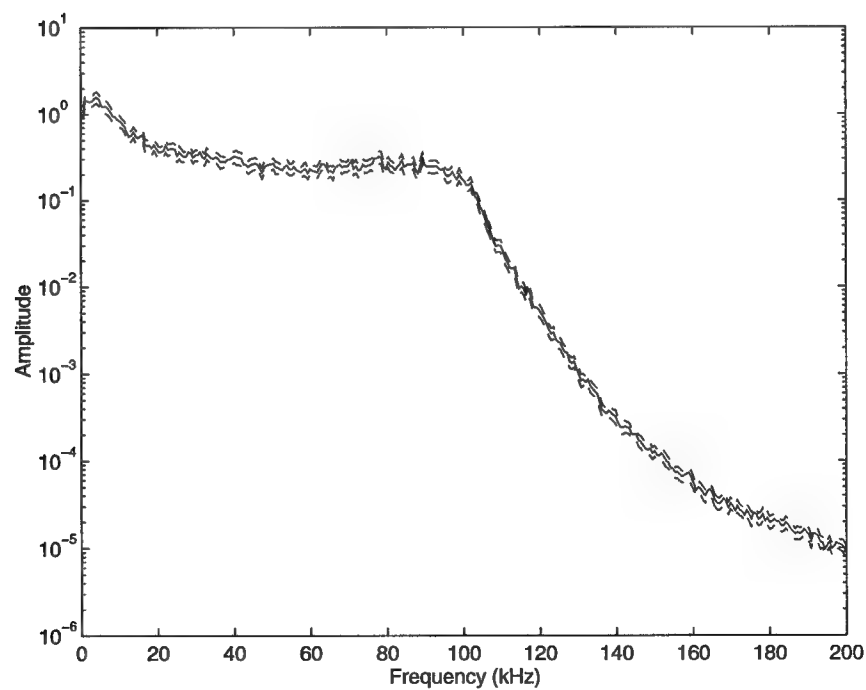


Figure A.18 : Power Spectrum for Station 33; $Re_\infty=4,265,000/m$

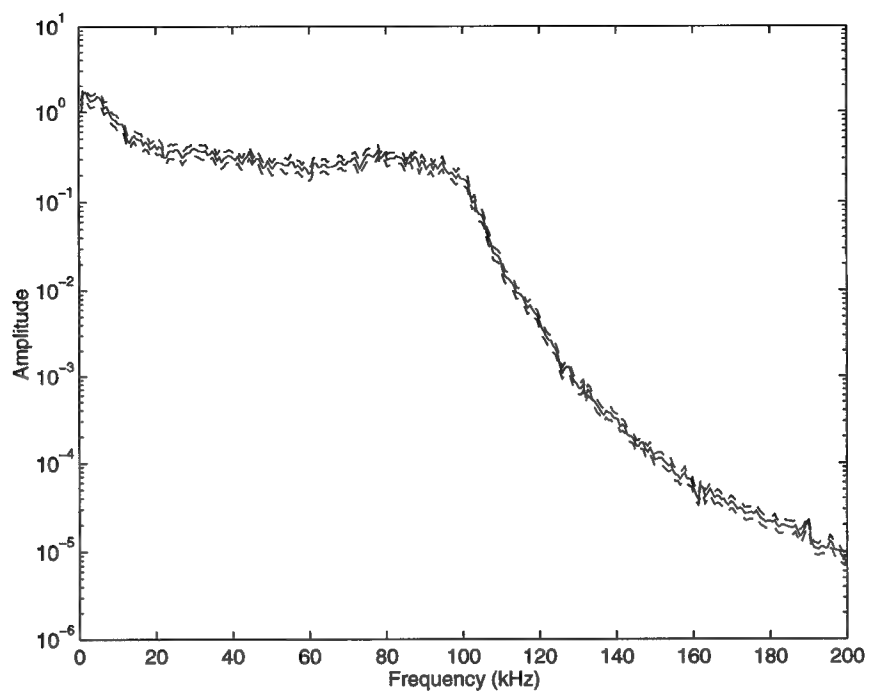


Figure A.19 : Power Spectrum for Station 34; $Re_\infty=4,265,000/m$

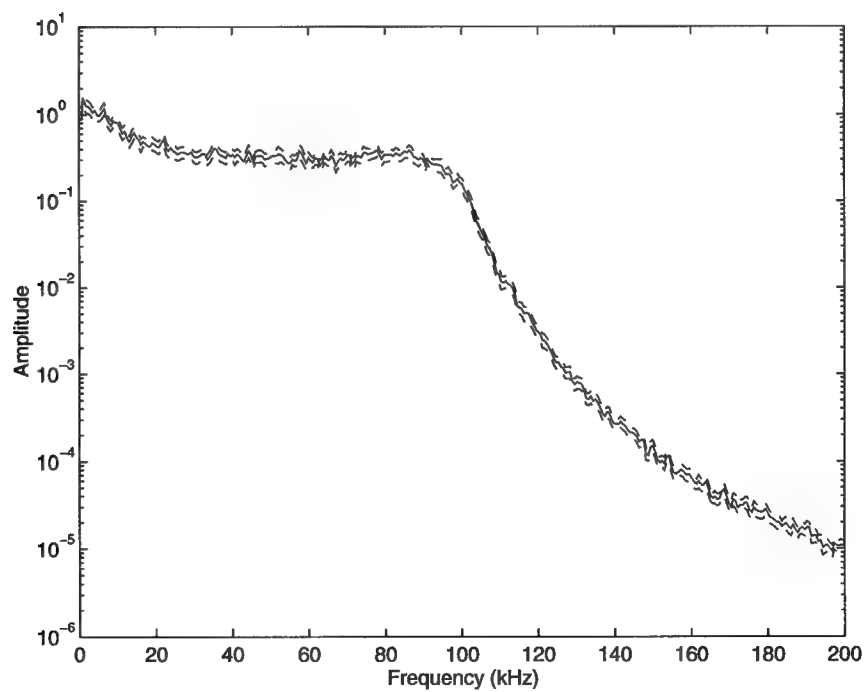


Figure A.20 : Power Spectrum for Station 35; $Re_\infty=4,265,000/m$

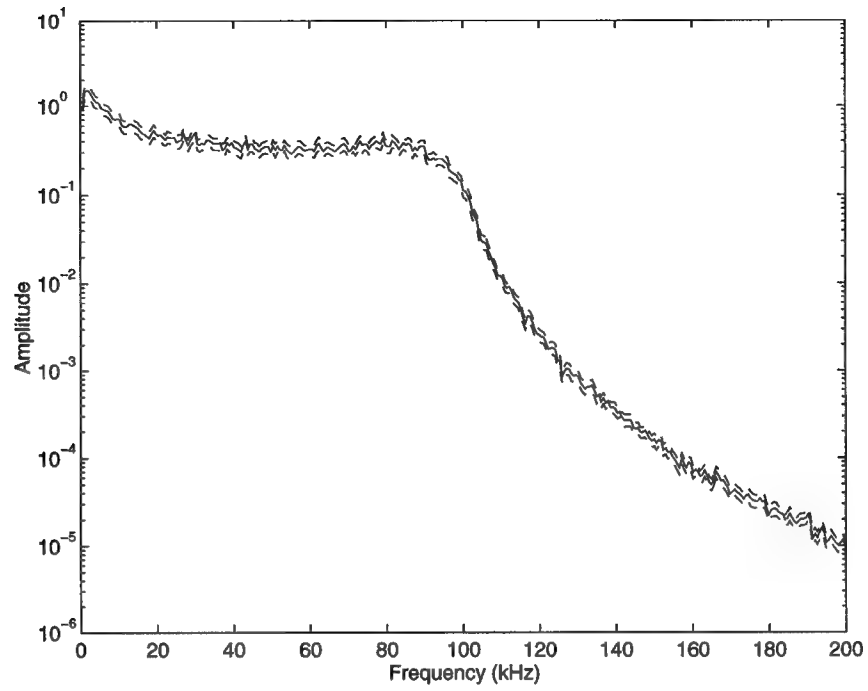


Figure A.21 : Power Spectrum for Station 36; $Re_\infty=4,265,000/m$

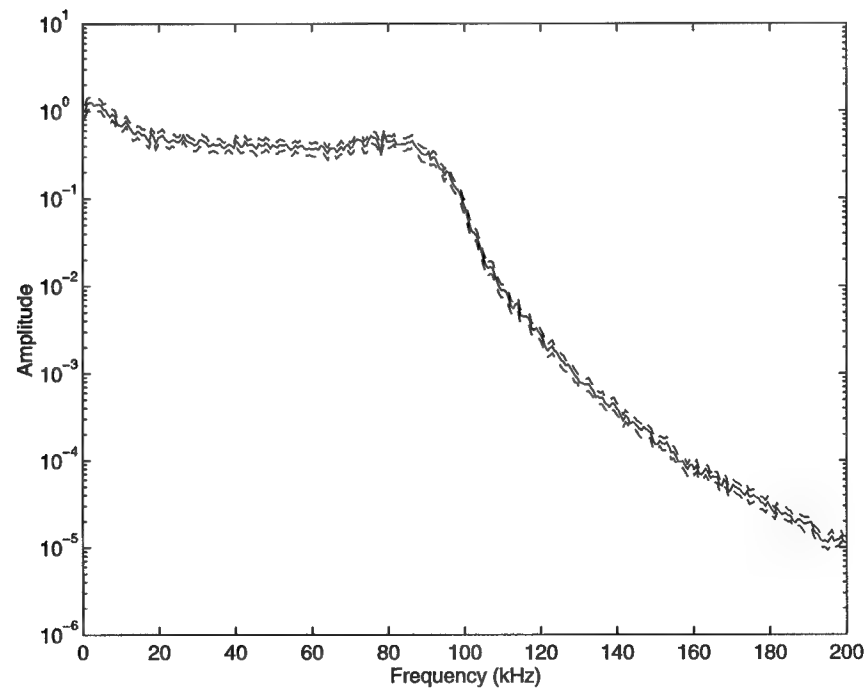


Figure A.22 : Power Spectrum for Station 37; $Re_\infty=4,265,000/m$

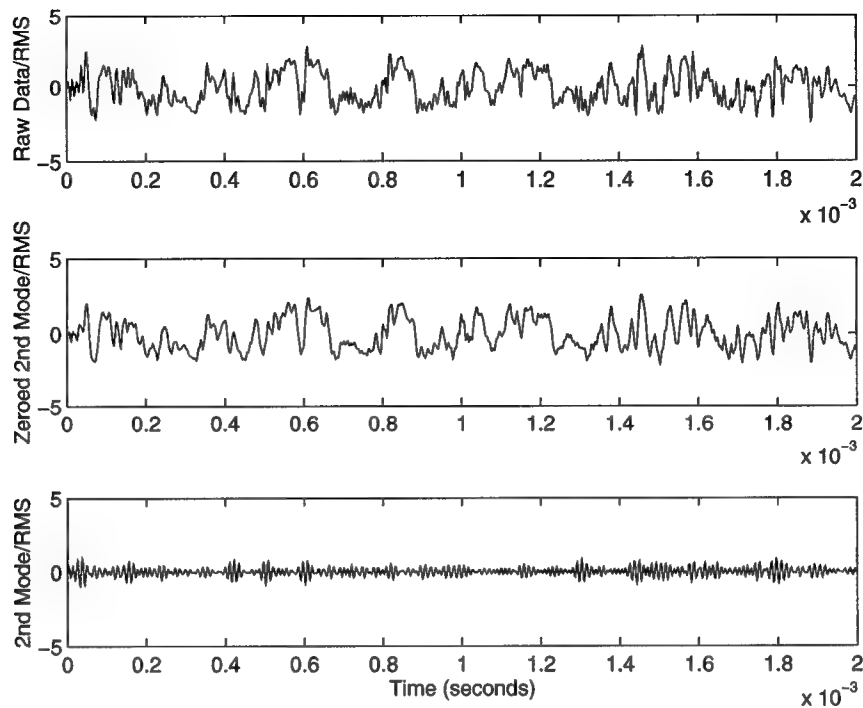


Figure A.23 : Data Signals for Station 27; $Re_{\infty}=4,265,000/m$

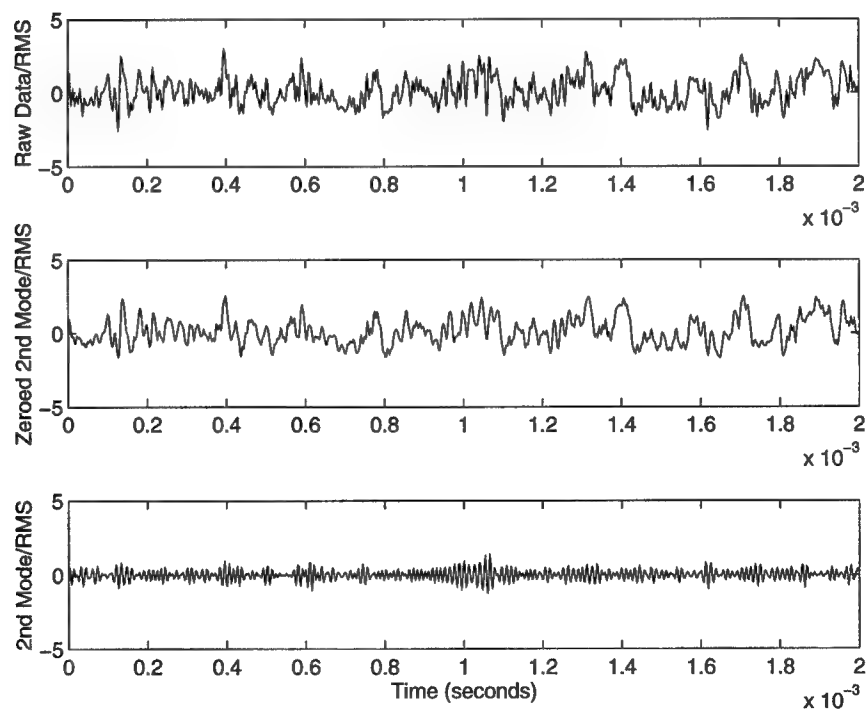


Figure A.24 : Data Signals for Station 28; $Re_{\infty}=4,265,000/m$

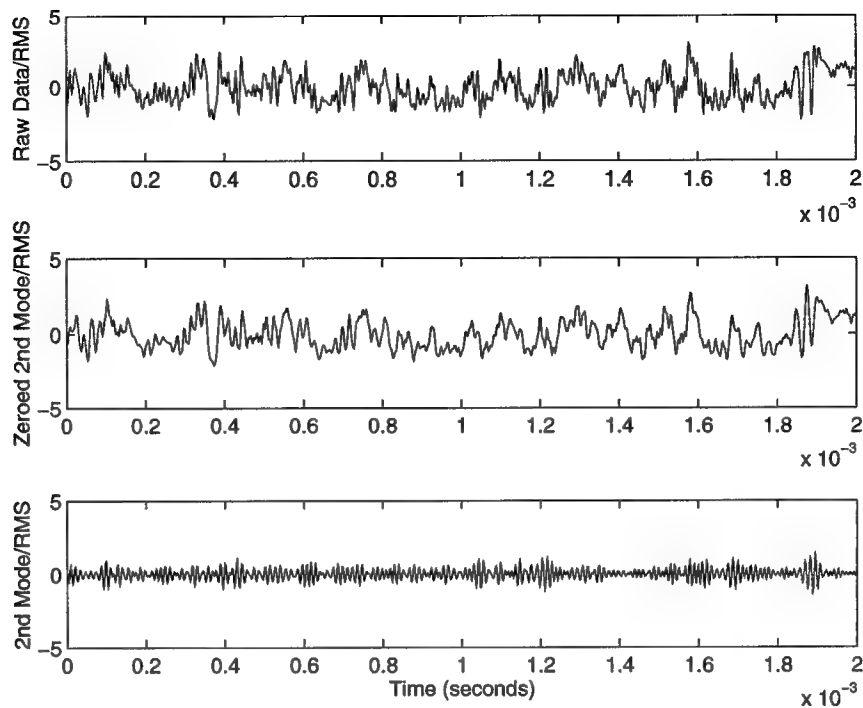


Figure A.25 : Data Signals for Station 29; $Re_{\infty}=4,265,000/m$

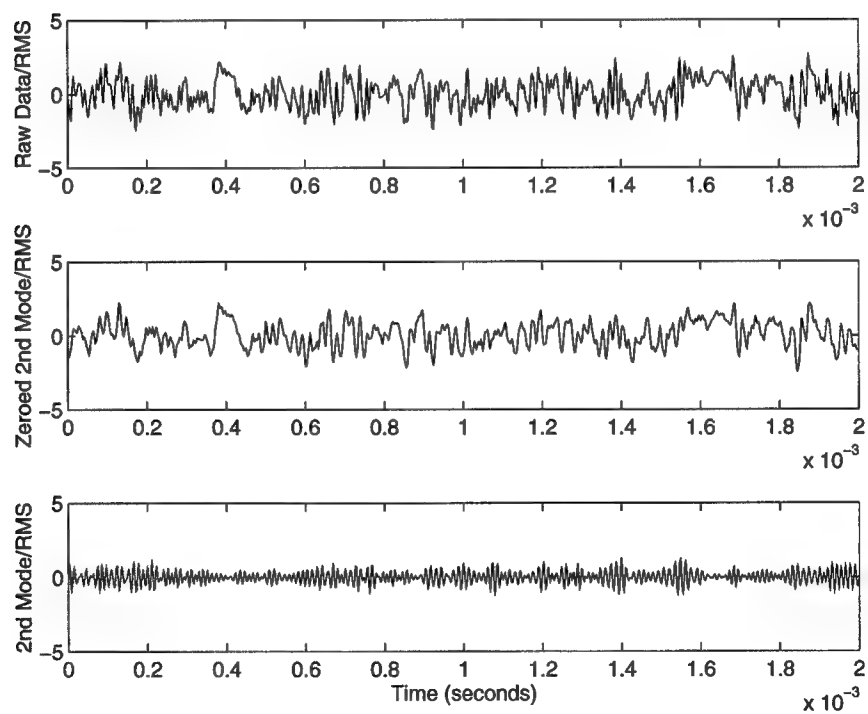


Figure A.26 : Data Signals for Station 30; $Re_{\infty}=4,265,000/m$

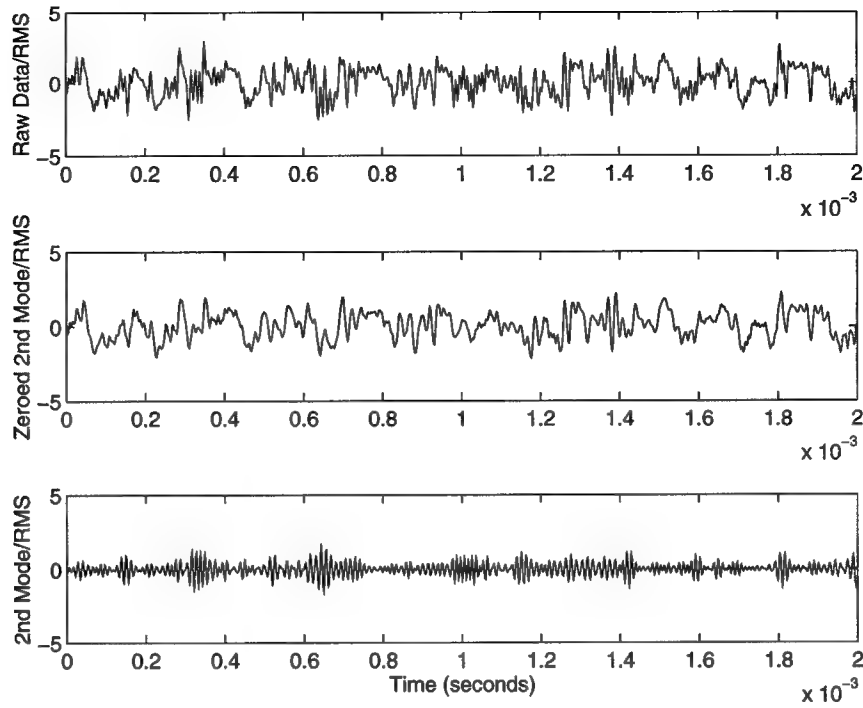


Figure A.27 : Data Signals for Station 31; $Re_{\infty}=4,265,000/m$

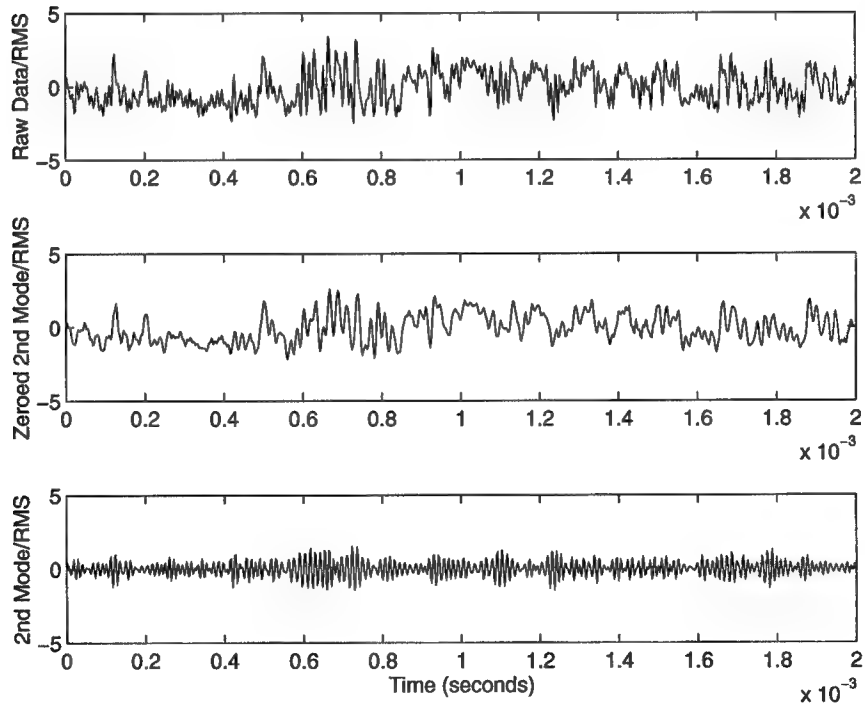


Figure A.28 : Data Signals for Station 32; $Re_{\infty}=4,265,000/m$

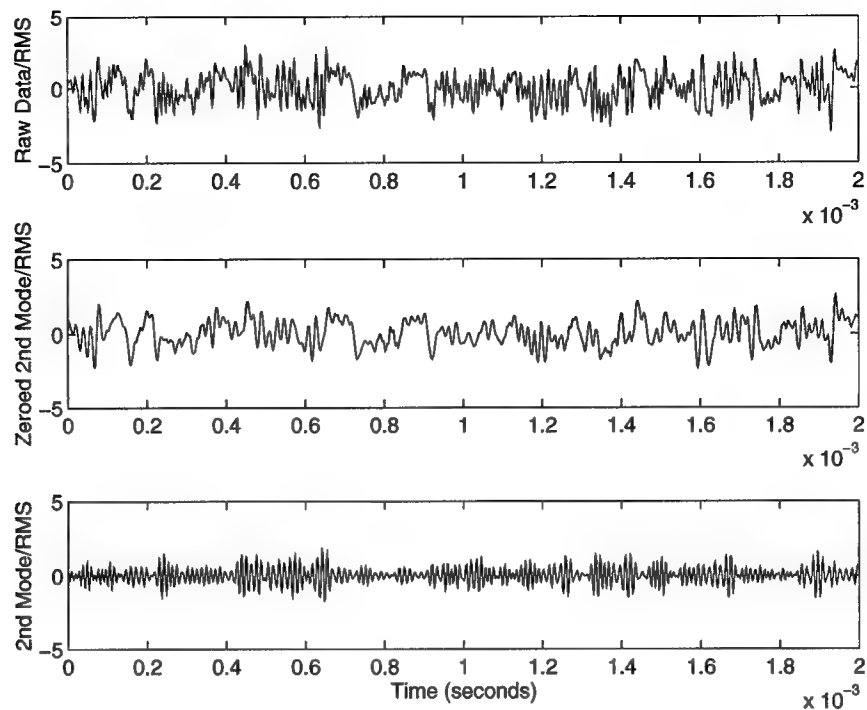


Figure A.29 : Data Signals for Station 33; $Re_{\infty}=4,265,000/m$

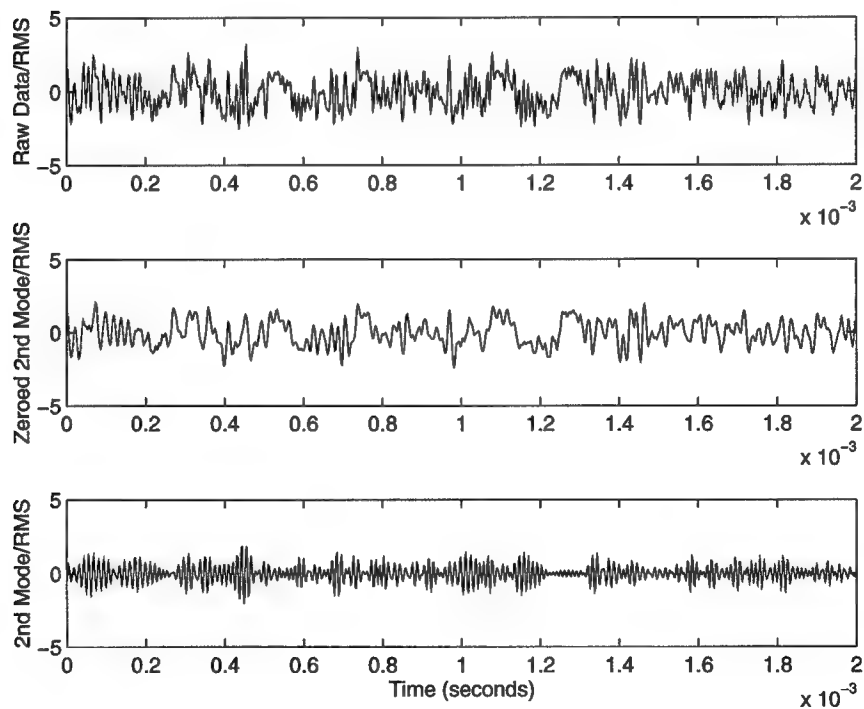


Figure A.30 : Data Signals for Station 34; $Re_{\infty}=4,265,000/m$

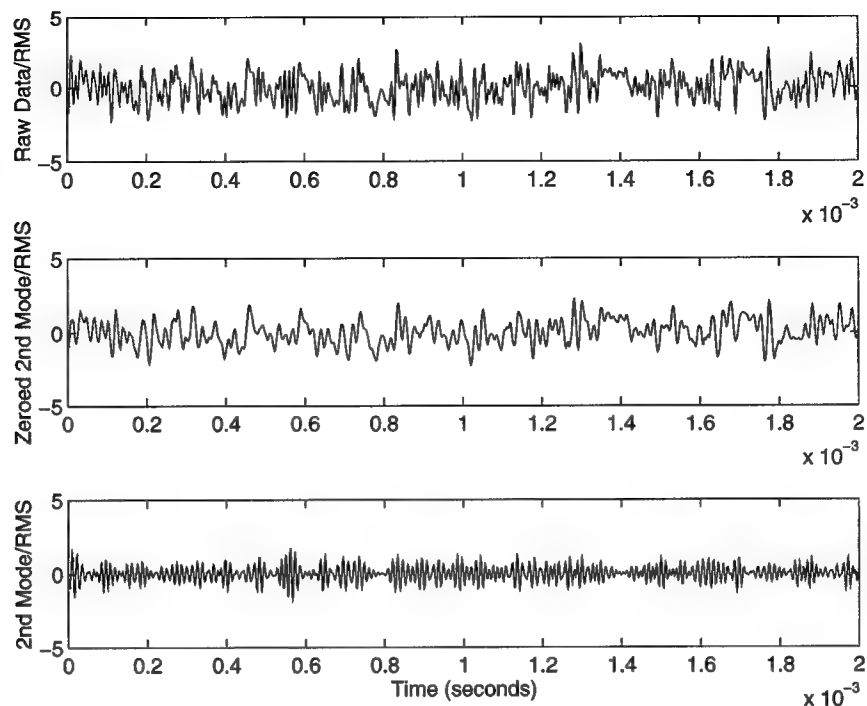


Figure A.31 : Data Signals for Station 35; $Re_{\infty}=4,265,000/m$

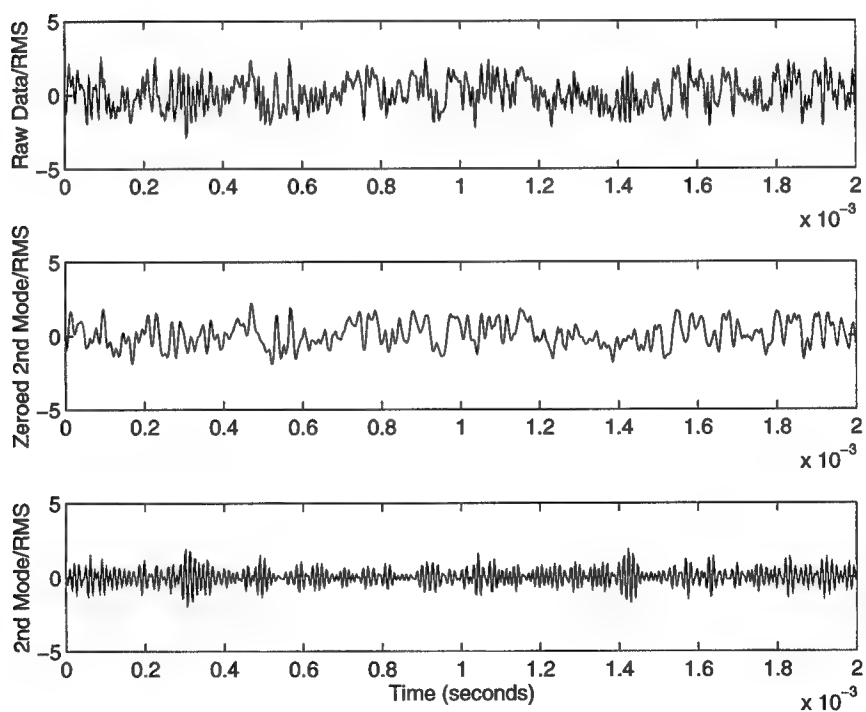


Figure A.32 : Data Signals for Station 36; $Re_{\infty}=4,265,000/m$

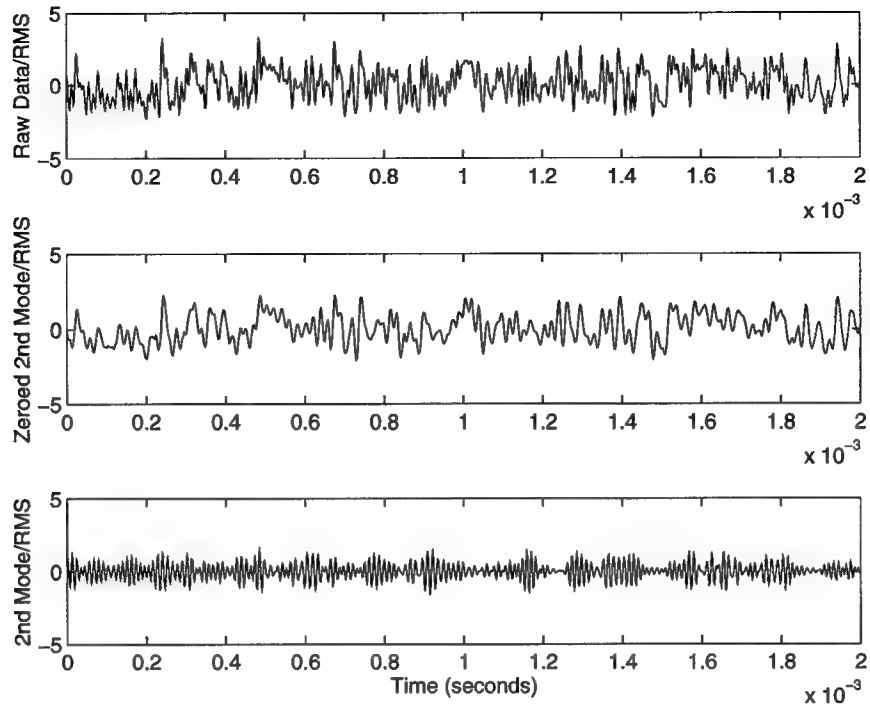


Figure A.33 : Data Signals for Station 37; $Re_{\infty}=4,265,000/m$

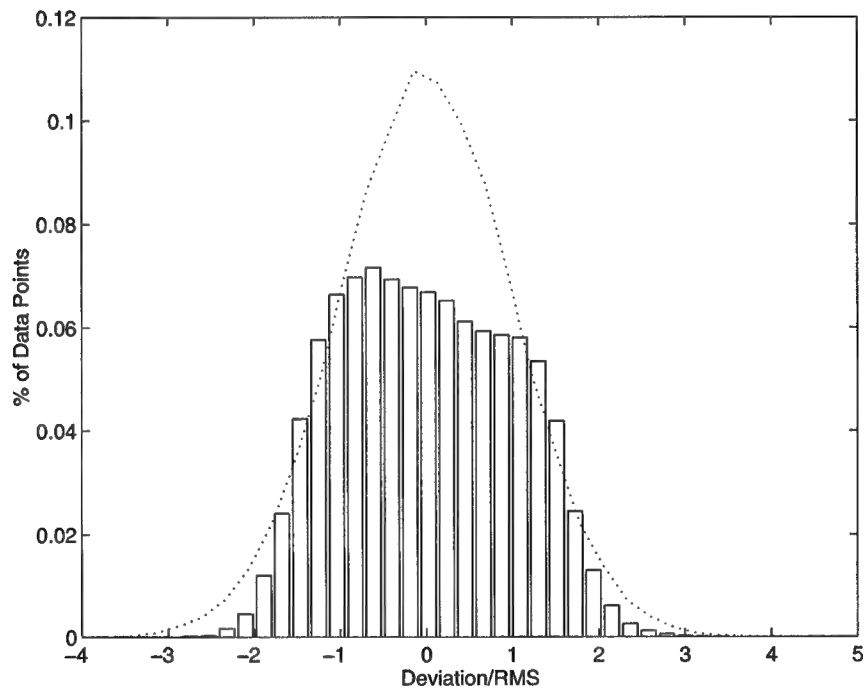


Figure 34 : Histogram for Station 27; $Re_{\infty}=4,265,000/m$

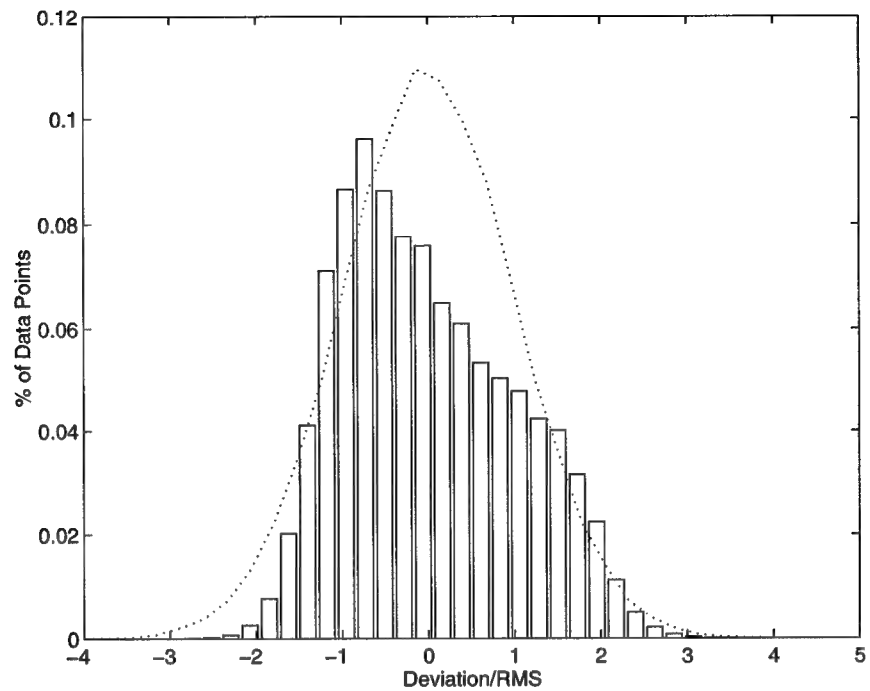


Figure A.35 : Histogram for Station 28; $Re_{\infty}=4,265,000/m$

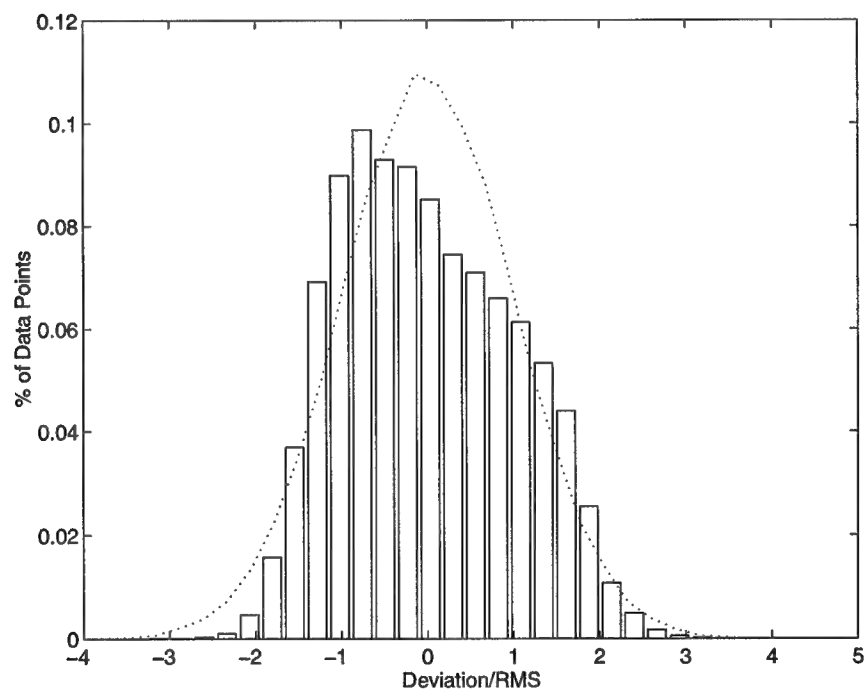


Figure A.36 : Histogram for Station 29; $Re_{\infty}=4,265,000/m$

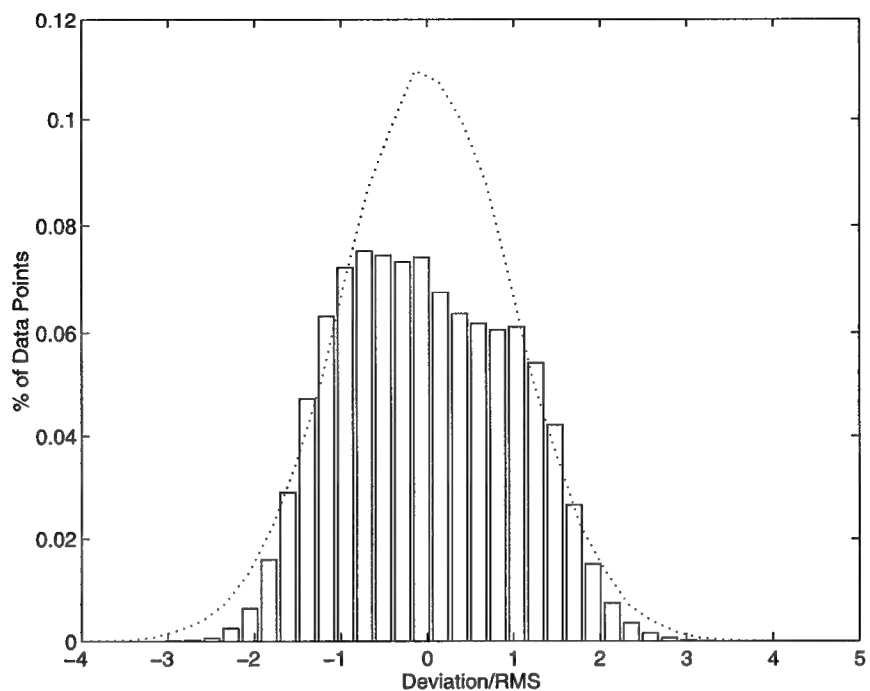


Figure A.37 : Histogram for Station 30; $Re_{\infty}=4,265,000/m$

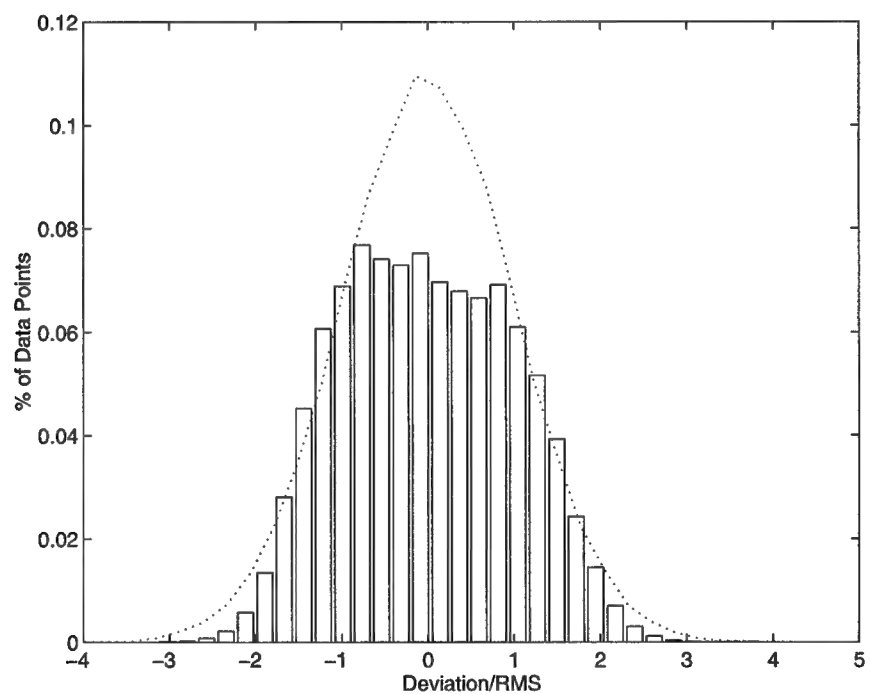


Figure A.38 : Histogram for Station 31; $Re_{\infty}=4,265,000/m$

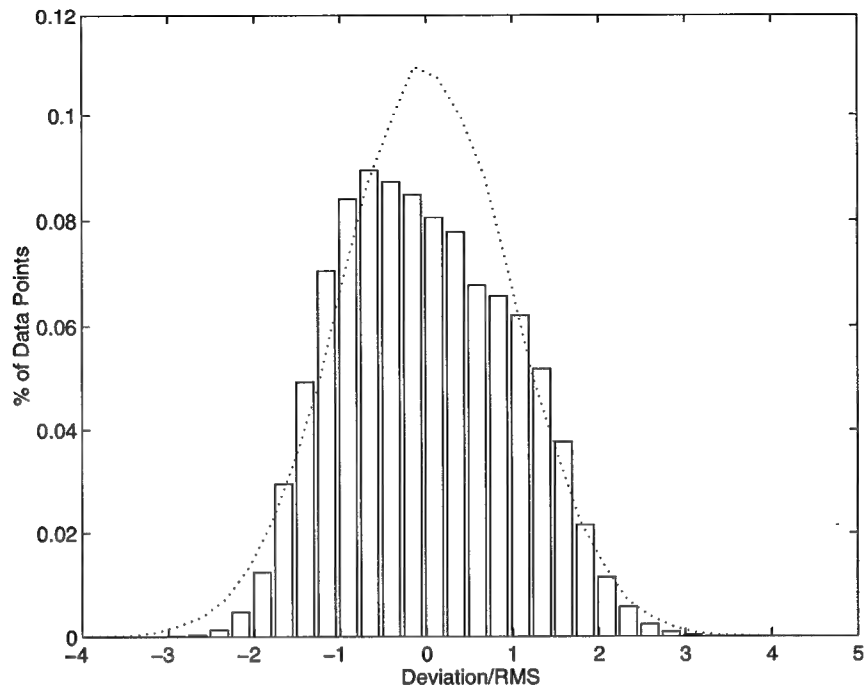


Figure A.39 : Histogram for Station 32; $Re_{\infty}=4,265,000/m$

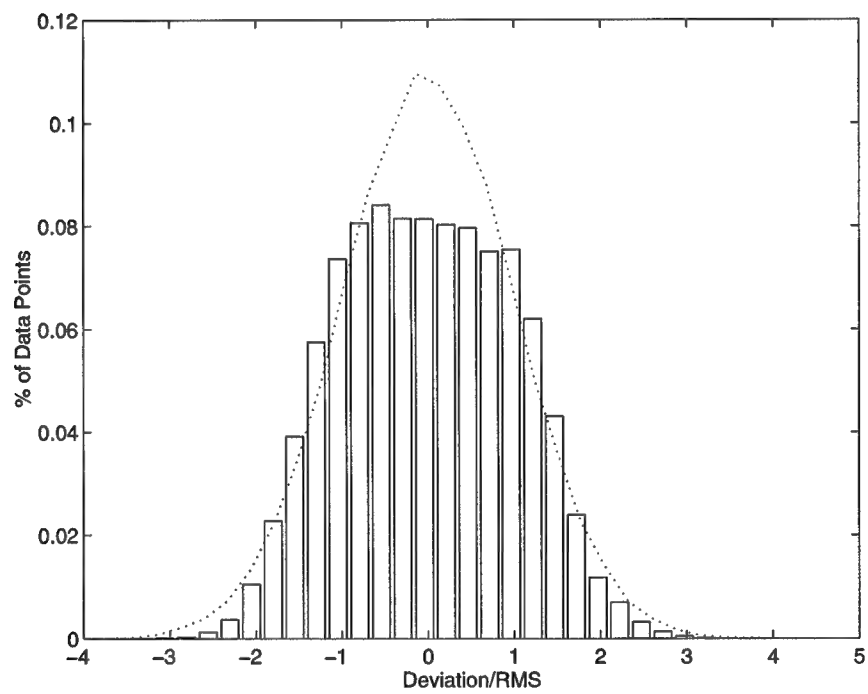


Figure A.40 : Histogram for Station 33; $Re_{\infty}=4,265,000/m$

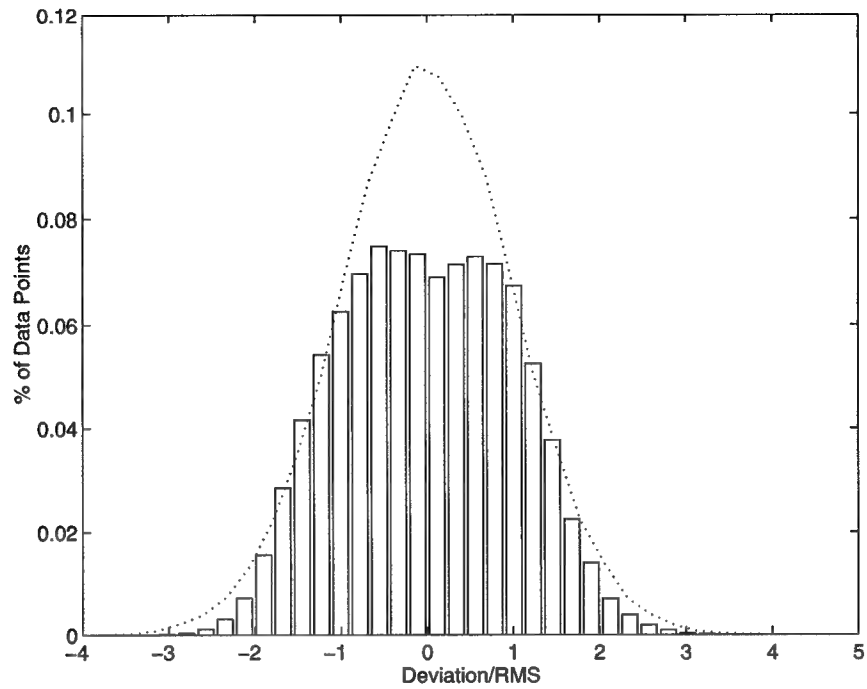


Figure A.41 : Histogram for Station 34; $Re_{\infty}=4,265,000/m$

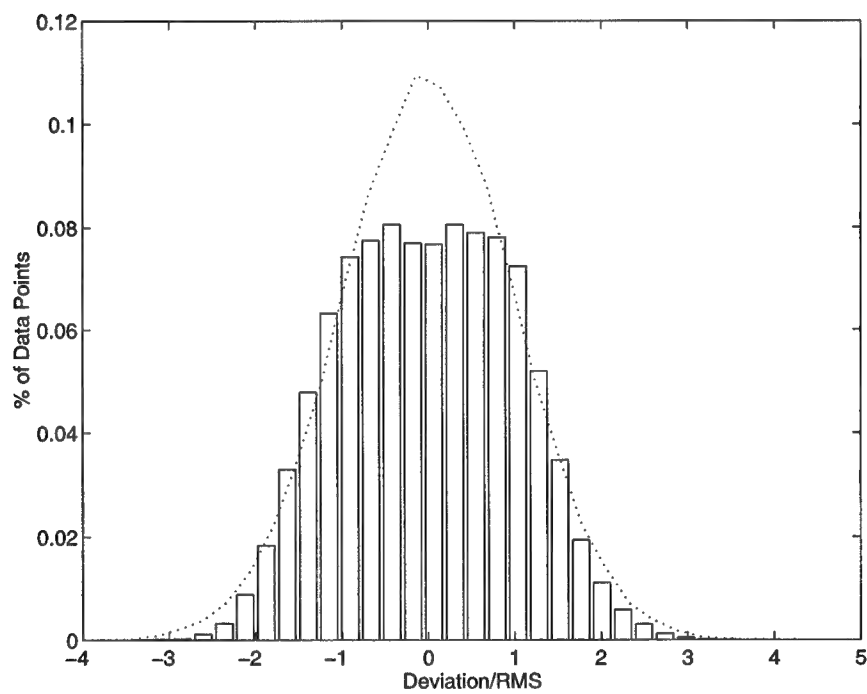


Figure A.42 : Histogram for Station 35; $Re_{\infty}=4,265,000/m$

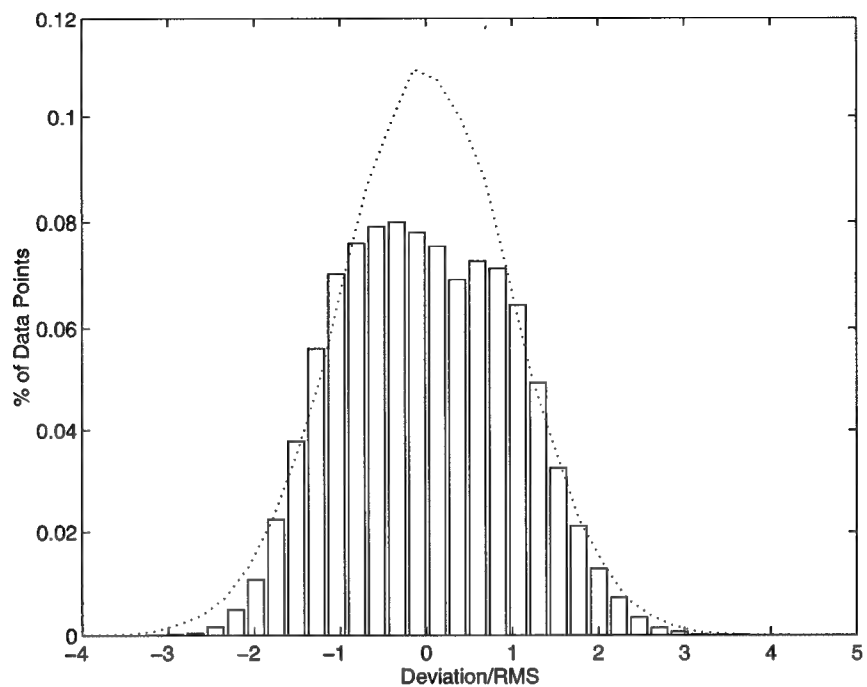


Figure A.43 : Histogram for Station 36; $Re_{\infty}=4,265,000/m$

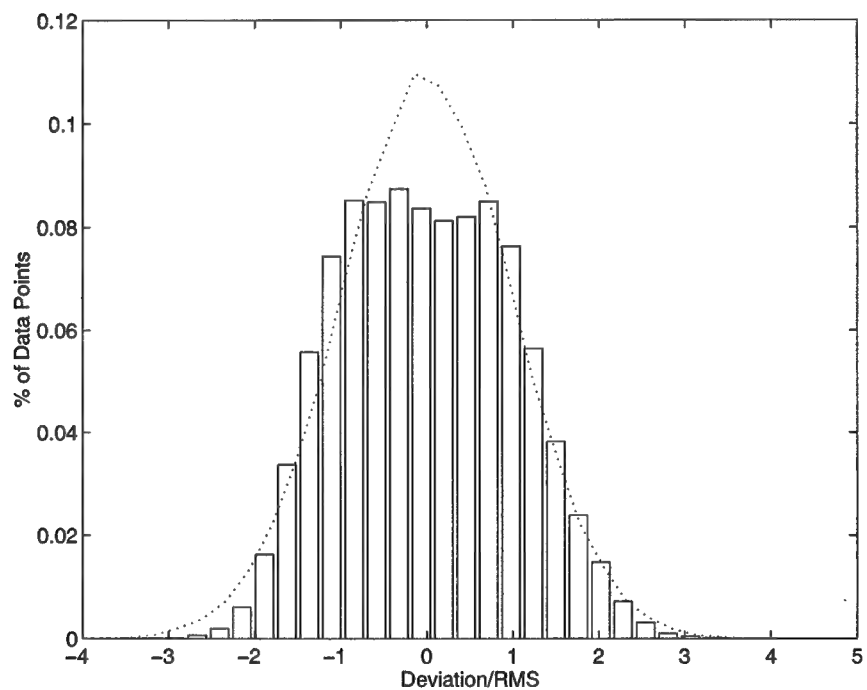


Figure A.44 : Histogram for Station 37; $Re_{\infty}=4,265,000/m$

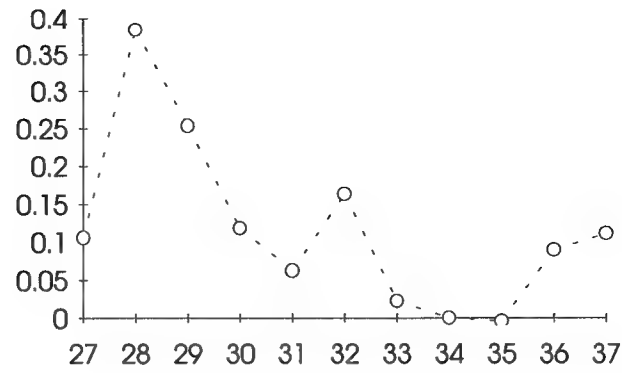


Figure A.45: Skewness Factor for $Re_{\infty}=4,265,000/m$

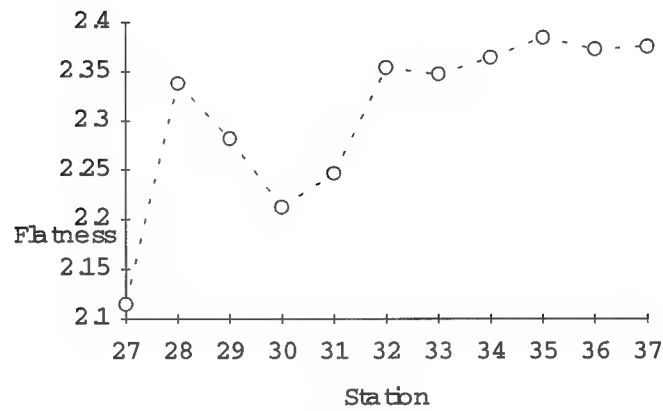


Figure A.46: Flatness Factor for $Re_{\infty}=4,265,000/m$

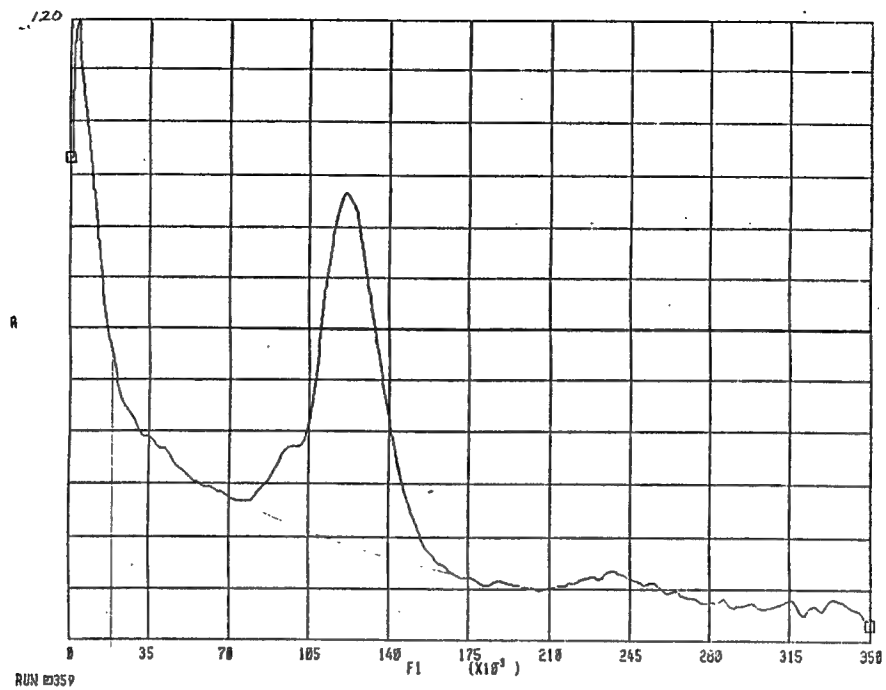


Figure A.47 : FFT (Alt. Source) for Station 27; $Re_\infty=4,265,000/m$

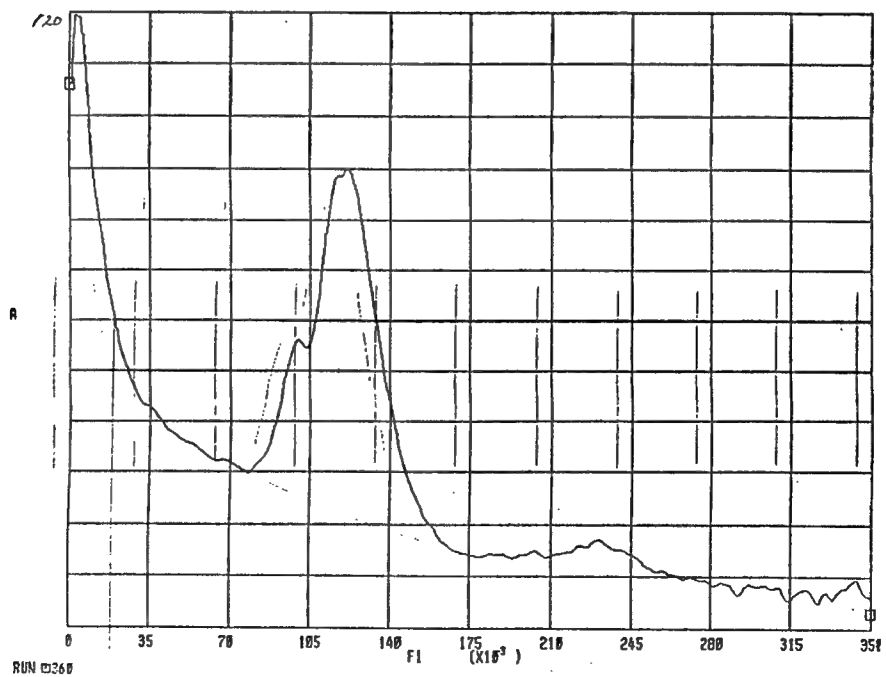


Figure A.48 : FFT (Alt. Source) for Station 28; $Re_\infty=4,265,000/m$

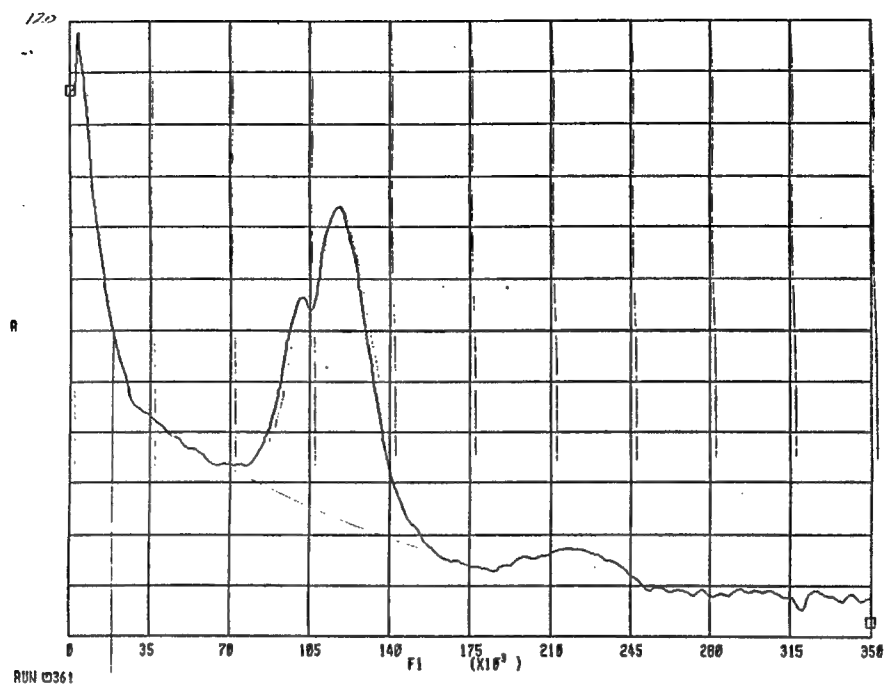


Figure A.49 : FFT (Alt. Source) for Station 29; $Re_\infty=4,265,000/m$

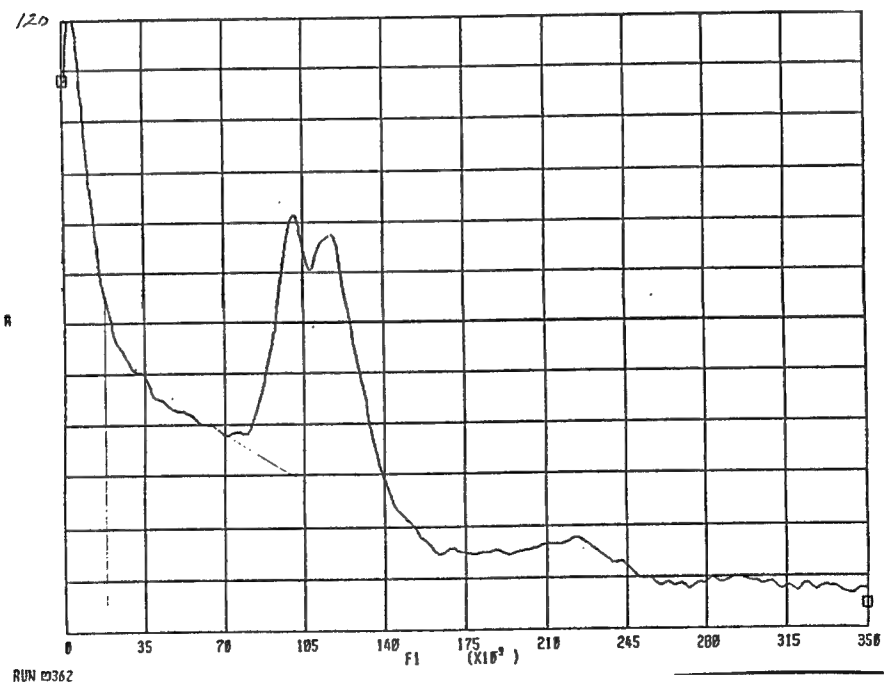


Figure A.50 : FFT (Alt. Source) for Station 30; $Re_\infty=4,265,000/m$

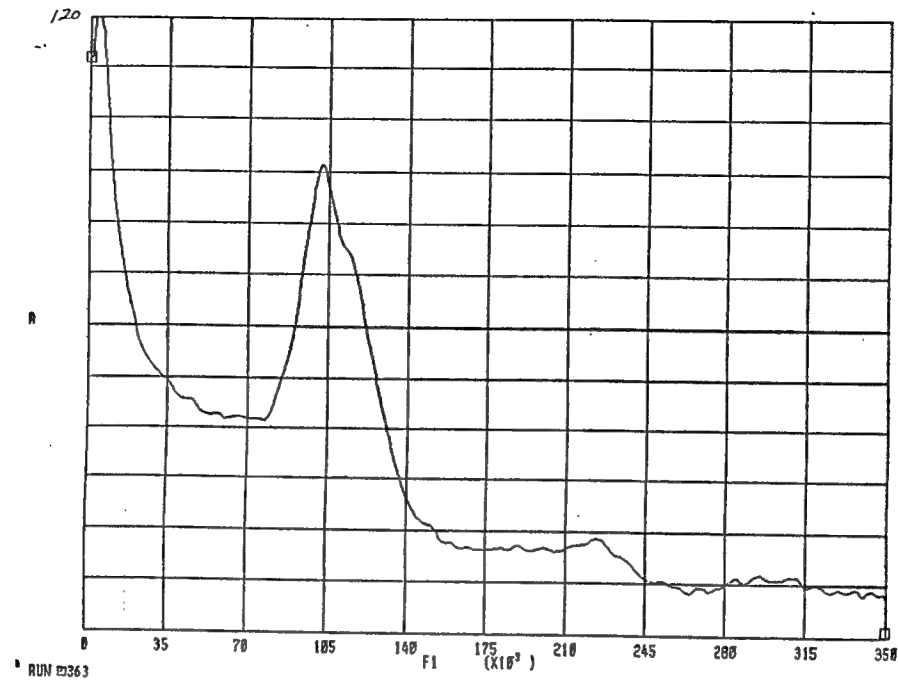


Figure A.51 : FFT (Alt. Source) for Station 31; $Re_{\infty}=4,265,000/m$

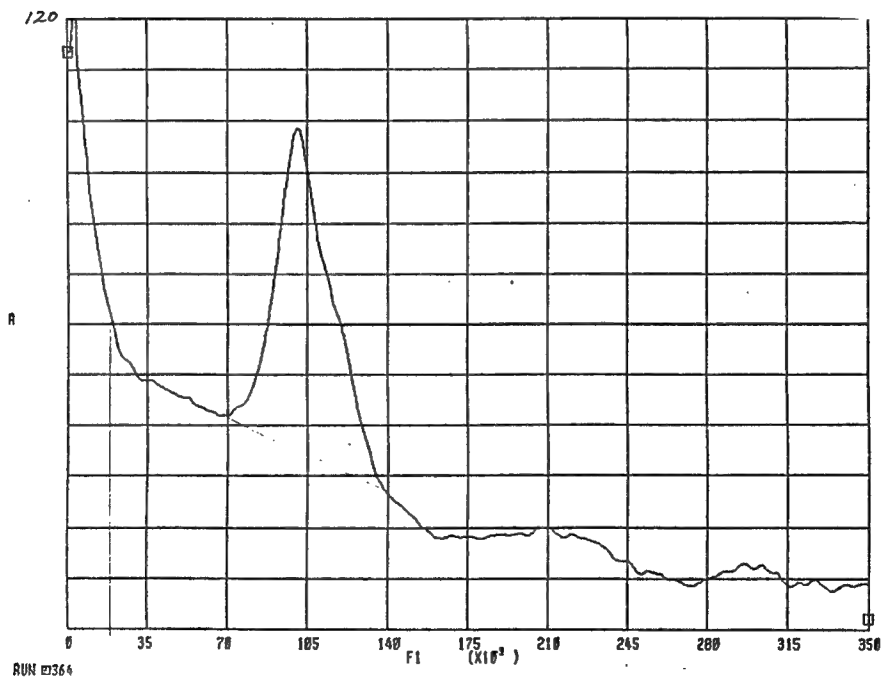


Figure A.52 : FFT (Alt. Source) for Station 32; $Re_{\infty}=4,265,000/m$

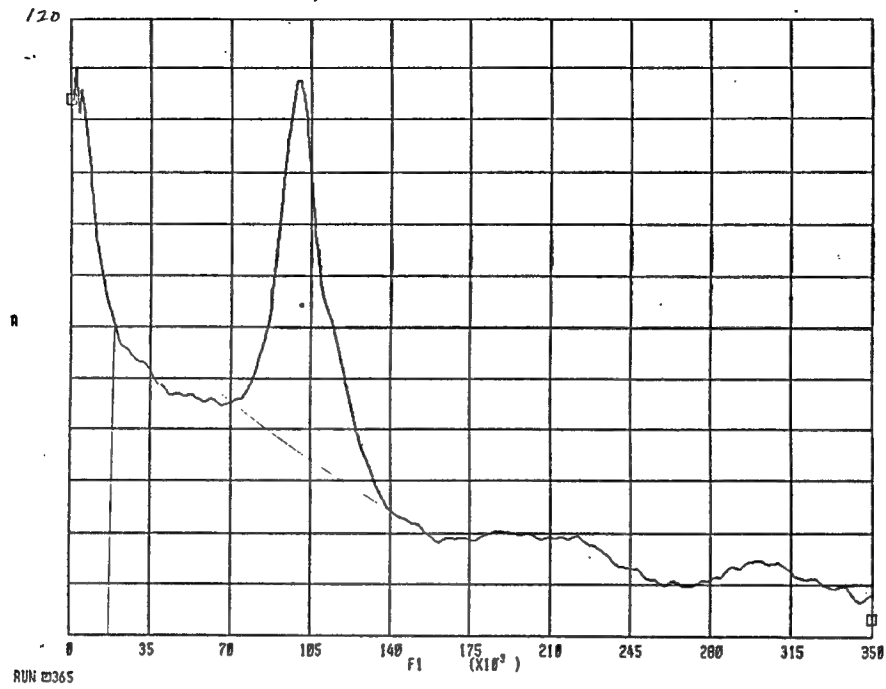


Figure A.53 : FFT (Alt. Source) for Station 33; $Re_\infty=4,265,000/m$

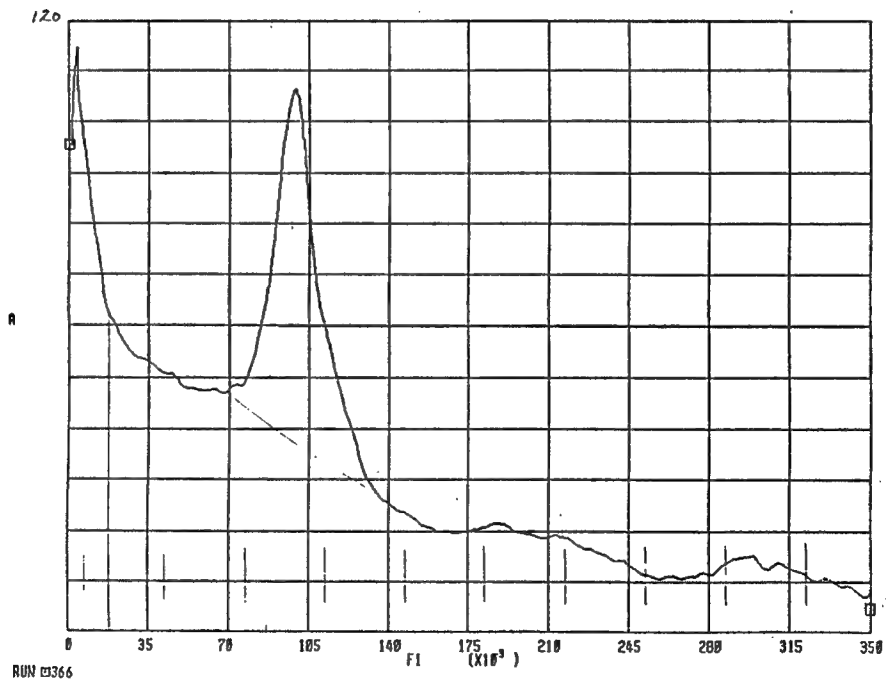


Figure A.54 : FFT (Alt. Source) for Station 34; $Re_\infty=4,265,000/m$

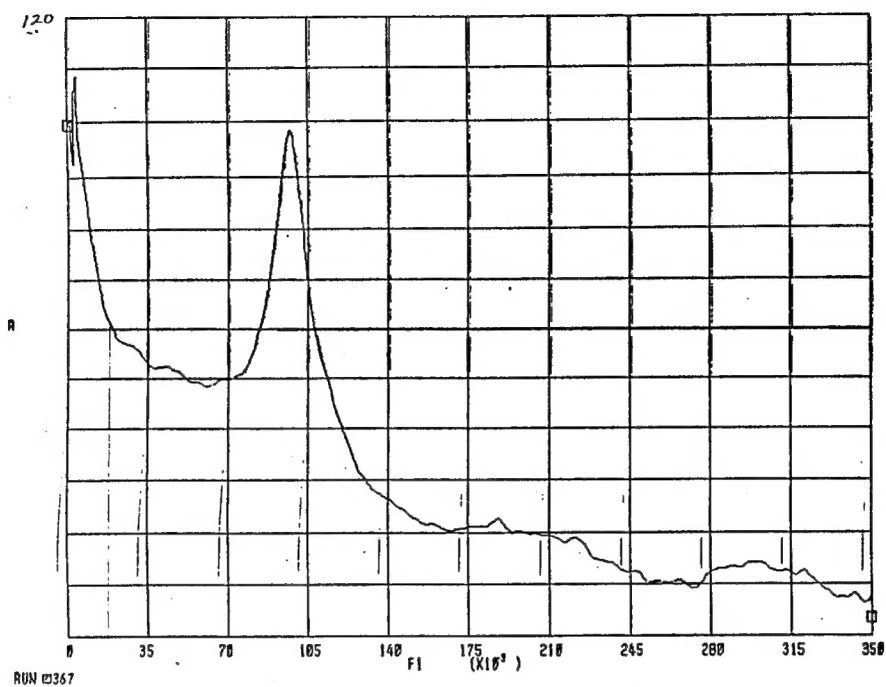


Figure A.55 : FFT (Alt. Source) for Station 35; $Re_\infty=4,265,000/m$

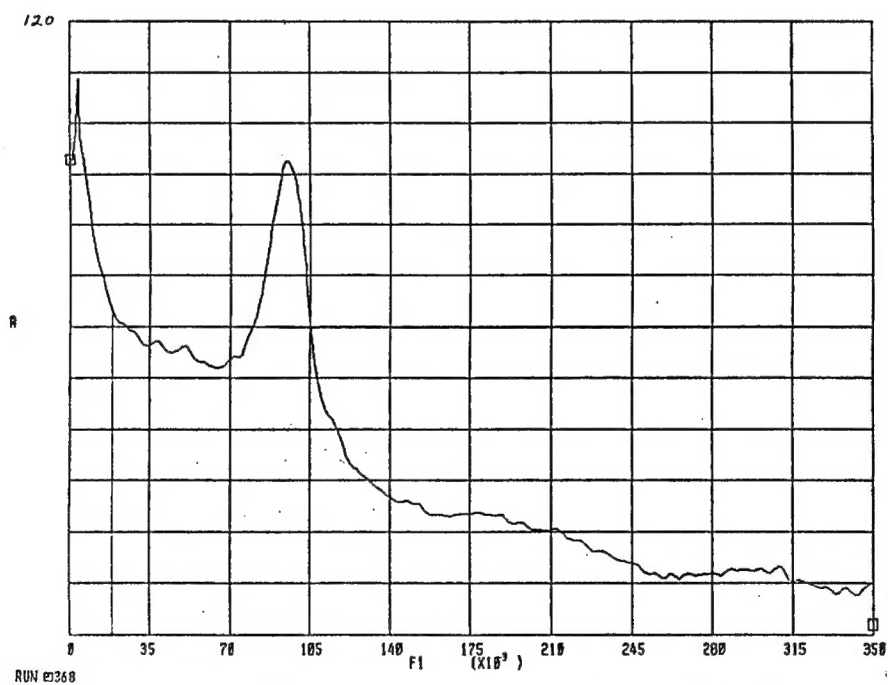


Figure A.56 : FFT (Alt. Source) for Station 36; $Re_\infty=4,265,000/m$

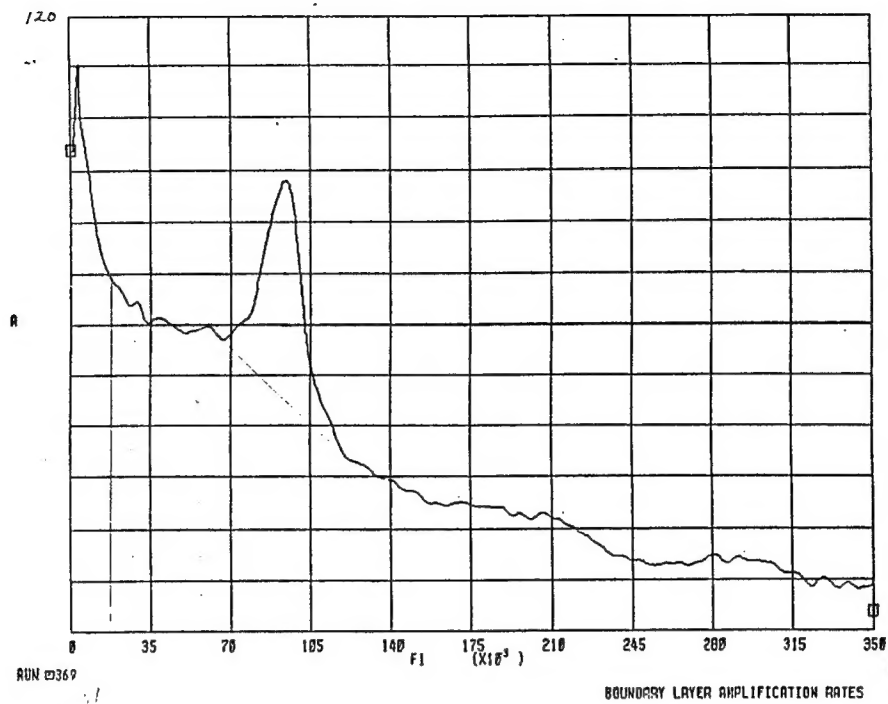


Figure A.57 : FFT (Alt. Source) for Station 37; $Re_{\infty}=4,265,000/m$;

REPORT DOCUMENTATION PAGE			Form Approved OMB No. 0704-0188	
<small>Public reporting burden for this collection of information is estimated to average 1 hour per response, including the time for reviewing instructions, searching existing data sources, gathering and maintaining the data needed, and completing and reviewing the collection of information. Send comments regarding this burden estimate or any other aspect of this collection of information, including suggestions for reducing this burden, to Washington Headquarters Services, Directorate for Information Operations and Reports, 1215 Jefferson Davis Highway, Suite 1204, Arlington, VA 22202-4302, and to the Office of Management and Budget, Paperwork Reduction Project (0704-0188), Washington, DC 20503.</small>				
1. AGENCY USE ONLY (Leave blank)	2. REPORT DATE December 1994	3. REPORT TYPE AND DATES COVERED Master's Thesis		
4. TITLE AND SUBTITLE ANALYSIS OF HYPERSONIC BOUNDARY LAYER SECOND MODE INSTABILITY OVER A SEVEN DEGREE CONE		5. FUNDING NUMBERS		
6. AUTHOR(S) Richard Dennery Capt, USAF				
7. PERFORMING ORGANIZATION NAME(S) AND ADDRESS(ES) Air Force Institute of Technology Wright-Patterson AFB OH 45433-6583		8. PERFORMING ORGANIZATION REPORT NUMBER AFIT/GA/ENY/94D-20		
9. SPONSORING / MONITORING AGENCY NAME(S) AND ADDRESS(ES) Roger Kimmell, Kevin Slima WL/FIVT WPAFB, OH 45433		10. SPONSORING / MONITORING AGENCY REPORT NUMBER		
11. SUPPLEMENTARY NOTES				
12a. DISTRIBUTION / AVAILABILITY STATEMENT Approved for public release; distribution unlimited			12b. DISTRIBUTION CODE	
13. ABSTRACT (Maximum 200 words) This paper presents the results of the analysis of Mach 8.0 flow over a seven degree half-angle cone. The purpose of this analysis was to develop techniques to examine boundary layer transition at hypersonic velocities. The specific objectives were to look for second mode instability waves characteristic of the transition process and to quantify the percentage of turbulent flow. Two sets of data were used in this analysis. The first set of data was taken at several axial positions at a freestream Reynolds number 4.265 million per meter. This data was used to develop the analysis techniques. The second set of data was taken at station 35 for Reynolds numbers of 3.28, 3.94, 4.92, and 6.56 million per meter. Spectral analysis was used to identify 2nd mode disturbances, if they existed. The energy associated with the disturbances was then removed from the data signal to produce a new signal. The new signal was then evaluated using conditional sampling techniques. Additional methods used to assess turbulent intermittency were histogram analysis and examination of the power spectrum of the data signal. It was determined that removal of the disturbances from the raw data signal produced a cleaner signal. However, the new signals were not amenable to conditional sampling techniques. The histogram analysis proved to be inconclusive. Examination of the power spectrum showed that a laminar flow could be identified by the presence of a strong peak corresponding to the 2nd mode disturbances, but could not be used to identify a flow as being turbulent by the absence of this peak.				
14. SUBJECT TERMS Hypersonics, Boundary Layer, Transition			15. NUMBER OF PAGES 91	
			16. PRICE CODE	
17. SECURITY CLASSIFICATION OF REPORT UNCLASSIFIED	18. SECURITY CLASSIFICATION OF THIS PAGE UNCLASSIFIED	19. SECURITY CLASSIFICATION OF ABSTRACT UNCLASSIFIED	20. LIMITATION OF ABSTRACT UL	

Vita

Captain Richard A. Dennery was born on 22 April 1968 in Washington, D.C. He graduated from Lake Braddock High School in Burke, Virginia in 1986 and attended the U.S. Air Force Academy, graduating with a Bachelor of Science in Aeronautical Engineering in May 1990. Upon graduation, he received a regular commission in the USAF and served his first tour of duty at Tinker AFB, Oklahoma. He began as an aeronautical engineer assigned to the B-1B SPM where his duties included aircraft modifications and upgrades until entering the School of Engineering, Air Force Institute of Technology, in May 1993.